Title
Accessing and interpreting hydration dynamics on biological surfaces

Author
Barnes, Ryan

Publication Date
2017

University of California
Santa Barbara

Accessing and interpreting hydration dynamics on biological surfaces

A dissertation submitted in partial satisfaction
of the requirements for the degree

Doctor of Philosophy
in
Chemistry

by

Ryan P. Barnes

Committee in charge:

Professor Songi Han, Chair
Professor Frederick W. Dahlquist
Professor Steven K. Burrato
Professor Mark S. Sherwin

March 2018

The Dissertation of Ryan P. Barnes is approved.

Professor Frederick W. Dahlquist

Professor Steven K. Burrato

Professor Mark S. Sherwin

Professor Songi Han, Committee Chair

December 2017

Accessing and interpreting hydration dynamics on biological surfaces

by

Ryan P. Barnes

For my family.

Acknowledgements

Graduate school was challenging to say the least and I thought about quitting more than a few times but it was because of the support I recieved from my friends, family, and colleagues that I stuck it out and am here today. I'd like to take the time to thank all of those that have helped me along my way to getting here.

I'd like to start off by thanking all of my sports coaches that I had in elementary, middle, and highschool that taught me the value of hard work and determination. You see I wasn't always a good student, I'm still not sure if I am, but I was fortuante enough to excell at football and this is where I learned how to apply myself and really what it takes to put all of yourself into something. I'd like to thank two coaches specifically, Vim Koesian and Steve Wallace. Vim was my middle school football coach who pushed me to bust my butt and showed me that I can really be athletic eventhough I was the fat kid back then. Steve was my offensive line coach and algebra teacher in high school and he taught me the value of mentally applying myself on and off the field. Unfortunately I didn't take that lesson into the classroom until college.

Next I'd like to thank my undergraduate advisor Dave Ball who turned this art student into a chemistry student, an organic chemistry student at that. Dave is a grouchy old man but such a caring teacher. He took the time to let me think my way through concepts in class and later let me do research in his lab. It was in his class and later in doing research that I learned how rewarding it is to do research. He really taught me to believe in myself and made me time and again prove to myself that I am a capable researcher. Thank you Dave for all you have done for me over the years.

In graduate school I have been fortunate enough to work for Songi Han, who was the person to convince me to come to UCSB. Songi's enthusiasm and determination have been instrumental to my growth as a scientist. There have been times when I wasn't the best graduate student and Songi stuck with me and helped push me through it. If it wasn't for her I wouldn't be here today. Throughout my time at UCSB, Songi's group has been such a collaborative and supportive environment and I am so thankful to have worked with Songi and everyone in her group.

I wouldn't be the researcher I am today without John Franck, my first mentor and colleague, who pushed me to achieve what I thought was impossible and really showed me how science actually gets done. I remember the feeling of dread when John moved on to his postdoc at Cornell and eventual professorship at Syracuse because now I had to figure out how to do science on my own. John was such a fantastic scientist that I always felt like he'd be there to solve the problems that I couldn't. When he moved on I knew I had to do it myself and I learned that I could because I did solve the problems myself that I thought I couldn't. I can't thank John enough for everything he has done for me.

I was fortunate enough to spend the last couple of years working and share an office with Ilia Kaminker who I've become good friends with. Ilia and I were able to work together on several projects and also spend many a day in lab cursing at the same instrument. Ilia has been a great mentor and friend over the years and I'm definitely going to miss working with him.

That brings me to the amazing chef of the Han group, Neil Eschmann, who always seemed to be frying a turkey. Sunyia amd then Alicia who always remembered everyone's birthday and would bring in a cake. Tim, who would always manage to keep me grounded. Alisa, who would always help me operate the high field EPR.

Now I wouldn't be the same person without all of the amazing friends I've time with over the years. I'd like to thank everyone I've known in Santa Barbara, grad school would have been a lot harder of an experience without them. I'd like to thank Jimmy, Nelson, and Garrett for introducing me to all the great mountain biking and later Phillipe, Seth, Dave, Shane, and Doug for taking me on some great adventures. I need to thank my fellow cohorts in grad school who bore this experience with me and supported eachother through this Zach, Sean, Tracy, Bi, Jose, Jimmy, Katherine, Katie, Reike, Annie, and Damien.

Finally, I would like to thank my family. Thank you, Mom, fo your unconditional support. You have given me so much throughout my life, I will always be proud to be your son. Dad, thank you for your love and guidance. you taught me so much, even when I didn't want to learn. My brother Tim, you have always been a source of inspiration and now a person to look up to.

Curriculum Vitæ

Ryan P. Barnes

Education

2017	Ph.D. in Chemistry (Expected), University of California, Santa Barbara.
2012	B.S. in Chemistry, California State University, Chico.

Publications

1 **R. P. Barnes**, S. Han, "Site-specific hydration dynamics and protein dynamic transition measurements on the Trp-Cage protein," *In preparation* (2017).

2 **R. P. Barnes**, S. Sun, F. Dahlquist, M.Heyden, and S. Han, "Spatially heterogeneous surface water diffusivity around structured protein surfaces at equilibrium," *Journal of The American Chemical Society* **Accepted** (2017).

3 I. Kaminker, **R. P. Barnes**, and S. Han, "Arbitrary waveform modulated pulse EPR at 200 GHz," *Journal of Magnetic Resonance* **279** 81-90 (2017).

4 O. Fisette, C. Päslack, **R. P. Barnes**, M. Isas, R. Langen, M. Heyden, S. Han, and L. Schäffer, "Hydration dynamics of a periferal membrane protein," *Journal of the American Chemical Society* **138** 11526-11535 (2016).

5 **R. P. Barnes***, J. M. Franck*, T. J. Keller, T. Kaufmann, and S. Han, "Active cancellation - a means to zero dead-time pulse EPR," *Journal of Magnetic Resonance* **261** 199-204 (2015).

6 I. Kaminker, **R. P. Barnes**, and S. Han - "Overhauser dynamic nuclear polarization studies on local water dynamics", in *Methods in Enzymology* (P. Z. Qin and K. Warnake, ed.) **564** of "Electron paramagnetic resonance investigations of biological systems using spin labels, spin probes, and intrinsic metal ions, part B" 457-483 (2015).

7 T. Kaufmann*, T. J. Keller*, J. M. Franck*, R. P. Barnes, S. J. Glaser, J. M. Martinis, and S. Han, "DAC-board based X-band spectrometer with arbitrary waveform control," *Journal of Magnetic Resonance* **235** 95-108 (2013).

Abstract

Accessing and interpreting hydration dynamics on biological surfaces

by

Ryan P. Barnes

Hydration water is necessary for protein function. It was long thought that the hydration water was simply an innocent solvent. However, current findings show that water is not an innocent solvent but an active player. It is now thought that hydration water plays a crucial role in biomolecular recognition by mediating the thermodynamic interaction between a protein and its ligand. The current challenge is to measure the hydration water and protein side chain thermodynamical properties.

In this thesis we present site-specific measurements of hydration water motion on an array of biomolecular surfaces. We rationalize the hydration water motion in terms of the biomolecular surface properties. We find that the hydration water surrounding globular proteins contains information about the chemical and geometrical topology of the protein surface. We then present instrumentation developments to the Overhauser dynamic nuclear polarization (ODNP) methodology that made such measurements possible.

We then introduce a new technique to measure the protein dynamic transition site-specifically and thus a new way to probe the coupling between a protein and the surrounding hydration water. We present measurements made on a small folded peptide system, the Trp Cage, and find that the hydration water motion and the protein dynamic transition temperature are homogeneous across the surface of the peptide.

Finally we discuss the development of a high field pulse EPR spectrometer that features arbitrary waveform generation capabilities. We showcase the applicability of this instrument and discuss the applicability of this instrument to the study of protein

structure and dynamics.

Contents

List of Figures

Chapter 1

Introduction

"Life is like riding a bicycle. To keep your balance you must keep moving."

Albert Einstein

Water is essential for life. So much so that our search for life throughout the universe is focused on looking for that simple chemical compound H_2O. Water is the universal solvent for life. Only water is much much more than an innocent solvent. In the context of protein science, water is thought of as the 23^{rd} amino acid [3]. Water has a structural role in proteins providing the necessary interactions to give proteins their full functionality. Water is much more that a structural contributor to proteins, water also gives the protein life. Water lubricates the rigid polymer that is a protein and turns the protein into a dynamic entity such that the protein can now perform its function [4, 5, 6]. This simple chemical compound has such an influence over the smallest building block of life. Yet we're only now beginning to understand how water interacts with the building blocks of life.

Water is a necessary component for proteins to function, yet the specific roles that water may play in protein function are just now being uncovered. This is in part because experimental approaches to access the interaction between a protein and its surrounding hydration water have only within the last 20 years become available. The main challenge with accessing this interaction is that the water protein interaction is a heterogeneous transient surface interaction.

Proteins are an amalgamation of individual amino acids strung together into a polymer that folds up in such a way that its structure produces some specific chemical function. Thus the surface of a protein is both chemically and geometrically a highly heterogeneous quantity. More so the interaction between any one amino acid on the surface of the protein and any one hydration water is a transient one because both the amino acid and the hydration water are fluctuating in accordance with all of the transient forces that act on them. To further complicate matters the forces that act on the water molecule arise from different interactions than the forces that act on any specific amino acid.

All is not lost however. The endless feats of human ingenuity do not stop here. Centuries of creativity along with scientific and engineering development have brought us to a point where not only can we see the challenges that are ahead of us but we can also overcome them. Since the turn of the century when scientists noticed that water isn't just the universal backdrop for all biological functions there has been an ever ongoing development of techniques and experiments to understand the role that water plays in life.

1.1 Properties of hydration water

As early as 1945 it was proposed that hydration water drives protein folding through the hydrophobic effect [7]. Frank's early work on hydration entropy lead to the development of the iceberg model that describes how water structures around hydrophobic molecules and can thermodynamically drive protein folding [8]. It was later suggested, building upon the hydrophobic effect, that the dynamic rearrangement of the water solvent, which has to be expelled from hydrophobic parts of the protein, makes an important contribution to the free energy of protein folding [9].

Water not only drives protein folding but actively takes part in the structure of the protein as shown with an early x-ray crystallography study [3]. Structural water molecules have been shown to stabilize the ligand binding interaction between the hen egg white lysozyme and its antibody D1.3 where four water molecules were found to link the antigen and antibody upon complex formation [10].

It was later shown that there is a critical amount of hydration water, $h = 0.2\left(\frac{g_{water}}{g_{protein}}\right)$, necessary for the physiological function of many proteins [6]. Note that this critical level of hydration water is significantly more water molecules than the few structural waters reported by x-ray crystallography. This shows that it is not just the structural waters that influence protein function but also a minimum hydration level. Hydration water was later shown to play a role in proton pumps and electron transfers in which the transfer rate constant of both protons and electrons was shown to be governed by large fluctuations in the hydration shell which lead to dielectric relaxation [11]

1.2 Coupling between hydration water and protein motions

Hydration water is necessary for protein function but how does the hydration water influence protein function? In short the hydration shell lubricates the protein and in effect gives the protein life. However, how does the motion of the water, or water itself cause the protein to fluctuate? It was shown that at low hydration levels, well below $h = 2$, the EF-hand calcium-binding parvalbumin protein is relatively stattic except for few peripheral lysyl residues [12]. The researchers found that as they increased the hydration level the interior of the protein began to fluctuate however not with the same intensity as the peripheral lysyl residues. This suggests two things 1) that the progressive induction of mobility at increasing hydration proceeds from the periphery towards the protein interior and 2) that hydrophilic residues couple more strongly to the hydration water motion.

The dynamic coupling between water molecules and the side chains of proteins has become a very exciting field. Pal and Zewail showed with femtosecond spectroscopy that there are two different dynamical processes that water undergo at the surface of the protein, a weak transient interaction between the water molecule and the specific site on the protein that results in bulk like behavior and a much stronger interaction, enough to define rigid water structure, leading to water molecules that are much slower than bulk [13]. Fenimore and Young showed with Mössbauer and neutron scattering experiments that the fluctuations in the hydration shell are coupled to the fast side chain motions of the protein [14]. More so Lukasz and Elsaesser show that the vibrational modes of the hydration water around DNA molecules is strongly coupled to the DNA and can actively dissipate excess energy absorbed by the DNA complex, this has the potential to prevent damage to the DNA complex from UV photo absorption [15].

Researchers have shown that the correlated hydration water motions extend up to 20 Åfrom the surface of the protein [16] substantiating claims that the hydration water plays a role in biomolecular recognition [17]. The dynamics of protein side chain motion have been shown to be governed by the dynamics of the hydration shell by femtosecond spectroscopy that shows the site-specific dynamics of the hdyrtaion water are always faster than the protein side-chain motions yet have the same energy barrier indicating that the hydration shell motions drive the protein side-chain motions [18].

The coupling between the protein and its surrounding hydration water is not a uniform interaction across protein systems [19]. Membrane proteins on the other hand seem to be insulated by the membrane itself as has been shown by neutron scattering experiments on the purple membrane protein showed that below $260K$ the hydration water and protein motions are decoupled. The researchers suggest that the lipid dynamics have a stronger impact on the protein motions than the hydration water [20].

Later it was shown with NMR experiments that there are different regimes of coupling between proteins and the hydration water. Hierarchical protein motions have also been observed by the NMR experiments on the protein dynamic transition, protein motion is decoupled from the solvent below $160K$ where the backbone of the protein is frozen, above $160K$ solvent rotational motions activate and allow side chain to access different rotameric states with a more pronounced effect on hydrophilic side chains. At $220K$ larger amplitude peptide backbone motions are observed which are accompanied by the unfreezing of hydration waters corresponding to the onset of translational motion. Finally large amplitude side chain motions dominate at $250K$ [21].

1.3 Connection to Protein Function

There have been many studies that connect the hydration water fluctuations to the protein function or misfunction. Anamolously fast water molecules adjacent to key residues is thought to facilitate the formation of aggreagates called amyloids which are involved in neurodegenerative dieseases such as Alzheimer's and Parkinson's disease [22]. The release of CO from the heme group of Myoglobin was shown to be coupled to the viscoelastic motion of the hydration shell by Mössbauer spectroscopy [17] showing that functions of the Myoglobin protein are in the very least coupled to solvent motions. The isomerization of a protein is also thought to be dependent on the coupling to hydration water, Li and co workers show with MD simulations that the observation of protein isomerization is only possible if the coupled water-protein motions are accounted for [23].

1.4 The protein surface's effect on hydration water

Hydration water has a role in protein folding and function. It has been argued that hydration water is actually driving protein function [18]. However, the hydration water does not have a uniform influence over the entire protein. Hydration water interacts with specific residues [20] causing a localized response on the protein surface. This suggests that the protein is directing the hydration water yet the influence that a protein exerts on the surrounding hydration layer remains an active topic of study.

It was observed by MD simulation that when the protein surface offers charged pinning sites the hydration water molecules are hindered and percolate through the surface. Water molecules are pinned by the charged sites yet when the electrostatics of the protein surface are turned off the hydration water motion increases dramatically [24]. Showing that the electrostatics of the protein surface have a dramatic effect on the hydration water. While this study was very insightful it was later criticized, albeit lightly, because turning off the electrostatic interactions of the protein surface causes too great of a perturbation to be considered still physically representative [25]. Researchers developed a model to describe the hydrogen bond re-orientation and showed on a physically representative MD simulation that the kinetics of hydrogen bond breaking and formation is largely dictated by the excluded volume of the protein surface [26].

Experimentalists have also attempted to understand the influence that the protein surface exerts on the hydration water. Using the individual amino acids Leucine and Glycine, researchers showed that the hydrophobic group on Leucine caused a dramatic slow down of the hydration water compared to the hydrophilic Glycine [27]. Later the same group investigated the Leucine and Glycine system with MD simulations to find that the hydration water slow down around Leucine was caused at the hydrophobic / hydrophilic interface [28]. In line with Chandler's [29] work, this shows that the iceberg model [8] applies to small molecules. Researchers later showed that the iceberg effect was not limited to small molecules but also applies to interfaces as well. Using sum frequency vibration spectroscopy researchers found enhanced ordering at the hydrophobic interface between water and hexane compared to a water and air interface [30]. While there is enhanced ordering at hydrophobic surfaces or interfaces there is a depletion of water density adjacent to the hydrophobic surface that is akin to a water vapor interface [31] relative to a hydrophilic surface. This density depletion is thought to drive hydrophobic assembly.

It is to this great body of work that I add my small contributions to science. I alongside phenomenal colleagues and collaborators show that the hydration water diffusivity on the surface of globular proteins is significantly modulated by the surface hydropathy in chapter 2. We go further to investigate how the small Trp-cage peptide interacts with hydration water by measuring the hydration water diffusivity, density, and the protein dynamic transition site-specifically in chapter 3.

I then discuss developments that we have made to further our access to site-specific hydration water and protein properties. In chapter 4 I along with my colleague Ilia Kaminker discuss the current state of ODNP methodology and current developments that are under way. In chapter 5 I along with my colleagues Tim Keller, John Franck, and Thomas Kauffman detail the development of a home-built pulsed EPR instrument arbitrary waveform generator (AWG) capabilities. Then in chapter 6 I along with my colleague John Franck discuss how we employed our pulsed AWG-EPR to achieve zero dead time which allows for the detection of EPR signal throughout the experiment. Finally in chapter 7 I along with Ilia Kaminker discuss the implementation of an AWG into the high field pulse EPR spectrometer, developed by Ilia Kaminker, Alicia Lund, Alisa Leavesley, and Tingann Siaw, and some of the ongoing developments that I and others are working on.

Chapter 2

Rationalization of Hydration Dynamics on the Surface of Globular Proteins

2.1 Abstract

Hydration water on the surface of a protein is thought to mediate the thermodynamics of protein-ligand interactions. For hydration water to play a role beyond modulating global protein solubility or stability, the thermodynamic properties of hydration water must reflect on the properties of the heterogeneous protein surface, and thus spatially vary over the protein surface. A potent read-out of local variations in thermodynamic properties of hydration water is its equilibrium dynamics spanning picosecond to nanosecond timescales. In this study, we employ Overhauser dynamic nuclear polarization (ODNP) to probe the equilibrium hydration water dynamics at select sites on the surface of Chemotaxis Y (CheY) in dilute solution. ODNP reports on site-specific hydration water dynamics within $5-10\mathring{A}$ of a label tethered to the biomolecular surface on two

separate timescales of motion, corresponding to diffusive water (DW) and protein-water coupled motions, referred to as bound water (BW). We find DW dynamics to be highly heterogeneous across the surface of CheY. We identify a significant correlation between DW dynamics and the local hydropathy of the CheY protein surface, empirically determined by molecular dynamics (MD) simulations, and find the more hydrophobic sites to be hydrated with slower diffusing water. Furthermore, we compare the hydration water dynamics on different polypeptides and liposome surfaces, and found the DW dynamics on globular proteins to be significantly more heterogeneous than on IDPs, peptides, and liposomes. The heterogeneity in the hydration water dynamics suggests that structured proteins have the capacity to encode information into the surrounding hydration shell.

2.2 Introduction

Water is thought to be directly involved in tuning the structure, stability, dynamics and function of biological macromolecules. One proposed avenue by which water participates in molecular recognition of proteins is by thermodynamically mediating the interactions between protein-protein or protein-ligand binding partners [5]. This suggests that the protein extends its range of interaction by encoding structural or dynamic information in the layer of water molecules that directly hydrate the protein surface [5, 16, 32, 33]. It follows that there must be spatial diversity in the water environments on the surface of a protein to enhance or impose the properties of a protein surface. However, experimental data on surface-, region- or site-specific water properties on protein surfaces in native solution state is an active area of research [34, 35, 36, 37, 38, 39, 40]. Consequently, the nature or even existence of the relationship between the molecular makeup of the protein surface and variation in hydration water environments by which the protein may encode functional properties continues to elude scientific understanding.

To gain an understanding of the role that chemical or geometrical topology of the protein surface plays in tuning the hydration water properties, it is necessary to probe hydration water properties with both spatial and temporal resolution.

The thermodynamics of solvation dictate the hydration water dynamics on a protein surface, thus measuring the dynamics of hydration water around the protein surface under equilibrium conditions serves as a proxy for probing the thermodynamics of solvation. Overhauser dynamic nuclear polarization (ODNP) offers an experimental approach to characterize hydration water dynamics with site-specificity under ambient solution state conditions over ns to ps timescales of motion. The timescale of motions for water on the protein surface varies over decades from bound water (BW) with lifetimes of few to $10`s$ of $ns$ - to highly diffusive water (DW) with lifetimes of $1-100`s$ of ps. The BW population on the surface has the potential to constitute an entropic reservoir, as it provides a mechanism to increase the total entropy through its release and expulsion from the binding surface of the protein, compensating for the negative entropy change resulting from protein-ligand binding. The retardation of DW may reflect on the enthalpic cost to disrupt, and ultimately dehydrate, the hydration layer at the interface, while the slower population of DW may also constitute an entropic reservoir, whose liberation to bulk water increases the net entropy. To capture the relevant properties of hydration water, it is necessary to probe the water dynamics over this range of timescales. There is experimental evidence to show that coupled water protein motions [38, 39] and water hydrogen bond reorientational motions [35, 36, 41] are spatially heterogeneous. Here, we report on site-specific ODNP measurements on the Chemotaxis Y (CheY) protein at room temperature in dilute solution state to probe the DW and BW motions.

ODNP selectively amplifies the ^1H NMR signal of the local hydration water in close proximity $(5-10\mathring{A})$ to the spin label by transferring the larger magnetic polarization from the unpaired electron spin of the label to the ^1H nuclear spin of the adjacent water molecules. The dipolar coupling between the electron spin of the nitroxide radical label attached to the biomolecular surface and the ^1H of the surrounding water molecules is modulated by the relative motion of the electron spin and the 1H nuclear spin. Transfer of polarization from the electron spins to ^1H spins occurs through electron-^1H dipolar coupling via cross relaxation and leads to the amplification of the ^1H signal through the Overhauser effect [42, 43] as described in chapter 4. ODNP measurements quantify the dipolar coupling factor (ξ) between the unpaired electron spin and the ^1H nuclear spin that is dependent on the dipolar correlation time (τ_c) of electron-^1H inter-spin motions. Thus, ξ and τ_c serve as a read-out of the waters ^1H motion, given that the relative motion of the spin label is negligible compared to that of water. As discussed previously [44], ξ and τ are sensitive to motions on both the picosecond and nanosecond timescales, which on the protein surface correspond to DW and BW respectively. Thus, it is necessary to expand the standard ODNP approach to separately analyze the picosecond and nanosecond timescales of motion to individually access the DW and BW on the protein surface. Following the method proposed by Franck et al. [44] and further described in chapter 4 we separate ξ into the cross-relaxation rate (k_σ) that is selectively proportional to the spectral density function for a $\sim 9.8GHz$ transition frequency (corresponding to the Larmor frequency of the electron spin) and the electron spin-induced self-relaxation rate (k_{Low}) of the ^1H spin that is selectively proportional to the spectral density function for a $\sim 14MHz$ transition frequency (corresponding to the Larmor frequency of the ^1H nuclear spin). This allows us to separately analyze the timescales of motions, as k_σ is only sensitive to the $10-100\text{'}s$ of picosecond timescale and k_{Low} only to the $10-100\text{'}s$ of nanosecond timescale of motions. The access to spatial and temporal resolution is critical from an experimental perspective, because it allows for a multiplexed study of water dynamics around many different sites, of the same protein, in the same solution system, and under otherwise identical experimental conditions.

CheY is a globular protein with $12kDa$ molecular weight (PDB ID 1JBE), structure shown in Fig. 2.1. The protein is natively cysteine free to which we introduced a single cysteine residue by site-directed mutagenesis [45] at the sites shown in Fig. 2.1, and covalently tether a stable nitroxide radical-based spin label *S-(1-oxyl-2,2,5,5-tetramethyl-2,5-dihydro-1H-pyrrol-3-yl)methyl methanesulfonothioate* (MTSL). We compared both the DW and BW dynamics at 10 different locations on the surface of the CheY protein to that of 10 different CheY-derived 5-residue peptides composed of the nearest and next-nearest neighbors of each site studied on the CheY protein surface. The 5-residue CheY-inspired peptides have a molecular weight of $700 \pm 50Da$, and are too short to form any stable secondary structure. Therefore, the difference in the geometrical topology between the different peptides should be negligible in comparison to differences in the surface hydropathy dictated by the peptides side chain chemistry. These peptide systems thus serve as a control surface to exclusively evaluate the effect of the average hydropathy on the variation in DW and BW dynamics. To further substantiate our experimental data, we determined the local protein surface hydropathy and excluded volumes for CheY by all-atom molecular dynamics (MD) simulation, and compared the results to the trends in both the DW and BW dynamics. Finally, we compared the surface water properties of the CheY protein and the derived peptides to that of a series of other biomolecular surfaces, focusing on identifying defining characteristics of DW and BW contributions on the surface of structured proteins in comparison to that of intrinsically disordered proteins (IDPs) and liposomes.

We found significant heterogeneity in DW retardation on the surface of globular proteins, compared to relatively uniform DW retardation on peptide, IDP, and liposome surfaces. Furthermore, we found significant correlation between the measured local DW retardation and the local hydropathy, as calculated from the partitioning of hydrophobic probe solutes on the adjacent CheY protein surface site according to MD simulations. In comparison, any hydropathy scale from the literature based on counting or rationalizing individual contributions of amino acid residues produced no correlation to the experimental DW retardation. Lastly, we found that BW is present on only globular protein surfaces, while no BW was detected on IDP, peptide, or liposome surfaces. These experimental findings suggest that proteins with a defined structure have the capacity to encode functional information into the hydration water surrounding the protein surface.

2.3 Experimental

We investigate the influence of surface sites of *E. Coli chemotaxis* response regulator protein (CheY), a $14kDa$ globular protein (PDB ID 1JBE) shown in Fig. 2.1, on the local surface water diffusivity derived from ODNP measurements. We covalently attach a stable nitroxide radical-based spin label - via a di-sulfide bond - to a single cysteine residue introduced to the CheY protein by site-directed mutagenesis [45]. Cysteine mutants of the CheY protein were prepared via a similar manner used in a previous study [46]. Specifically, the gene encoding wild-type *Escherichia coli* (*E. coli*) CheY (residues 1 - 129) was cloned into pET28a (Novagen) at the NcoI and XhoI sites in frame with the carboxy-terminal hexahistidine tag. Cysteine mutants were generated with the QuikChange site-directed mutagenesis and transformed into E. coli BL21(DE3) (Novagen). The expression was induced at $OD_{600} = 0.4$ by the addition of $1mM$ isopropyl *β-D-1-thiogalactopyranoside (IPTG)* in Lysogeny broth (LB) medium. The proteins were then purified by immobilized nickel affinity chromatography (GE Healthcare). The collected fractions were dialyzed into a buffer consisting of $50mM$ sodium phosphate and $150mM$ sodium chloride at pH 7.9 and concentrated to about $0.5mM$. A nitroxide radical-based spin label was attached to the CheY mutants as described in the following. CheY cysteine mutants were reduced with $5mM$ dithiothreitol (DTT) (Sigma-Aldrich)

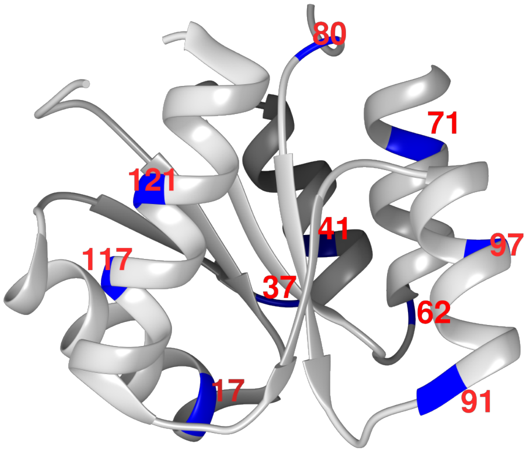

Figure 2.1: The X-ray crystal structure of CheY (PDB ID code 1JBE). The residues studied in this work are highlighted in blue and labeled in red. The protein structure was prepared in Chimera [1].

for $2hr$. Then, Sephadex G-25 spin column (GE-Healthcare) was used to remove DTT prior to the addition of MTSL at a $20:1$ reagent-to-protein molar ratio. The reaction mix was incubated at room temperature for $12hr$, and subsequently a Sephadex G-25 spin column used to remove the unreacted MTSL.

In this report we present and compare ODNP measurements on the surface of ΔTau-187 [47], α-synuclein [48], Annexin XII [49], and DOPC/DPPC LUV liposomes [50]. The hydration water retardation on the surface of ΔTau-187 monomers were measured on sites 313, 316, 322, 400, and 404 [47], of α-synuclein measured at sites 77, 81, 85, 86, 90, 93, 95, 98, 100, 101, 124, and 136 [48], and of Annexin XII measured at sites 12, 16, 104, 112, 121, 124, 137, 141, 162, 180, and 260 XII [49]. The liposomes systems were prepared in the LUV state and composed of purely DOPC, DPPC, and a $50:50$ mixture of DOPC / DPPC. The spin label was added to the lipid system by mixing in a phospholipid TEMPO-choline moiety [50] in a mol ratio of 2%.

The systematically charge varied peptide sequences are composed of CK, CD, CPPP, CPPPK, CPPPD, CPPPPPK, and CPPPPPD. The cysteine residue was labeled by addition of MTSL at a $1:3$ reagent-to-protein molar ratio. Purification by size exclusion or cation exchange chromatography was unsuccessful. A $1:3$ reagent-to-protein molar ratio limited free MTSL to $< 5\%$ of the total continuous wave EPR spectrum. The samples for ODNP were prepared in $20mM$ sodium acetate buffer.

2.3.1 ODNP Methods

Samples of approximately $3.5\mu L$ volume were placed in a $0.6mm$ i.d. and $0.84mm$ o.d. quartz capillary and analyzed by ODNP, as described previously [51]. A "pass through" NMR probe design built to fit inside a $3mm$ i.d. $6mm$ o.d. quartz tube was used. The quartz tube was inserted into a high sensitivity microwave cavity (ER 4119HS-LC, Bruker Biospin) along with the NMR probe and sample. ODNP experiments were performed using a Bruker EMX CW EPR spectrometer and a Bruker Avance III NMR console. The samples were sealed in a capillary with a protective layer of Critoseal on the top and hot beeswax on the bottom. All ODNP measurements were performed at room temperature. The sample was irradiated with up to $\sim 6W$ of microwaves at the EPR resonant frequency of the spin labels at $\sim 10GHz$ using a home-built microwave amplifier [52]. The magnetic field was set on resonance at the central electron hyperfine transition, here at $\sim 9.8GHz$. The spin label concentration of each sample was determined from the double integral of its cw EPR spectrum measured at $1mW$ irradiation power, $0.4G$ modulation width. The concentration-dependent ODNP relaxation rates, k_σ, k_ρ, and k_{Low}, are normalized to the sample concentration derived from spin counting per integration of the cw EPR spectrum.

In the following we present the correlation time τ_c of hydration water diffusivity, the cross relaxation rate k_σ, and the electron localized proton relaxation rate k_{Low} to report on different timescales of the proton diffusivity on the surface of the CheY protein. Our analysis of the ODNP data is explained in chapter 4. We first analyze the hydration water diffusivity by the retardation in correlation time $\tau_{c,site}/\tau_{c,bulk}$, which shows slower motion as a larger retardation factor. As discussed in section 4.6.2 the correlation time is sensitive to motions on both the nanosecond and picosecond timescale. We separately analyze motions on the picosecond timescale by reporting the retardation in the k_σ relaxation rate as $\left(\frac{k_{\sigma,site}}{k_{\sigma,bulk}}\right)^{-1}$ which only has dependence on picosecond timescale motions. The relationship between the retardation in k_σ and the retardation in correlation time of motion, given the FFHS model [53], is shown in Fig. 4.6B. Fig. 4.6B shows that as the retardation in correlation time increases the retardation in k_σ increases proportionally. Thus larger k_σ retardation corresponds to slower water motion. We analyze the nanosecond timescale motions by reporting the enhancement in k_{Low} as $\left(\frac{k_{Low,site}}{k_{Low,bulk}}\right)$. As discussed in section 4.6.2 enhancement in k_{Low} reports on the relative population of bound water at any specific site on the protein surface.

2.3.2 MD Simulations

Molecular dynamics simulations were performed starting from the crystal structure of the CheY protein (3CHY) [54]. Initial structures of the 5-residue peptides, corresponding to the sequence environment of the experimentally studied sites of CheY, were obtained from the same crystal structure by selecting the atoms of the respective amino acids and completing the N- and C-termini. All simulations were carried using the Gromacs 4.6.1 software package [55]. The proteins and peptides were modelled with the AMBER [56] force field and the SPC/E model [57] for water. All simulations were carried out in cubic simulation boxes with periodic boundary conditions. The particle-mesh Ewald [58] algorithm was employed to compute long-ranged electrostatic interactions on a real-space periodic grid with $1.2\mathring{A}$ resolution. Short-ranged pair-wise interactions were treated with a real-space cut-off at $9\mathring{A}$. A constant energy shift of the pairwise potentials was used to ensure zero interaction energies at the cut-off distance. Bond lengths in proteins and peptides were constrained with the LINCS [59] algorithm, while the SETTLE [60] algorithm was used to constrain the geometry of water molecules.

The protein was solvated with approximately 10500 water molecules, including 147 water molecules resolved in the crystal structure. The protein charge with standard protonation corresponding to a pH of 7 was neutralized with 4 sodium ions. The 5 residue peptides were solvated with approximately 2150 water molecules, and their total charge neutralized with either sodium or chloride ions.

All simulated systems were subjected to an initial energy minimization of 100 steps. This was followed by a 1nanosecond equilibration simulation with position restraints on protein/peptide non-hydrogen atoms under isothermal/isobaric conditions at $1bar$ and $300K$ and a subsequent 1 nanosecond equilibration without restraints. Both equilibrations were carried out with 1 femtosecond time steps combined with the Berendsen weak coupling algorithm [57] for the thermostat and barostat using a 1 picosecond time constant. The equilibrations were then followed by production simulations of 100 nanosecond length in the NPT ensemble. Production simulations used a timestep of 2 femtoseconds. The Nosé-Hoover thermostat [61] with a reference temperature of $300K$ and a period time of 1.0 picoseconds was used to describe temperature coupling to an external bath separately for the protein and the surrounding solvent. The Parrinello-Rahman barostat [62] with a 1picosecond period time and a reference pressure of $1bar$ was used for pressure coupling.

Local hydration water diffusion dynamics was analyzed in the vicinity of the experimentally studied sites via the mean squared displacements of water oxygens in the production simulations of the solvated CheY protein and the selected 5-residue peptides. For each experimentally studied amino acid in the protein or peptide, water molecules were selected at a given time in the trajectory within $5\mathring{A}$ of any sidechain atom of that residue. The translational motion of these water oxygens was then followed in time via the mean squared displacement (MSD).

$$MSD(t) = \langle |\vec{r}(t) - \vec{r}(0)| \rangle \tag{2.1}$$

MSD time traces were then averaged over the initial time points used to select the water oxygens for the MSD analysis. The average local hydration water MSD observed for delay times of 10 picoseconds, $MSD^{10ps} = MSD(t = 10ps)$, was then used to obtain a local measure of the translational diffusivity of hydration water molecules. The MSD obtained from explicit simulations inherently includes intrinsic effects on the translational mobility of hydration water molecules due to the inaccessible volume occupied by the protein, in addition to other interactions with the protein surface. The local retardation factor for water in the vicinity of a given protein/peptide sidechain was then determined by the local hydration water's MSD over the MSD of bulk water, $\left(MSD^{10ps}_{site}/MSD^{10ps}_{bulk}\right)^{-1}$, at $t = 10ps$. The bulk water reference value was obtained from a separate bulk water simulation under equivalent conditions. This system contained 11417 water molecules, which corresponds to a system size equivalent to the simulation box used for the solvated protein. We note that the simulations of proteins and peptides were carried out in absence of the spin label or cysteine mutation to obtain information on the unaltered environment of the specific sites. This is motivated by the observation that local hydration water retardation is only partially determined by the experimentally labeled site itself, and to a larger degree by its more extended chemical environment. This is suggested, for example, by a previous comparison between simulations of the unlabeled Anx protein with ODNP experiments that are comparable to the experiments reported here [49]. To test for the potential impact of local modifications, we carried out an additional set of simulations for the 5-residue peptides that included the cysteine mutation.

To characterize the local hydropathy of the protein surface of CheY, we carried out an additional simulation of the solvated CheY protein in which 75 hydrophobic Lennard-Jones (LJ) particles were added. The parameters of these particles were chosen according to a previous study of Acharya et al. [63] ($\sigma = 3.855\mathring{A}$ and $\epsilon = 0.694 kJ/mol$) that correspond roughly to a united atom representation of a methane molecule. The relative local concentration of LJ particles within $4\mathring{A}$ of any given protein atom, in comparison to the bulk solution, was used to determine the local excess chemical potential, μ_{LJ}^{ex}, which we interpret as a measure of the local hydropathy of the protein surface [63]. To compare the local and bulk solution concentrations of the LJ particles, we simply divide the average number of LJ particles by the average number of water molecules in the respective reference volume, i.e. within $4\mathring{A}$ of a given protein atom or within the total system.

$$\mu_{LJ}^{ex} = -k_B T ln \left(\frac{n_{LJ}^{local} / n_{h_2O}^{local}}{n_{LJ}^{total} / n_{H_2O}^{total}} \right) \tag{2.2}$$

In this definition, negative values for μ_{LH}^{ex} correspond to an increased concentration of LJ particles compared to the bulk solution and thus to a more hydrophobic character of the protein surface site. Positive values correspond to preferred hydration and a resulting expulsion of LJ particles compared to the bulk solution and therefore a more hydrophilic character of the protein surface site. With this definition, we follow previous work by Garde and co-workers [63] that utilizes the local excess chemical potential of LJ probe molecules as a reference for an approach to quantify the hydropathy of a protein surface. For a given amino acid, the average local hydropathies were computed as an average over atomic hydrophilicities obtained for the atoms of the amino acid itself, and atoms of nearby protein residues within varying distance cut-offs of R ranging from $0 \rightarrow 10\mathring{A}$.

This procedure then resulted in the cut-off distance dependent averaged local hydropathy $\mu_{LJ}^{ex}(R)$.

Local protein surface accessibilities were analyzed by counting the average number of water molecules within $4\mathring{A}$ of each protein atom, $n_{H_2O}^{local}$, and comparing it to the expectation value for a sphere of the same volume in bulk water, $n_{H_2O}^{bulk}$. The volume fraction excluded by the protein in the vicinity of that atom provides us with a measure of the site's accessibility, which is dictated by the protein geometrical topology:

$$f_{excl} = \frac{V_{protein}}{V_{sphere}} = 1 - \frac{n_{H_2O}^{local}}{n_{H_2O}^{bulk}} \tag{2.3}$$

Expected values for f_{excl} are ~ 0.5 in case of primarily flat surfaces, ~ 1 for completely buried atoms and < 0.5 for highly solvent-exposed atoms and/or at positive surface curvatures. For the experimentally studied sites of the CheY protein, we computed the average values for f_{excl} for the respective atoms of the given amino acid.

2.4 Results

2.4.1 Retardation of Surface Water Dynamics on CheY Proteins and Peptides

We investigated the hydration water retardation near the surface of a small globular protein, CheY, with site specificity. The hydration water retardation was sampled around 10 residues located on the CheY protein surface, specifically residues 17, 37, 41, 62, 71, 80, 91, 97, 117, and 121, see Fig. 2.1. To probe the local environment, the respective amino acid was mutated to a cysteine for spin labeling, making this a measurement of the local environment around the site, not of the respective residue. To evaluate the effect of the protein surface on hydration water dynamic properties around these 10 surface sites of

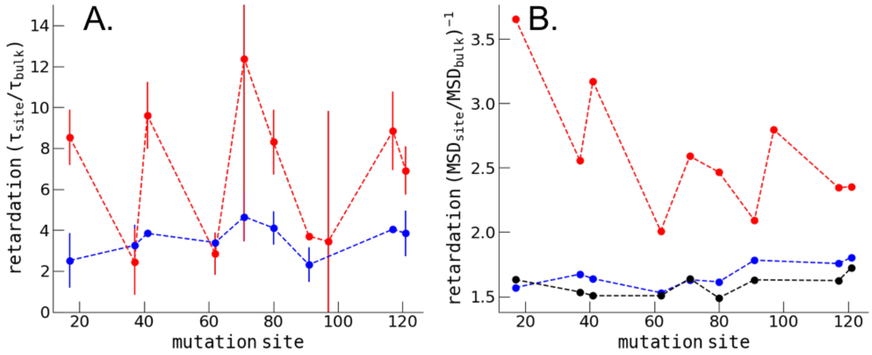

Figure 2.2: The hydration water retardation of the CheY protein (red) and 5-residue peptide segments (blue) as a function of the site of cysteine mutation. (A) shows the ODNP experimental results for the protein and peptide comparison, (B) show the MD simulation results for the protein and peptide comparison. MD derived retardation factors for 5-mer peptides including the cysteine mutation are shown in black.

CheY, we compared these to measurements of 5-residue peptides with the same primary sequence as the protein segment around the CheY site in question. In other words, the 5-residue peptides are composed of the nearest and next-nearest neighbor of each of the select 10 cysteine mutated sites of CheY, as listed in Table A.1. The experiment was designed to separately evaluate the effects of the complex surface environment of a globular folded protein vs the average hydrophilicity given by the amino acid composition on the local hydration water retardation around the protein surface site.

The ODNP-derived electron-^1H dipolar correlation time for hydration water, τ_c, modulated by the diffusive dynamics of water within $5-10\mathring{A}$ of the respective spin label is shown in Fig. 2.2 for the CheY protein (red) and the 5-residue peptides (blue). We observed that the surface water retardation (in-depth discussion to follow) as reflected in the τ_c value measured on the CheY surface relative to bulk water is significantly varied from site to site. The τ_c value measured on some sites increased up to $10-12$ fold relative to that of bulk water (henceforth referred to as retardation factor in correlation time of τ_c), while other sites reveal a modest retardation factor in τ_c of $2-3$ fold. In contrast, the retardation factor of τ_c for all peptide surface sites was modest, and ranged between $2-4$ fold. This trend is generally reproduced by the computationally derived retardation factor for local hydration water diffusion, as obtained from the slope of water oxygen MSD from our MD simulations (see section 2.3.2).

The corresponding results are shown in Fig. 2.2B, for the CheY protein in red, the 5-residue peptide in blue and for the 5-residue peptide including the CYS mutation in black. The simulated retardation factor of hydration water diffusion for the CheY protein varies between $2-3.5$, while it ranges narrowly around 1.5 for all peptides. Qualitatively the ODNP and MD simulation results agree, in that the hydration water of the protein surface displayed greater overall retardation, as well as a greater dispersion of retardation values from surface site to site of the protein compared to that of the peptides. However, the magnitude of the hydration water retardation factor reported by the ODNP-derived τ_c was significantly larger than found by MD simulations - an observation that will be further dissected.

The τ_c value measured by ODNP is modulated by two timescales of inter-spin motion between the hydration water and the spin label on the protein surface. We separately analyzed these timescales of inter-spin motion, and so access the dynamic properties of DW and BW. From the ODNP measurements we computed the cross-relaxation rate (k_σ) and the self-relaxation rate (k_{Low}), as described in detail in chapter 4 (see Eq 4.9 and 4.17). The cross-relaxation rate (k_σ) and self-relaxation rate (k_{Low}) are sensitive to $1-100's$ of picoseconds and $1-100's$ of nanoseconds timescale motions, respectively, that occur within the $5-10\AA$ sphere about the nitroxide spin label. The k_σ value increases monotonically with decreasing correlation time of water fluctuations, thus an increase in k_σ represents an increase in the rate for translational diffusion of hydration waters. Consequently, the retardation of DW is presented as the retardation of the k_σ relaxation rate, (see section 4.6.2). This correlation is valid as the k_σ retardation over the range of timescales present on the surface of the protein is approximately linear

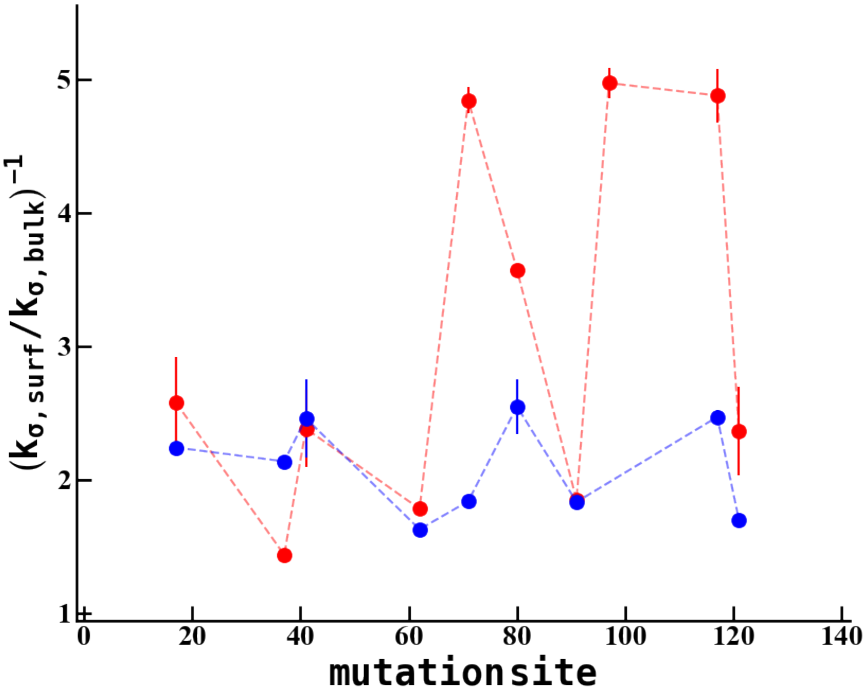

Figure 2.3: k_σ is shown normalized to the bulk water relaxation rate for each site measured on the CheY protein in red and for the 5-residue peptides in blue.

with τ_c retardation, as shown in Fig. 4.6B. While the k_σ relaxation rate is strongly modulated by the timescale of motion in the $1-100's$ of picoseconds range, the k_{Low} relaxation rate is both modulated by the timescale of biomolecule rotational motion on the $1-100's$ of nanosecond timescale and by the number of nearby BW molecules. As discussed in section 4.6.2, it is reasonable to assume that the rotational correlation time of each mutant protein is similar, so that any difference in the k_{Low} relaxation rate can be attributed to differences in the relative population of BW. Thus, on surface sites that harbor BW, we observe an enhancement in the kLow relaxation rate relative to bulk solvent, presented as $\left(\frac{k_{Low,site}}{k_{Low,bulk}}\right)$.

2.4.2 Analysis of Diffusive Surface Water

We now focus on the influence of the protein surface on the DW retardation. We present k_σ retardation, $\left(\frac{k_{\sigma,site}}{k_{\sigma,bulk}}\right)^{-1}$, found on the surface of the CheY protein and the 5-residue peptides in Fig. 2.3. We found on average a $3-fold$ retardation with a distribution ranging between $1.5-5$ on the CheY protein surface, while the peptide surfaces displayed a much narrower distribution of $2.3 \pm 0.5 - fold$. The relatively modest retardation of $\sim 3 - fold$ for DW dynamics reported here for the CheY protein is en par with experimental values in the literature of diffusing water on protein surfaces [16, 32, 35, 38, 39] as well as the calculated values by MD simulation in this study (Fig. 2.2B) and the literature [24, 25]. The observation that DW retardation on the peptide surfaces converges to a narrower range of values around ~ 2.3 suggests that a common property of all peptides is dictating the DW retardation. The excluded volume of each peptide is similar given their comparable molecular weights (see Table A.1), and as such is the likely common factor that determines the average DW retardation value. Looking to the small, yet distinct, variation in DW retardation, an intuitive cause for this is the variation in hydropathy between the peptides. The average hydropathy of each peptide, calculated by the GRand Average of hydropathY (GRAVY) score (see Table A.1), varies from -2 to 2. However, we find no correlation between the experimental DW retardation from k_σ relaxation and the GRAVY score, as shown in Fig. A.1. This indicates that the hydration water properties of even simple peptide systems are not well described by an average over individual amino acid residue properties. In order to describe the local hydration water properties even qualitatively, it is necessary to take the local chemical and geometrical topologies into account [64].

In contrast, the dispersion in DW retardation on the CheY protein surface is much greater than on the peptide surfaces, even though the average value of 3 is not much greater than the 2.3 found for the peptides. In other words, DW retardation is greater around some, but lower around other protein surface sites compared to that of the peptide counterparts. This variation may come from differences in local excluded volume between topologically different protein surface sites or variations in local surface hydrophilicity and chemical topology. To examine the molecular basis of the DW retardation, we compute the local surface hydrophilicity and excluded volume of the CheY protein surface by MD simulation.

However, before we launch into the interpretation of local water motion, it is important to address the possibility that the flexible spin label attached to the protein sidechain influences the hydration water dynamics reported by k_σ. We measured continuous wave electron paramagnetic resonance (cw-EPR) measurements on the spin label attached to the protein and performed line shape analysis to extract the correlation time of spin label motion, as shown and detailed in the appendix section A.1.5. We find that each site on the protein has in general two correlation times roughly corresponding to spin label rotation about the disulfide linkage (fast, $1 - 100's$ of picoseconds) and the protein backbone motion (slow, $1 - 10's$ of nanoseconds)[65, 66, 67]. There is no correlation between k_σ or k_{Low} and the fast timescale of spin label motion, showing that the independent spin label motion and the water dynamics, both in the picoseconds to sub-nanoseconds timescales reported by k_σ and k_{Low} are decoupled. We find a distinct correlation between k_σ and the slow timescale of spin label motion ($R^2 = 0.8$) which suggests that the local protein and hydration water motion is coupled. Such coupling is expected and there are studies in the literature experimentally demonstrating this relationship [37, 18, 68]. However, deriving local protein motion from cw-EPR data requires more in-depth studies at multiple frequencies, and thus we present this finding as a hypothesis.

2.4.3 MD Simulation: Local Hydropathy and Excluded Volume

The surface hydrophilicity was determined by analyzing the local concentration of small methane-sized LJ particles (added to the simulated system at a low concentration) in the vicinity of protein surface atoms (see Eq. 2.2 for details). Variations in the local concentration of the LJ particles describe changes in the excess chemical potential, μ_{LJ}^{ex}, which we use to quantify the local hydrophobicity. Averages are computed over atoms belonging to a respective amino acid, $\bar{\mu}_{LJ}^{ex}$, and also including additional atoms in the vicinity within a cutoff-radius $R, \bar{\mu}_{LJ}^{ex}(R)$, which includes influences of the extended environment. Negative values for μ_{LJ}^{ex}, $\bar{\mu}_{LJ}^{ex}$ or $\bar{\mu}_{LJ}^{ex}(R)$ correspond to hydrophobic sites with increased local concentrations of the LJ probe particles, while positive values are found for hydrophilic sites that are preferentially hydrated by water. The simulation results show that the local hydropathy of the protein surface is heterogeneous, with simulations using cosolvents instead of LJ particles [69], and varies roughly from (hydrophobic) to (hydrophilic), spanning the x-axis of Fig. 2.4A. We varied the cutoff distance for averaging over atomic hydropathies around a labelled site, and observe the strongest correlation with k_σ retardation of DW when we account for contributions within $5\mathring{A}$ of a given site. In this case, the coefficient of determination amounts to $R^2 = 0.77$ (see Fig. 2.4A). The R^2 coefficient of determination is severely reduced to 0.4 when considering only local contributions of the atoms of the individual amino acids (Fig. 2.4B). When accounting for increasingly non-local contributions of adjacent fractions of the protein surface beyond $5\mathring{A}$ distances, the correlation of the surface hydrophathy with the DW retardation plateaus at $R^2 = 0.6$ at $> 8\mathring{A}$. This finding indicates that properties of the protein surface, which determine chemical properties such as the effective hydropathy and the dynamic properties of hydration water, exert their main influence on a length scale of around $5\mathring{A}$, a distance that corresponds roughly to the diameter of two water molecules.

The correlation reveals that DW is least retarded in the vicinity of hydrophilic surfaces and most retarded on hydrophobic surfaces. This might seem counter-intuitive as hydrophilic surfaces are expected to form hydrogen bonds with water molecules that are associated with the slowdown in water dynamics [25]. On the other hand, water molecules can form clathrate-like structures around hydrophobic residues with a high surface curvature [29], which may also result in a slowdown. However, on low surface curvatures, i.e. flat hydrophobic surfaces, increasing numbers of defects in the water hydrogen bond network with increasing hydrophobicity should result in an decrease in water retardation [70, 71]. Neither of these mechanisms directly apply to a protein surface that displays heterogeneous topological and chemical features, making our finding a non-obvious result. We note that the average local hydropathy determined from our simulations is derived from the preferential partitioning of hydrophobic probe particles, and therefore does not simply rely on the presence of polar or non-polar groups. Instead, combined effects due to the geometrical and chemical topology of the protein surface are captured empirically, which is apparent from the absence of any correlation between the computed hydrophilicity values and the chemical nature of the central amino acid sidechain for a selected site.

The experimentally derived DW retardation and the computed local excluded volume around the CheY protein surface sites are plotted in Fig. 2.4C, where we find a weak to negligible correlation between k_σ and the surface excluded volume with $R^2 = 0.30$. In other words, variation in DW retardation shows no clear dependence on the local excluded volume determined by the protein surface geometrical topology, i.e. surface curvature and accessibility. This result does not imply that the excluded volume of the protein surface has no effect on DW retardation. It is possible that the excluded volumes present on the protein surface do not span a wide enough range to reveal an influence on the hydration water retardation, or to overcome the chemical variation present on the protein surface.

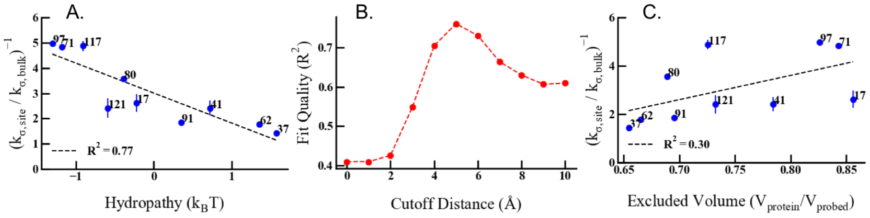

Figure 2.4: (a) shows the correlation between surface hydrophilicity shown on the x-axis with the DW represented by k_σ retardation on the y-axis. (b) shows the quality of the fit between DW retardation and surface hydrophilicity shown in (a) as R^2 as a function of the cutoff distance for averaging atomic hydropathies at the surface site. (c) shows the correlation between excluded volume on the protein surface and DW retardation.

If we for instance separate the sites by hydropathy into a hydrophobic group (hydropathy < 0, sites = 17, 71, 80, 97, 117, 121) and hydrophilic group (hydropathy > 0, sites = 37, 41, 62, 91) we see a correlation ($R^2 = 0.92$) between DW retardation of the hydrophilic sites and excluded volume, Fig. A.6. This suggests that the excluded volume has the expected influence on the DW retardation on hydrophilic sites, however that the DW dynamics of local water around hydrophobic sites are dominated by the hydrophobicity, perhaps by the hydrophobic mismatch as discussed in the literature [27, 28, 72], less by the excluded volume.

Importantly, k_σ does not probe the translational diffusion of one water molecule, but rather the average translational diffusion of several waters within a $5 - 10\mathring{A}$ sphere around the nitroxide oxygen. This sphere includes a number of water molecules that are within the first, second and even third hydration layer on the surface of the protein. This implies that the DW retardation probed by k_σ that is sensitive to the strength of the extended hydrogen bond network in the hydration layer, not merely a single water molecule most adjacent to and directly interacting with the protein surface site, is systematically increased with increasing hydrophobicity. Overall, our result is consistent with a clathrate-like behavior in which water molecules adjacent to hydrophobic surface sites form stronger hydrogen bonds to the neighboring water molecules of the hydration layer than the hydration waters adjacent to hydrophilic surface sites. This effect has been studied by Raman spectroscopy and MD simulation on small hydrophobic solutes that find increased water ordering around hydrophobic solutes compared to hydrophilic solutes [29, 73]. However, it was unknown to date what to expect from hydrophobic sites on net hydrophilic protein surfaces in dilute solution state in thermodynamic equilibrium.

2.4.4 Survey of Diffusive Surface Water on Other Biological Systems

Next, we examined other biomolecular surfaces with the goal of exploring the possible role that DW plays in specific binding. We analyzed the DW on a range of surfaces that can be separated into two categories: ones that take part in highly specific binding, such as folded globular proteins, and ones that tend to take part in less specific binding, such as intrinsically disordered proteins (IDPs), small peptides, and liposomes. Here, we analyzed the DW retardation on the folded globular protein surfaces of Annexin XII (Anx) [49] and CheY, the intrinsically disordered proteins of α-Synuclein (α-Syn) [48] and ΔTau187 [47], CheY-inspired 5-residue peptides, poly proline peptides with systematically varied charges (discussed in section A.1.1), and model LUV liposome surfaces made of DPPC and DOPC [50]. The description for each system is found in Methods. While ΔTau-187 and α-synuclein also participate in specific binding, the binding region extends over a significant portion of the IDP and/or these systems adopt a defined structure either just before binding or after binding to its target has occurred. Thus ΔTau-187 and α-synuclein in the disordered solution state does not represent the structure that participates in site-specific binding.

The surface DW dynamics for each system was evaluated by the DW retardation as expressed in and shown in Fig. 2.5. Each data point along a vertical line from the axis represents a different location on the respective surface. The globular proteins CheY and Anx displayed the largest distribution in DW retardation factors ranging from $1-6$. The IDP α-Synuclein also had a relatively large distribution ranging from $1-4$. The other IDP ΔTau187 displayed a narrow range of DW retardation around 2.7 ± 0.3, which is similar to that of the CheY-derived 5-residue peptides that displayed values 2.1 ± 0.5 around and the poly proline-based peptides of around 2.1 ± 0.4. Even so, the average DW retardation was found to be rather similar for any of these protein and peptide-based surfaces with the average retardation factor, $\left(\frac{k_{\sigma,site}}{k_{\sigma,bulk}}\right)^{-1}$, falling between $2-3$.

To evaluate whether there is a dominant effect of charges on the DW retardation on surfaces, we test poly proline-based peptides with systematically added charged residues. The sequences studied were CK, CD, CPPP, CPPPK, CPPPD, CPPPPPK, and CPPPPPD, where the lysine (K - positively charged) or aspartate (D - negatively charged) residue was systematically moved further from the spin label attached to the cysteine residue by the addition of proline residues. The DW retardation for each peptide was compared to the GRAVY score for each peptide and the composition of each peptide, as shown in Fig. A.1. We do not observe any consistent trend between DW retardation and the GRAVY score or the net charge of each peptide. This implies that the variation in local charges on a disordered peptide surface does not exert any persistent modulation in the DW retardation. The effects of charges on structured protein surfaces may be highly different.

Compared to IDP and peptide surfaces the LUV liposome surfaces showed significantly greater average DW retardation factors with ~ 4.5 on DOPC, ~ 5 on DPPC, and ~ 7.5 on mixed DOPC/DPPC liposomes. While the three values are co-plotted under the common categorization as “liposomes”, the DW retardation for a given LUV composition is uniform as there are no site-specific variations on the synthetic LUV surface studied here. What is clear is that the DW retardation on the liposome surfaces is significantly larger than that of the peptide and protein surfaces, including that of the globular proteins. Slow water fluctuations in and around PC lipids has been shown previously [49, 74, 75, 76] and is explained by a strong interaction between the charges on the phosphocholine group and water.

As introduced earlier, the retardation of DW dynamics can be viewed as reflecting on the enthalpic cost for disrupting and displacing the hydration water that is collectively strengthened by the attractive interaction between the protein surface and the hydrogen bonds of the local water network. When using DW retardation as a proxy in this way, the broad distribution of DW retardation observed on Anx and CheY surfaces suggests that some sites have a high enthalpic cost (most retarded) and other sites have a low enthalpic cost (least retarded) for displacing the local hydration water. In contrast, ΔTau187, the CheY peptides and the liposomes display narrow distributions in DW retardation, implying that displacing hydration waters has an approximately equal enthalpic cost for any position on these biomolecular surfaces. It is interesting to note that α-Syn - characterized under conditions known to populate an IDP state - displays a rather broad distribution in DW retardation, which may indicate that this IDP tends to populate a more persistent residual or transient solution state secondary structure and is prone to participate in specific binding, as has been postulated [77].

Recall that we found DW retardation in k_σ to inversely correlate with the local hydrophilicity of the protein surface sites (Fig. 2.4A). This would suggest that the enthalpic cost for disrupting and displacing the collective hydration water layer is higher near the more hydrophobic protein sites. The other finding is that the enthalpic cost for disrupting and displacing the collective hydration water layer of, and thus the enthalpic cost for solutes to approach, the liposome surface is by far greater compared to the cost for solutes to approach and bind to protein or peptide surfaces. In other words,

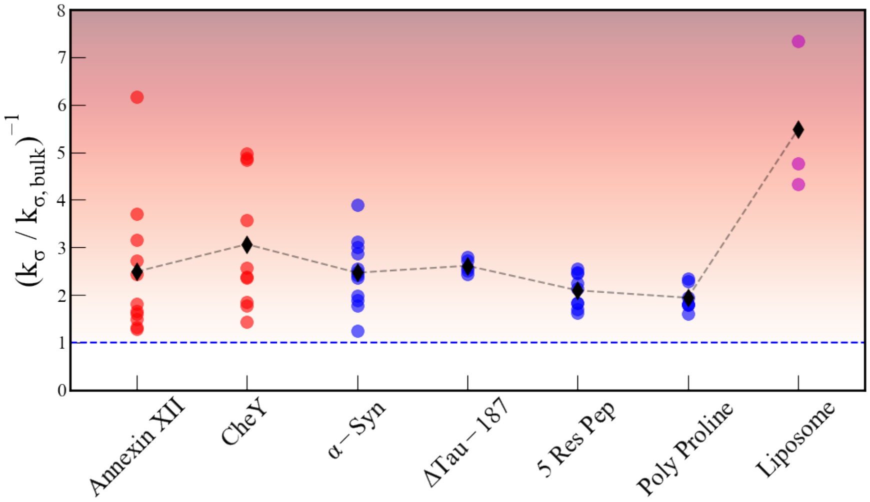

Figure 2.5: The k_σ retardation for each system studied. Each data point corresponding to a given system represents the value at a given site on the surface for the given system. The color shading represents fast or bulk like water as white and the maximally retarded water as black. The blue dashed line indicates the bulk value.

liposome surfaces display greater protection from solute interactions than protein or peptide surfaces.

2.4.5 Analysis of Bound Surface Water

Next, we focus on the influence of the protein surface on the BW population and dynamics, as measured by the k_{Low} relaxation rate. As introduced in chapter 4, the k_{Low} relaxation rate is enhanced by inter electron (spin label)-nuclear (water proton) spin fluctuations on the $1-100's$ of nanoseconds timescale. The total enhancement in the k_{Low} relaxation rate is a function of the number of water molecules fluctuating on the $1-100's$ of nanoseconds timescale and the correlation time of each fluctuation. As discussed in the Methods section, we limit our interpretation of the k_{Low} enhancement to a measure of the increase in bound water population, as expressed as an enhancement of k_{Low}, $\left(\frac{k_{Low,site}}{k_{Low,bulk}}\right)$. The variation in k_{Low} relaxation enhancement measured on the CheY protein surface (red) and the 5-residue CheY peptides (blue) is shown in Fig. 2.6. The

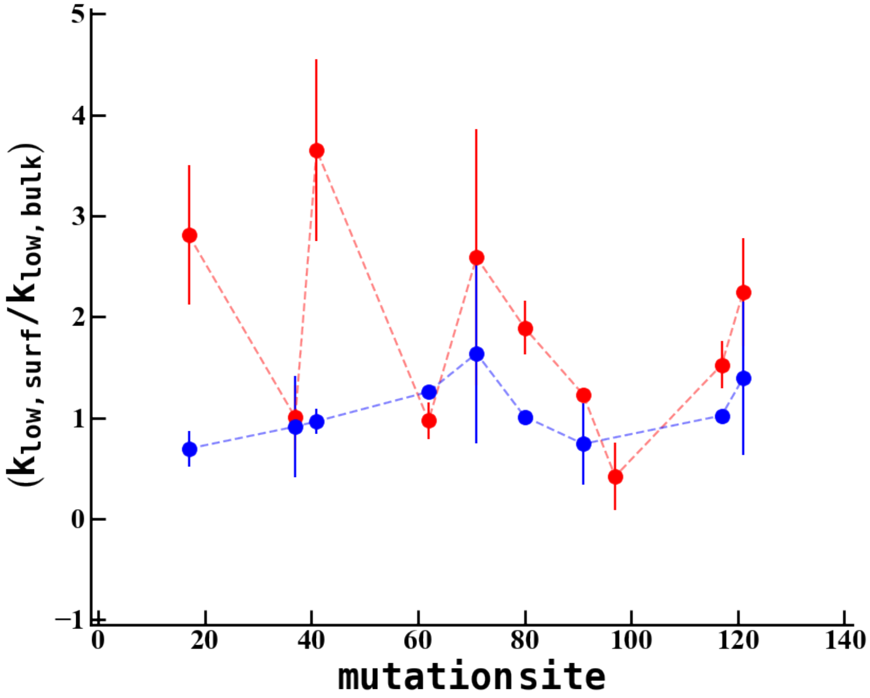

Figure 2.6: The kLow enhancement, the site specific k_{Low} relaxation rate normalize to the bulk water relaxation rate, is shown for each site measured on the CheY protein in red and for the 5-residue peptide segments in blue.

k_{Low} enhancement on the surface of CheY varies from $1-4$, where many sites have a k_{Low} enhancement above 2, indicating the presence of bound water at these sites. In contrast, the 5-residue peptides all have a negligible enhancement (1 ± 0.5) in the k_{Low} relaxation rate. The negligible k_{Low} enhancement may be due to the absence of BW population or the rapid tumbling time of the peptide system which prevents the detection of slow BW water.

2.4.6 Comparison to MD Simulation

Finally, we compare the presence of BW on the CheY protein surface to the estimated surface hydrophilicity and excluded volume, as calculated from MD simulation, in Fig. 2.7. The correlation between k_{Low} and the surface hydropathy is nonexistent, with an

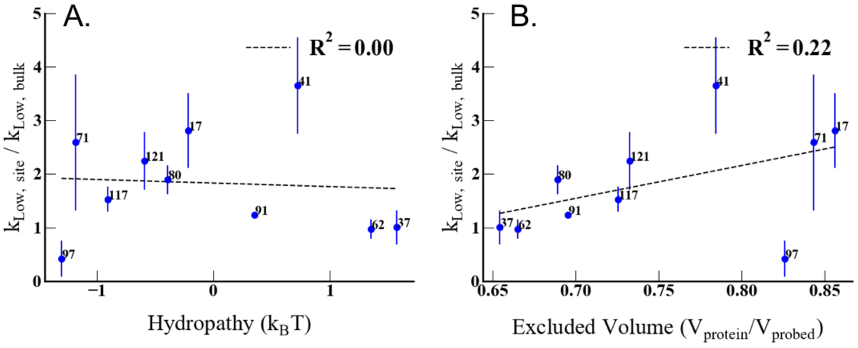

Figure 2.7: (a) shows the correlation between surface hydrophilicity shown on the x-axis with the BW represented by k_{Low} enhancement on the y-axis. (b) shows the correlation between the excluded volume of the surface sites and the BW represented as k_{Low} enhancement.

$R^2 = 0.00$ (Fig. 2.7A). There is a weak to negligible correlation between k_{Low} and the excluded volume of the protein surface, with an $R^2 = 0.22$ (Fig. 2.7B). The lack of any significant correlation between k_{Low} and the surface hydropathy or excluded volume does not necessarily imply that the BW population is not modulated by the properties of the protein surface. It is more likely that the BW population is determined by a combination of factors modulated by surface chemistry and geometry.

2.4.7 Survey of Bound Surface Water on Other Biological Systems

Finally, we find that BW is present on folded protein surfaces of CheY and Anx and absent on IDPs, including peptides, as well as on liposome surfaces. We find that there is no measurable correlation between the BW present on the protein surface to the hydrophilicity and excluded volume of the protein surface. Likely, the factors that govern the presence of BW must lie in the three-dimensional fold of the protein surface, while the molecular and structural determinants of the population of BW remain to be uncovered. It is important to note that we do not observe any correlation between DW retardation and BW populations, shown in Fig. A.2. This implies that not only are the two timescales of motion decoupled, but so is the origin for the variation in DW and BW contributions.

2.5 Conclusion

The contributions from and variation in DW and BW are thought to play a key role in protein ligand interactions through the modulation of the local thermodynamics of the interaction. Specific binding requires that some locations on the protein surface become thermodynamically more favorable for ligand binding than other locations on the surface. While the connection between the diffusive and bound water dynamics and the relevant enthalpic cost and entropic gain associated for expelling surface water is not clearly delineated and understood to date, our study finds that both DW and BW waters display significant spatial heterogeneity. This demonstrates that both bound and diffusive water dynamics are potentially effective modulators of specific and localized interactions involving the protein. This is further corroborated by our discovery that the most significant difference between structured proteins that engage in highly specific binding events and intrinsically disordered proteins that do not is the presence or absence of spatial variation in diffusive surface water dynamics and the presence or absence of bound surface water populations.

Chapter 3

Protein Dynamic Transition

3.1 Abstract

Hydration water on the surface of a protein plays a vital role in biomolecular interactions thus it is of upmost importance to understand the interaction between hydration water and the protein surface. Previously we found that large ($> 3kDa$) globular protein systems feature a very broad distribution in hydration water dynamics and that intrinsically disordered proteins and peptide systems have a relatively narrow distribution in hydration water dynamics. We want to know if this is because structural interconversion or lack of structural diversity. We investigate the hydration water dynamics and coupling to the Trp cage protein with Overhauser dynamic nuclear polarization (ODNP) and site-specific protein dynamic transition (PDT) measurements. The Trp cage protein contains 20 amino acids and exists in a folded solution state structure. This system features a persistent structure but also very little structural diversity and allows us to compare the effects of structural interconversion and little structural diversity. We selectively mutate residues on the Trp protein to a cys and attach a spin label to the cys residue to measure site-specific hydration water dynamics and the PDT temperature.

We find that the hydration water dynamics around the Trp protein are indistinguishable from IDPs and peptides. This shows that the diversity in hydration dynamics on the globular proteins is due to the long-range structure present on the surface and the lack of diversity on peptides and IDPs is due to the absence of structural diversity and not due to interconversion.

3.2 Introduction

Water is a major prerequisite for life as most if not all biological processes occur in water [78]. The water environment can be both a passive and active component in biological processes, as water can influence both the structure and function of the solvated biomolecules [5, 9]. The active water environment, the hydration water that directly solvates the biomolecule, can play a role in biomolecular recognition [79, 80, 5] as the information contained on the biomolecular surface gets projected on to the hydration layer. However, the relative contribution from different factors of the protein surface that influence the hydration layer properties remain under intense study.

Globular proteins have a very diverse hydration landscape [79, 38, 39, 26, 5, 18], that features a broad distribution of diffusive water (DW) and bound water (BW). Intrinsically disordered proteins (IDPs) and small peptide systems feature a comparatively homogeneous distribution of DW and a lack of BW altogether [79]. The origin of this difference is not clear. IDPs and peptide systems feature the same residue heterogeneity as the globular protein systems, but lack the defined structure present in globular protein systems. To determine what effect structural interconversion plays on the measured hydration dynamics we use the Trp cage protein as a model system. The Trp cage protein is a 20 amino acid globular protein that features an α-helix and a 3-10 helix and is stable in solution state conditions. The Trp protein has a minimal structure but does not undergo rapid interconversion like IDP and small peptide systems. Thus this system allows us to delineate the effects

The question is what effect does tertiary and longer range protein structure play in determining hydration water properties? Previously we have seen larger globular proteins that feature tertiary structure and long range order have a very diverse hydration landscape while intrinsically disordered proteins (IDPs) and small peptides (< 10 amino acids) that only feature primary and transient secondary structure have a relatively homogeneous hydration landscape. This would lead one to believe that long range structure has an important role in determining hydration water properties. However, the IDP and peptide systems rapidly interconvert between structures and this may average out any diversity present in the hydration layer. We wonder if each structure of an IDP or peptide has a very diverse hydration landscape and if this diverse hydration landscape gets averaged out over the ensemble of structures present.

In this study, we employ the Trp cage protein (PDB ID 1L2Y), a model system that has a defined and stable secondary structure to address the role of secondary and extensive tertiary structure on hydration water properties. We selectively mutate a cysteine residue into the Trp system and attach a nitroxide spin label to the cysteine to access this system. We measure the site-specific diffusive water (DW) hydration dynamics near the spin label on the Trp protein surface with ODNP and compare the results to analogous measurements on large globular proteins and peptides [79]. We then measure the site-specific dynamic transition temperature of the Trp system with pulse electron paramagnetic resonance (EPR) relaxation and compare the site-specific measurements to what is predicted from the community for globular proteins [81, 82, 80, 83]. Finally, we measure the site-specific hydration water density of the Trp system with electron spin echo envelope modulation (ESEEM) and compare that to what has been found in literature for globular proteins [51, 84, 85]. We find that the Trp protein with defined and stable secondary structure behaves more like a peptide than a globular protein and conclude that the hydration water properties around globular proteins are influenced by tertiary and long range structure.

3.3 Methods

3.3.1 Overhauser DNP

Overhauser DNP was performed at $0.35T$ using a Bruker EMX CW EPR spectrometer, a Bruker Avance NMR console, a Bruker Super HighQ dielectric microwave resonator, and a home built $10W$ and $9.8GHz$ microwave source described in [52]. The spin labeled Trp mutant was placed in phosphate buffer at $pH6.5$ to a concentration of approximately $200300\mu M$. Samples of approximately $3.5\mu M$ were placed in a $0.6mm$ I.D. and $0.84mm$ O.D. quartz capillary (Vitrocom CV6084). The samples were sealed with a protective layer of Critoseal on the top and hot beeswax on the bottom. A quartz tube connected to an airflow line was inserted into the microwave cavity and the NMR probe and sample were inserted into the quartz tube. All DNP measurements were performed at room temperature. The microwave resonator was tuned to $9.8GHz$, the rf tuning circuit was tuned to $14.8MHz$, and the magnetic field was set on resonance with the central electron spin transition. The proton free induction decay and proton T_1 relaxation time for each sample was measured as a function of microwave power up to $6W$. Each ODNP experiment was repeated at least twice. The concentration depended relaxation rate k_σ determined from ODNP was normalized to the concentration derived from the second integral of the CW EPR spectrum.

3.3.2 ESEEM

Electron spin echo envelope modulation (ESEEM) spectroscopy of deuterium was carried out at $0.35T$ and $9.2GHz$ on a Bruker Elexsys E580 spectrometer at $85K$. The spin labeled Trp protein in a deuterated water and 30 % protonated glycerol at approximately $100\mu M$ concentration was placed into a $1.85mm$ I.D. $2mm$ O.D quartz capillary. The sample in the capillary was submerged in liquid nitrogen for rapid freezing and then placed into the Bruker MS3 split ring resonator. The resonator was over-coupled at approximately $9.2GHz$ and the $\pi/2$ pulse length was calibrated. The field swept echo spectrum was recorded to find the maximum of the central transition. The static magnetic field was set to the maximum. The three-pulse ESEEM signal was recorded with the sequence $\pi/2 - \tau - \pi/2 - T - \pi/2 - \tau - echo$ and the standard phase cycle [86]. The constant delay was set to $\tau = 204ns$ corresponding to the proton blind spot. The second inter pulse delay, T, was incremented from $200ns$ to approximately $4\mu s$ in $24ns$ increments. For all ESEEM measurements the $\pi/2$ pulse length was set to $16ns$.

ESEEM was used to measure the local hydration water density on the surface of the protein. ESEEM was used to measure the deuterium modulation depth which is proportional to the number of water molecules nearby the spin label. The three-pulse ESEEM data was analyzed with a home-written python program that phased and background corrected the time domain data and computed the Fourier transform. The deuterium modulation depth k_D was obtained from the maximum of the deuterium peak in the ESEEM spectrum. The measurement-independent water accessibility parameter $\Pi(D_2O)$ was calculated through Eq. 3.1 [84].

$$\Pi(D_2O) = \frac{2k_D}{(1 - cos(2\pi\nu_D\tau)}\left(\frac{\nu_D}{2MHz}\right)^2 \tag{3.1}$$

Where ν_D is the deuterium larmor frequency and τ is the constant pulse spacing in the ESEEM experiment. In this manuscript we report the water accessibility relative to bulk solvent as a percentage, i.e. $(\Pi(D_2O)_{site}/\Pi(D_2O)_{bulk}) * 100\%$.

3.3.3 Protein dynamic transition

The Trp protein dynamic transition was measured by recording the electron T_2 relaxation as a function of temperature. The electron T_2 was measured on a Bruker Elexsys E580 spectrometer at $0.35T$ and $9.2GHz$. The spin labeled Trp protein was prepared in pure water and diluted with the cys-free wt-Trp protein at a dilution ration of $50:1$ of unlabeled protein to labeled protein. The sample was then freeze dried by lyophilization to a dry white and flakey powder. The hydrated powder samples were prepared by storing the loose dried protein powders in isopiestic chambers containing saturated $NaCl$ and K_2SO_4 solutions to produce a hydration level of $h = 0.2$ and $h = 0.4$ $(g_{water}/g_{protein})$ respectively. The dry powder samples were used as is post lyophilization. The powder samples were packed into a $0.8mm$ I.D. $1mm$ O.D. capillary. The sample temperature was carefully recorded during the experiment by an IR fiber optic temperature sensor that was placed in the sample capillary just above the sample position. The sample capillary and the fiber optic sensor were submerged in liquid nitrogen (for rapid freezing) and placed in the Bruker MS3 microwave cavity that sits inside of an Oxford Instruments cryostat cooled to $85K$. The microwave cavity was tuned and the $\pi/2$ pulse was calibrated. The field swept echo spectrum was recorded to find the central transition. The electron T_2 was measured by Hahn echo decay. The sample was continuously warmed up from $85K$ to $240K$ by setting the heater to maximum and turning off the control system on the temperature controller. The electron T_2 measurements were continuously repeated (lasting $\sim 5s$ each) during the entire course of the sample heating.

We investigate the dynamical transition of the protein powders by recording the local motion of the nuclei around the electron spin system through the PDT temperature. The electron spin relaxation is induced by two factors, the fast (< nanosecond timescale) reorientational motions of the nitroxide group containing the unpaired electron and the fluctuating electron nuclear spin interactions. We probe the PDT by focusing on the fluctuating electron nuclear spin interactions. The electron spin relaxation induced by reorientational motion is dependent on the spectral anisotropy at the position of the spectrum where the static magnetic field is applied. The electron nuclear hyperfine interaction, due to the ^{14}N of the nitroxide, splits the electron spin 1/2 into three transitions. The anisotropy of the central transition is only due to the g-tensor and not dependent on the hyperfine tensor whereas the other two lines, the low and high field lines, are dependent on both the g and the A-tensors [81, 82]. Thus, the central transition features the least anisotropy and is the least sensitive to reorientational motions of the nitroxide.

The anisotropy at the central transition of the electron spin spectrum is the less of the two factors that dominate the electron spin relaxation. The fluctuating electron nuclear interaction that arises from the motion of near by protons is the significant source of electron spin relaxation. We focus on this interaction as it provides a convenient "noise probe" for local fluctuating atoms. This measurement is nearly analogous to neutron scattering measurements.

Each Hahn echo decay curve was fit to a mono exponential to extract the T_2 as the time constant of the mono exponential fit. Each T_2 value was plotted against the corresponding temperature of the experiment. The PDT was realized as the inflection point in the $T_2(T)$ curve. The PDT temperature was estimated by fitting the inflection point to a third order polynomial and extracting the maximum value of the fit.

3.4 Results

We investigated the hydration water properties near the surface of the Trp cage protein with site specificity. The hydration water retardation, protein dynamic transition, and hydration water density was sampled around six residues located on the Trp protein surface, specifically residues 3, 5, 7, 10, 12, and 15, Fig. 3.1. We probed the local environment by mutating the respective amino acid to a cysteine residue for spin labeling. To evaluate the effect of the secondary structure, present in the Trp protein, we compare our measurements to those reported in literature for much larger protein systems that feature extensive tertiary structure as well as to peptide and intrinsically disordered systems that feature only primary and transient secondary structure.

3.4.1 Hydration water dynamics

We investigate the hydration water retardation by ODNP measurements and specifically focus on the cross-relaxation rate k_σ that is sensitive to pico second timescale motions. In the context of hydration water about a protein surface the pico second timescale is representative of translationally diffusive motions, we refer to this water as diffusive water (DW). We report retardation in DW motions as retardation in the k_σ relaxation rate, $(k_{\sigma,site}/k_{\sigma,bulk})^{-1}$. We measure k_σ by measuring the NMR signal enhancement of waters nearby the spin label via ODNP, described in chapter 4.

The DW retardation, shown by k_σ retardation, of the Trp protein is shown alongside the two globular proteins Anx and CheY Fig. 3.1. The DW retardation is shown site specifically for the Trp protein in the inset of Fig. 3.1. The DW retardation for the Trp protein from site to site varies from 1.4 to 1.8. In comparison, the DW retardation for Anx varies from 1.2 to 6.3 and CheY from 1.4 to 5. Notably the variation in the DW retardation is much greater for the proteins that feature extensive tertiary structure.

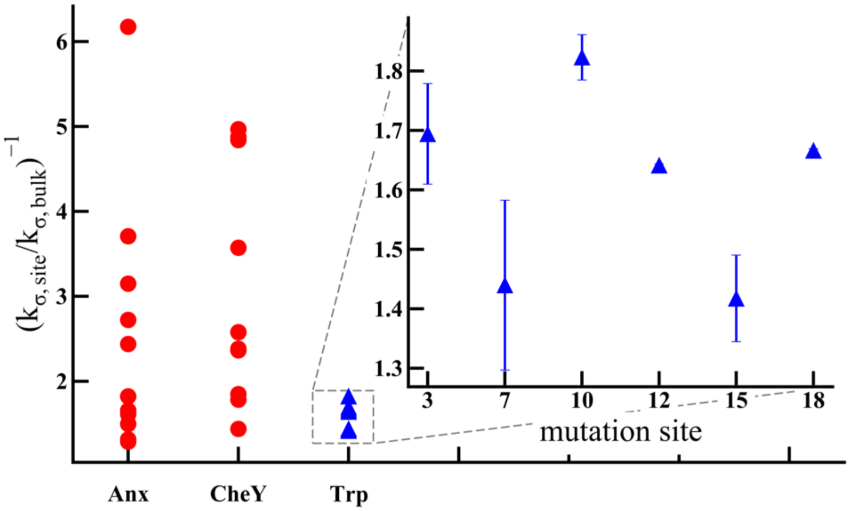

Figure 3.1: The site-specific measurements of solution state hydration water retardation, $\left(\frac{k_{\sigma,site}}{k_{\sigma,bulk}}\right)^{-1}$, shown for select sites on the globular proteins Annexin XII (Anx red) and Chemotaxis Y (CheY red) alongside each site of the Trp Cage protein (Trp blue). The inset shows the hydration water retardation as a function of the mutation site on the Trp Cage protein.

3.4.2 Protein dynamic transition

The protein dynamic transition is a means to probe the coupling between the protein surface and the hydration water. There are two transitions that hydrated protein powders undergo one at $100 - 150K$ that corresponds to motion of the methyl groups and one at $170 - 230K$ that corresponds to a transition from harmonic to anharmonic motions. It is this later transition, at $170 - 230K$, that we are interested in because it signifies the onset of large amplitude protein side chain and backbone motions, we refer to this transition as the protein dynamic transition (PDT). We want to probe the heterogeneity in the site-specific PDT temperature. It has been shown that large globular proteins feature a very large distribution in the PDT temperature, via MD simulation, estimated from neutron scattering, and very recently with pulse EPR.

We measure the PDT by making use of the spin label attached to the protein and

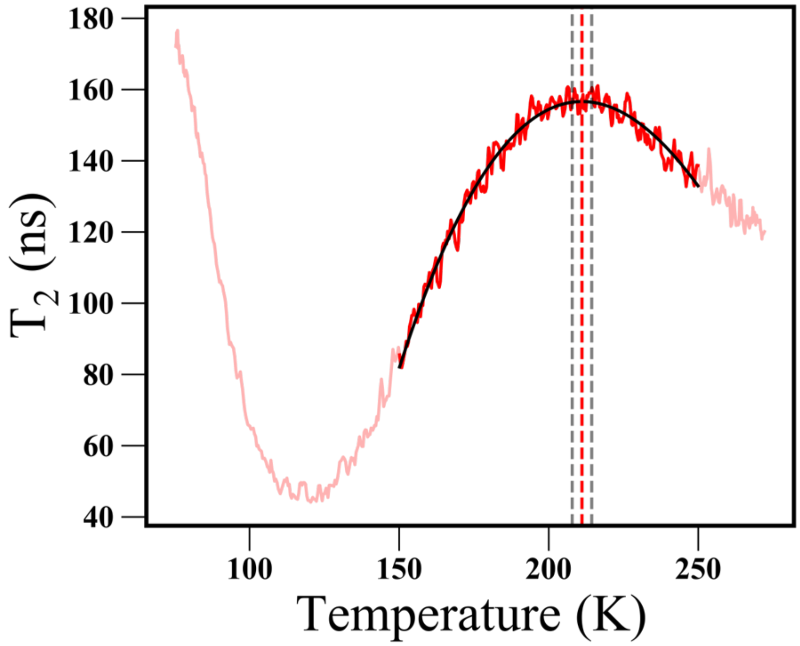

Figure 3.2: The opaque red line is the measured T_2 as a function of temperature. The solid red line is the portion of the data that is fit to a 3^{rd} order polynomial. The solid black line is the result of the polynomial fit. The red dashed line is the maxima of the polynomial fit and the black dashed lines are the error in the maxima of the polynomial fit.

employing a pulsed EPR method to read out the motion about the spin label, similar to Dzuba et. al. [82]. Here the spin label acts as a convenient probe for motion of all the magnetic nuclei around the electron spin, mainly protons, as well as the motion of the electron itself. We use the T_2 relaxation time of the electron spin as a relative measure of all the magnetic motion about the electron. To record the PDT we measure the electron T_2 as a function of temperature from $85K$ to $220K$, shown in Fig. 3.2. There are two notable features in the $T_2(T)$ curve, the minimum at $\sim 120K$ signifying methyl motions and the maximum at $\sim 190K$ signifying the PDT. We estimate the PDT temperature by fitting the $T_2(T)$ curve about the maximum to a polynomial and choose the maximum of the polynomial fit as the PDT temperature.

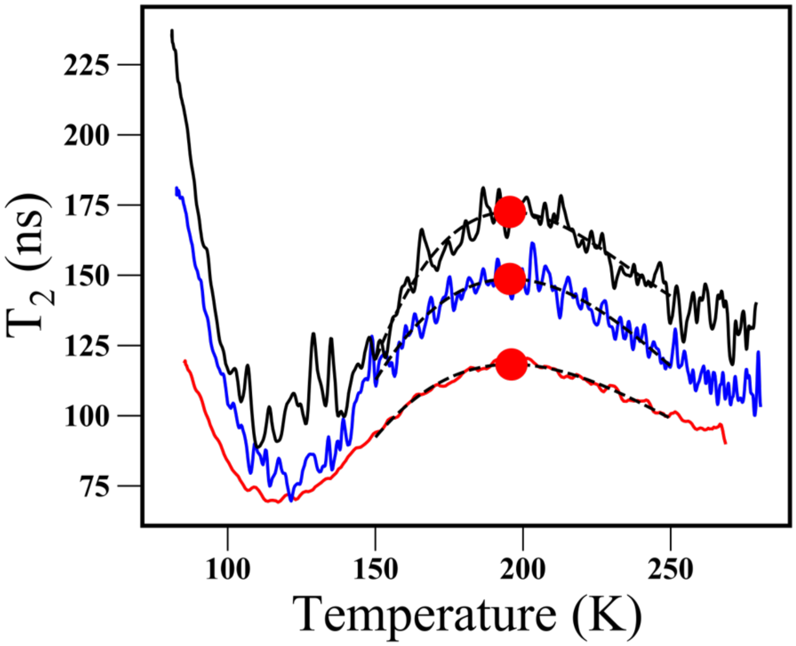

Figure 3.3: The dynamic transition as a function of spin dilution for the hydration level of $h = 0.2$. A spin label dilution of $20 : 1$ (unlabeled : labeled) is shown in red, $50 : 1$ is shown in blue, and $100 : 1$ is shown in black. The black dashed line shows the result of a cubic fit and the red dot shows the maxima of the cubic fit.

To ensure that the dipolar coupling between neighboring electron spins does not effect the measured PDT we measure the PDT as a function of spin label dilution. We prepare hydrated powders at a hydration level of $h = 0.2(g_{water}/g_{protein})$ and spin label dilutions of $20 : 1$, $50 : 1$, $100 : 1$ (unlabeled protein : labeled protein). We measure the electron $T_2(T)$ for each dilution ratio, shown in Fig. 3.3. We observe a difference in the absolute value of T_2 for each dilution ratio showing that the electron-electron dipolar coupling for the $20 : 1$ sample is the greatest and the lowest for the $100 : 1$ sample. While there are differences in the absolute T_2 there is no discernible difference in the estimated PDT temperature. Experimentally we find that the $50 : 1$ dilution ratio has the best signal to noise ratio, thus we use this dilution for all proceeding measurements.

We verified the PDT dependence on hydration level. We prepared three samples

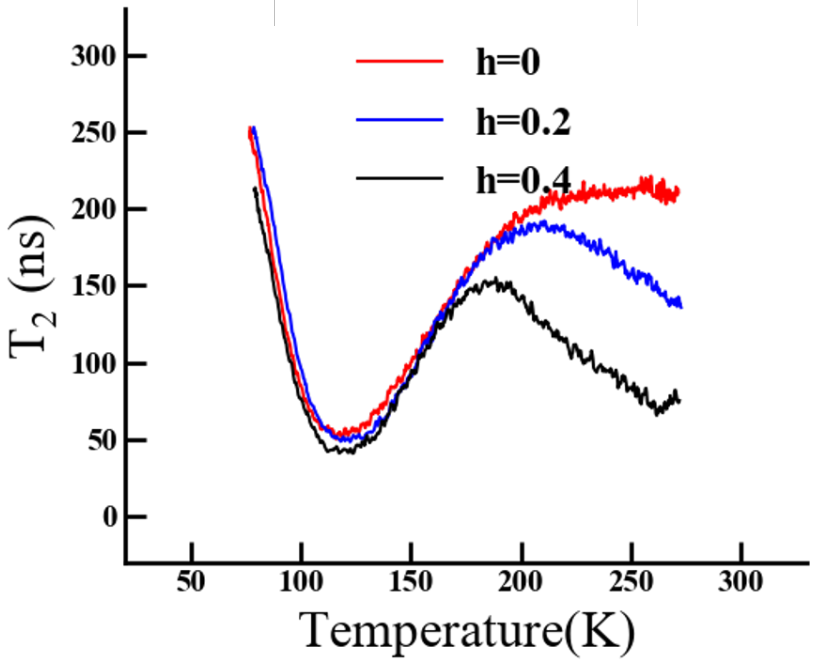

Figure 3.4: Measurements of the electron T_2 as a function of temperature for varying hydration levels. The dry powder is shown in red, the partially hydrated powder ($h \sim 0.2$) in blue, and the fully hydrated powder ($h \sim 0.4$) in black.

with hydration levels 0, 0.2, 0.4 ($g_{water}/g_{protein}$) and recorded the $T_2(T)$ curve. The PDT dependence on hydration level is shown in Fig. 3.4. We found that for a hydration level of 0 there is no observed PDT up to $220K$. We observed for a hydration level of 0.2 there is a PDT at $\sim 190K$ and for a hydration level of 0.4 the PDT shifts to lower temperature at $\sim 175K$. It has been shown that dry protein powders do not undergo a PDT up to $300K$ [87] while increasing the hydration level of the protein powder causes the PDT to shift to lower temperature [87, 80, 83].

It is worth pointing out that the PDT temperature recorded by $T_2(T)$ measurements is systematically lower than neutron scattering measurements. This discrepancy is due to the electron T_2 dependence on slower motions, specifically nano second and micro second timescale motions [82]. Thus, the electron T_2 is sensitive to the onset of slower motions

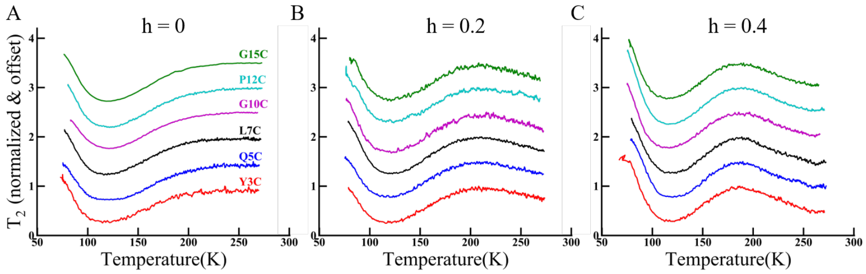

Figure 3.5: The electron T_2 measured as a function of temperature for the select sites on the Trp protein for varying levels of hydration. Measurements on the dehydrated powders are shown in (A), the partially hydrated powders ($h \sim 0.2$) in (B), and the fully hydrated powders ($h \sim 0.4$) in (C). The T_2 as a function of temperature is shown for the mutants Y3C (red), Q5C (blue), L7C (black), G10C (purple), P12C (cyan), and G15C (green).

than neutron scattering measurements and will show a deviation from harmonic motions at a lower temperature.

We investigated the site-specific coupling of the Trp protein to the surrounding hydration water by measuring the site-specific PDT temperature with EPR. We used protein powders composed of individual spin labeled mutants at a dilution ratio of $50 : 1$ and measured the $T_2(T)$ curve for each mutant at three hydration levels (0, 0.2, 0.4). Each trace for the $T_2(T)$ curve is shown in Fig. 3.5. We observed that for a given hydration level each site on the protein behaves indistinguishably. The estimated PDT temperature for each site is shown in Fig. 3.6. All the dry powders show no PDT, the partially hydrated powders ($h = 0.2$) have a dynamic transition at $\sim 190K$ and the fully hydrated powders ($h = 0.4$) have a dynamic transition at $\sim 175K$.

We observed that all sites studied on the Trp protein undergo a PDT at similar temperatures. This result has been observed in MD simulations previously. This shows that the individual sites on the Trp protein couple to the hydration water motion with the same strength. In comparison neutron scattering measurements on the much larger globular protein T4 Lysozyme it has been shown that the PDT temperature is not homo-

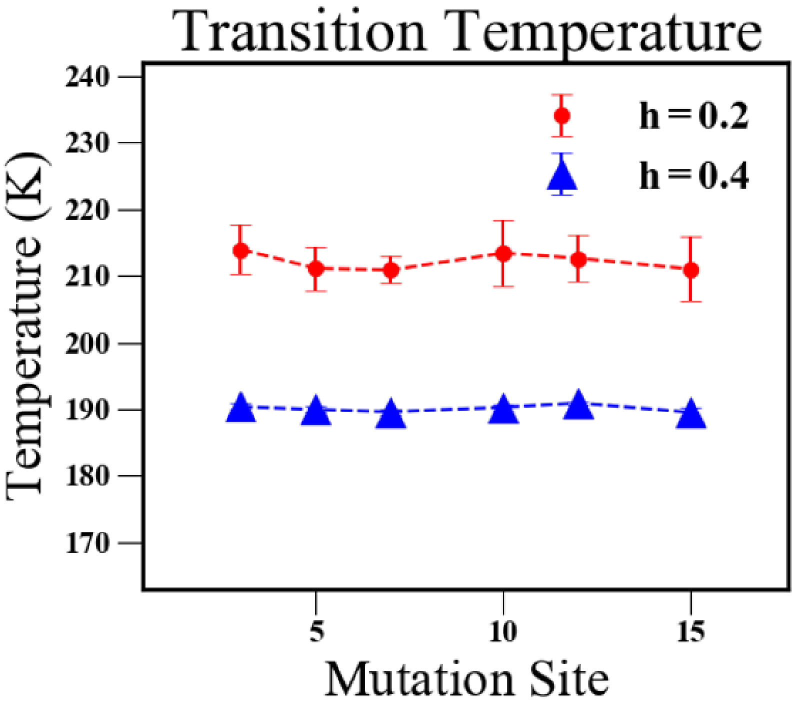

Figure 3.6: The dynamic transition temperature measured on the select sites of the protein for the partially hydrated powder (red) and the fully hydrated powder (blue).

geneous across the surface of the protein [83, 80]. MD simulations on T4 Lysozyme have shown that sites on the protein surface have very different PDT temperatures [87]. The disparity in PDT temperature from site to site is rationalized as being due to the complex surface environment on the protein surface and that the hydropathy and curvature of the surface effect the ability of water to couple to the protein surface and ultimately the PDT.

3.4.3 Hydration water density

We measured the hydration water density on the Trp protein using a pulsed EPR technique, electron spin echo envelope modulation (ESEEM). The ESEEM technique yields a water accessibility parameter $\Pi(D_2O)$, see methods section, that quantifies the

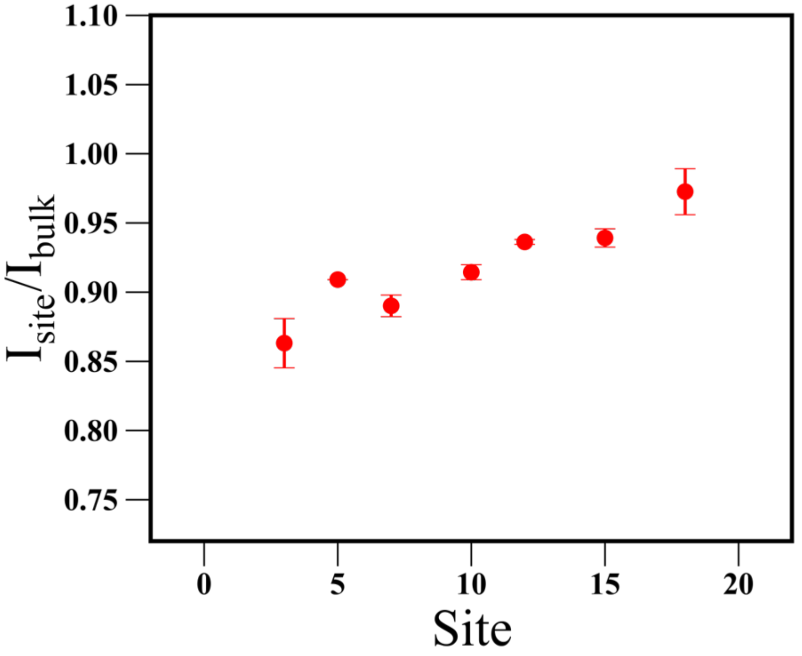

Figure 3.7: The relative hydration shown by the ratio of the ESEEM intensity at $2.16MHz$ measured on the protein surface to that measured in bulk solvent. Shown for each site on the Trp Cage protein.

relative amount of hydration waters are near any specific site on the protein and provides access to the protein surface topology. For convenience, we report the water accessibility as a percentage relative to bulk solvent.

The site-specific water accessibility parameter $\Pi(D_2O)$ measured on the Trp protein and normalized to the bulk water value is shown in Fig. 3.7. The water accessibility on the surface of the Trp protein varies from 85% to 95% of the bulk water value. For comparison, the water accessibility on the surface of the globular proteins varies much more widely from 20% to 85% reported by Volkov et. al. [84, 85]. The Trp protein is significantly hydrated all along the surface of the protein and these results match what is expected from an IDP or unstructured peptide.

3.5 Discussion

In a previous study [79] we found that globular proteins feature a diverse hydration environment with a wide range of hydration water retardation present on the surface. While we found that small unstructured peptide and IDP systems feature a comparatively homogeneous hydration environment, while we found reproducible variation from site to site on the peptide or IDP the variation was comparatively small. We wondered if this difference in hydration environments was due to the persistent structure that it present in globular proteins and lacking in the unstructured peptides and IDPs. Thus, we investigated the hydration water properties of the small but structured Trp Cage mini protein. The Trp cage mini protein features a persistent structure but lacks the structural diversity present in larger globular proteins.

We measured the local hydration water retardation variation from site to site with ODNP and found that the retardation in hydration water diffusivity on the Trp protein varies from 1.8 to 2.2. The variation in hydration water retardation previously found for the larger globular proteins CheY and Anx is 1.5 to 6.5. The average hydration water retardation is lower and the variation is smaller for the Trp cage mini protein than for either CheY or Anx. We measured the local PDT temperature for the Trp cage protein with EPR relaxometry and found that regardless of hydration level each site undergoes the dynamic transition at the same temperature. The PDT temperature for larger globular proteins is predicted to vary over the surface of the protein by up to $40K$ [87] and has been shown experimentally to vary by as much as $50K$ when comparing the dynamic transition temperature of the surface of the protein to the core of the protein [82, 81]. Finally, we measured the local hydration water density on the surface of the Trp cage mini protein with ESEEM and found that the hydration water density around the spin label on the surface of the protein varies from 85% to 96% relative to bulk water.

While for the globular protein Volkov the hydration water density about the spin label varies from 20% to 85% [84, 85].

3.6 Conclusion

In this study, we investigated the hydration water properties of the small folded Trp Cage protein system. We found that the variation in the hydration water retardation, the PDT temperature, and the hydration water density all resemble an intrinsically disordered protein or small unstructured peptide. This shows that persistent structure alone does not produce the rich diversity present in the hydration water of large globular proteins. It is the rich structural diversity due to the tertiary structure and long range order that is only found in the large globular proteins that produces the rich hydration environment present on such proteins.

Chapter 4

Overhauser Dynamic Nuclear Polarization Studies on Hydration Water Dynamics

4.1 Abstract

Overhauser dynamic nuclear polarization (ODNP) is an emerging technique for quantifying translational water dynamics in the vicinity ($< 1nm$) of stable radicals that can be chemically attached to macromolecules of interest. This has led to many in-depth and enlightening studies of hydration water of biomolecules, revolving around the role of solvent dynamics in the structure and function of proteins, nucleic acids, and lipid bilayer membranes. Still to date, a complete and fully automated ODNP instrument is not commercialized. The purpose of this chapter is to share the technical know-how of the hardware, theory, measurement, and data analysis method needed to successfully utilize and disseminate the ODNP technique.

4.2 Introduction

Overhauser dynamic nuclear polarization (ODNP) has attracted renewed interest in recent years with the rediscovery of its potential as a tool to quantify local water dynamics on biological or soft material surfaces. The method is based on measurement of water dynamics within distances of $5 - 10\mathring{A}$ around stable-radical-based spin probes that are either tethered to a site and surface of interest or selectively imbibed within a local volume of interest [88, 89, 2]. While the principle of ODNP has been around for over 50 years [90, 42, 91, 92, 93], new and exciting applications keep emerging [94, 95, 96, 97, 98]. The discovery of its usage at X-band ($8 - 12GHz$) microwave (mw) frequencies as a ^1H relaxometry tool to reveal translational diffusion dynamics of hydration water in a region- and site- specific manner has excited a large community of researchers. This method is being applied to address the question of the role of water and solvation in biological structure, function, dynamics, and beyond [89, 99, 100, 101, 102, 103, 51, 94, 104]. ^1H ODNP relaxometry is particularly powerful when it can naturally complement continuous-wave (CW) electron paramagnetic resonance (EPR) and other more advanced (pulsed) EPR measurements. A particularly rewarding combination is of ODNP with the pulse EPR technique of Electron Spin Echo Envelope Modulations (ESEEM) [105, 106] that can quantify the water density in the vicinity of the spin label of a frozen sample, and thus can powerfully complement the ODNP derived information on local water diffusion dynamics that, in a first approximation, is uncoupled from the water density in the local environment [51].

Importantly, ODNP shares the broad application range, scope, and high sensitivity of EPR. Because the size and complexity of the macromolecular system of interest is not fundamentally limiting and only $\sim 0.5nmol$ of sample is required ($3-5\mu l$ of $50-100\mu M$), ODNP and EPR methods are typically applicable for the study of large and complex biomolecular systems [107, 101, 108, 109]. The main requirement is that a stable spin label, typically nitroxide or trityl radical, can be incorporated reliably and site specifically. This allows ODNP and EPR analysis to access a large range of interesting biological and synthetic systems that are often beyond the reach of light scattering, crystallography, or highresolution NMR spectroscopy. Thus far, ODNP was successfully applied to studies of globular proteins [51], protein folding [34], intrinsically disordered proteins [110, 47], lipid membrane systems [103, 111, 112], membrane proteins [101, 99, 102, 108], peptides [113, 114, 115], polymer systems [99, 115, 111], and more recently, nucleic acids [44]. Nevertheless, these studies are barely scratching the surface of key questions that ODNP in combination with EPR methodology is capable of addressing, such as the functional role of solvent in protein binding, recognition or catalysis, or more fundamentally, the nature of proteinwater coupling under ambient solution conditions.

Fortunately, for the experimentalist, an ODNP spectrometer operating at $0.35T$ is in practice an add-on to an existing CW EPR spectrometer. An additional advantage is that a sample prepared for ODNP can also be used for CW EPR characterization and vice versa. As with most experimental techniques, the key for successful deployment of the technique and broad dissemination to a new user base relies on optimized and robust experimental and hardware designs. This chapter will describe the “how to” of ODNP experiments, focusing on techniques, analysis methods, and equipment employed in ODNP measurements.

The ODNP-derived water dynamics are most commonly analyzed with the unit-less electronnuclear coupling factor, ξ, which is directly obtained from the NMR signal enhancement and ${}^{1}H$ T_1 relaxation data [42]. However, in order to translate ξ into a physical parameters that scale with known units, several assumptions are made and models applied to convert ξ into a correlation time τ_c and a local diffusion coefficient D_{local} of water within $5 - 10\mathring{A}$ of the spin label (see Section 4.3). The relationship between ξ

and τ_c is shown in Fig. 4.1, which illustrates the dynamic range and the sensitivity of the ξ parameter to the translational diffusion correlation time between a few tens of picoseconds to sub-nanosecond the type of dynamics captured when ODNP is performed at $0.35T$. When compiling experimental ODNP data from the literature onto this $\xi(\tau_c)$ plot, distinct regimes for local water dynamics can be recognized. For example, ODNP provides a clear distinction between different regimes of water dynamics: (i) bulk-like water dynamics ($0.15 < \xi < 0.3$) found not only in bulk solution systems, but also on the surface of DNA duplexes [44] and the inner surface of the chaperon GroEL/ES cavity [51] that displays unusually unhindered translational diffusion dynamics for water; (ii) surface dynamics ($0.07 < \xi < 0.15$) - as found on most hydrophilic biomolecular surfaces, such as the surface of lipid bilayers, peptides, proteins, and polymers; and finally (iii) buried dynamics ($\xi < 0.07$) as found at sites within the core of a protein or lipid bilayer or strongly confined interfaces. The observation that the measured local water diffusivity across such a large range and classes of biological and soft material systems fall into distinctly identifiable regions implies that absolute characterization of solvent exposure or surface hydrophilicity/hydrophobicity is likely feasible, and also that events involving changes of surfacesolvent interaction, such as protein folding, aggregation, and binding, can be probed by ODNP.

However, ODNP can do more than passively probe and report on events of macromolecular interaction, folding, and aggregation. More excitingly, ODNP at $0.35T$ was found to be critically sensitive such that it has revealed a heterogeneous surface hydration dynamic topology on a globular protein [34], where the contrast in surface water diffusivity arises from different topology of the amino acid arrangement of entirely solvent-exposed sites, not simply from contrast due to differential solvent exposure or burial of different sites [101]. Thus, it has been proposed that this hydration dynamics landscape harbors information that has predictive values on the location of binding interfaces or

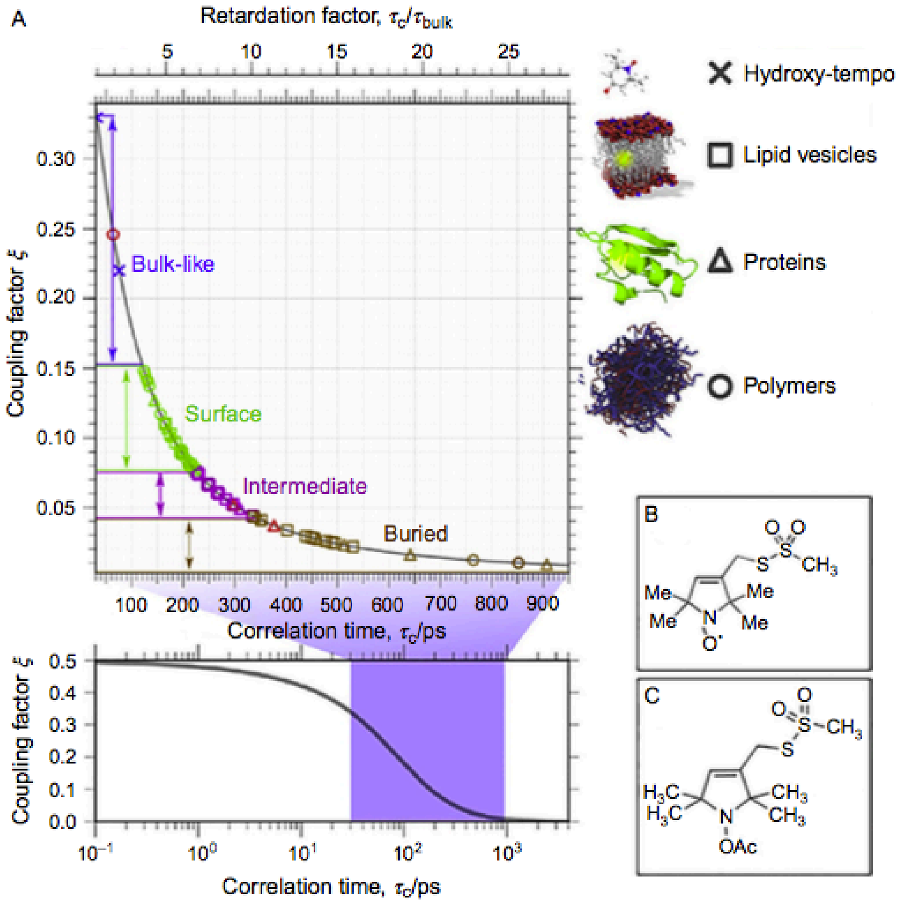

Figure 4.1: Data for the coupling factor ξ for a set of known biological spin probe (spin label) positions for a variety of systems appearing in the ODNP literature. The bottom panel shows the FFHS curve plotted over a larger range of logarithmically spaced correlation times. Adopted from figure 12 of Franck, et al. [2].

enzymatically active sites [116]information that cannot be obtained even from a fully resolved 3D protein structure a priori.

4.3 Theory

We briefly review the necessary theoretical basis for analyzing data obtained in an ODNP experiment for the purpose of extracting hydration dynamics. Particular attention will be given to the special case of using a nitroxide radical, as this is currently

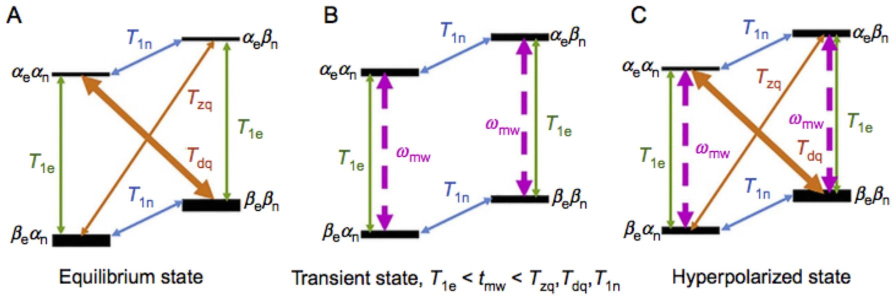

Figure 4.2: Energy level and populations diagram for the $S = 1/2$, $I = 1/2$ spin system. Thickness of the black bars represents the population of the corresponding level at each stage of the experiment. (A) At thermal equilibrium (no mw irradiation). (B) At transient state where irradiation time (t_{mw}) is short such that electron transitions are saturated but redistribution due to cross-relaxation is still negligible. (C) At steady state with mw irradiation on.

almost exclusively employed as the spin probe for ODNP-derived hydration dynamics studies. We do not intend to present a rigorous derivation of the ODNP theory, but rather to present a concise summary of the equations and relations needed for the basic understanding of the ODNP experiment and the associated data analysis. For more rigorous in-depth treatments, the reader is referred to the excellent reviews published throughout the years [101, 2, 117, 42].

Fig. 4.2 illustrates the change in the spin population of different levels in the course of a simplified ODNP experiment on an $s = 1/2$, $I = 1/2$ spin system. Fig. 4.2A illustrates the thermal equilibrium state. The $\beta_e\alpha_n$ and $\beta_e\beta_n$ states have higher population as defined by the Boltzmann distribution and depicted by the thicker black bars. All relaxation rates present in the system, namely electron spin lattice relaxation T_{1e}, nuclear spin lattice relaxation T_{1n}, and zero and double-quantum relaxation rates T_{zq} and T_{dq} are depicted on Fig. 4.2A as solid double headed arrows. Fig. 4.2B illustrates a transient state that is achieved quickly after mw irradiation on resonance with the EPR transitions (denoted as dashed arrows) is applied, so that $T_{1e} < t_{mw} < T_{zq}$, T_{dq}, and T_{1n} where t_{mw} denotes the duration of the mw irradiation. Here, we assume the mw irradiation is strong enough to achieve full saturation of the $\beta_e\beta_n \rightarrow \alpha_e\beta_n$ and $\beta_e\alpha_n \rightarrow \alpha_e\alpha_n$ electron transitions, namely equalizing the populations of the connected energy levels. Note that the NMR signal is given by

$$S_{NMR} = P(\alpha_e\beta_n) - P(\alpha_e\alpha_n) + P(\beta_e\beta_n) - P(\beta_e\alpha_n) \tag{4.1}$$

Thus, mw saturation in this regime does not alter the NMR signal from its equilibrium state (Fig. 4.2A). Fig. 4.2C shows the redistribution of populations in the steady state achieved after prolonged mw irradiation, so that $t_{mw} > T_{1n}$, T_{zq}, T_{dq}. The hyperpolarized state is a result of simultaneous action of the mw irradiation and unequal zero-quantum and double-quantum relaxation rates. Note that if $T_{dq} < T_{zq}$, the resulting hyperpolarized NMR signal given by Eq. (4.1) is going to be inverted relative to the equilibrium signal. So, ODNP enhancement results from the difference in zero- and double-quantum relaxation rates. The source of these cross-relaxation rates in liquids lies in the high-frequency modulation of the dipolar interaction between water proton and the unpaired electron spin of the nitroxide radical-based spin probe. The extent of the inequality between zero- and double-quantum rates, which is the source of the ODNP enhancement, is thus a direct measurement of the spectral density function, which characterizes the local motion of water in the vicinity of the unpaired electron spin. The details are given in Section 4.3.1.

4.3.1 Relaxation Rates

The most common way to analyze ODNP data is by interpreting the unitless parameter ξ commonly referred to as the coupling factor that, as shown below, reports on the local ($< 1nm$) dynamics of the water molecules around the spin label.

$$\xi = \frac{k_\sigma}{k_\rho} \tag{4.2}$$

Here k_σ and k_ρ denote, the cross-relaxation $k_\sigma = \frac{1}{T_{dq}} - \frac{1}{T_{zq}}$ and the radical-induced self-relaxation $k_\rho = \frac{2}{T_{1n}} + \frac{1}{T_{zq}} + frac1T_{dq}$ rates between the ^1H water nuclei and the electron spin on the biomolecular surface. All above relaxation processes are driven by the time-dependent electronnuclear dipolar interactions between the unpaired electron spin of the nitroxide and the water ^1H nuclei. The r^{-3} dependence of the dipolar interaction leads to rates governed by dipolar relaxation to scale as r^{-6}, where r denotes the electronnuclear distance [118]. The implication of the distance dependence of the dipolar interaction is that the coupling factor reports on water dynamics in close vicinity (i.e., within $< 1nm$) of the spin probe [88, 89, 119]. This localization effect is central to the high spatial sensitivity of the ODNP technique. It allows for the characterization of site-specific hydration dynamics by carefully positioning the spin labels on the biomacromolecules or by clever choice of tailored spin probes (by size, charge, hydrophobicity, etc.) with known partitioning properties.

To calculate the coupling factor, it is necessary to measure k_ρ, which includes the contribution to the relaxation rate of the nuclei due strictly to the presence of the unpaired electron. In practice, especially at low radical concentrations ($< 0.1mM$), other contributions to the water ^1H T_1 relaxation will typically dominate the experimental value of the T_1 relaxation as obtained in the inversion recovery experiment. To account for this, we measure the "background" relaxation rate $T_{1,0}$ of the sample of identical composition (i.e., same biomolecules, same buffer conditions, etc.) lacking the radical. Consequently, ^1H longitudinal relaxation time (T_1) in the presence of a radical is given by $\frac{1}{T_1} = k_\rho + \frac{1}{T_{1,0}}$, where one notes that the three different processes contributing to k_ρ will contribute together to the radical induced nuclear T_1 relaxation as measured by an inversion recovery experiment. The self-relaxation rate is thus obtained from the difference of the relaxation rates obtained for the samples with and without the radical:

$$k_\rho = \frac{1}{T_1} - \frac{1}{T_{1,0}} \tag{4.3}$$

The cross-relaxation rate k_{sigma} is obtained from the ODNP experiment as derived in Franck et al. [2]:

$$k_\sigma = \lim_{p \to \infty} \left(\frac{1 - E(p)}{T_1(p)} \right) \left| \frac{\gamma_n}{\gamma_e} \right| \frac{1}{S_{max}} \tag{4.4}$$

Here, $E(p)$ and $T_1(p)$ denote the enhancement and ^1H relaxation times, respectively, measured as function of applied mw power; γ_n and γ_e are nuclear and electron gyromagnetic ratios, respectively; S_{max} denotes the maximum achievable saturation of the unpaired electron EPR spectrum, as discussed in more detail below.

Note that Eq. (4.4) is different from the one that appears in the classical ODNP literature [42] and in the earlier papers of the Han laboratory [89, 88]. The early definition of the cross-relaxation rate assumes that T_1 is independent of temperature, or alternatively that mw-induced sample heating is negligible. We will be referring to this original definition as $k_{\sigma,uncorrected}$ in this text due to the fact that temperature correction is omitted in the classical definition of k_σ.

$$k_{\sigma,uncorrected} = \lim_{p \to \infty} \left(\frac{1 - E(p)}{T_1(p = 0)} \right) \left| \frac{\gamma_n}{\gamma_e} \right| \frac{1}{S_{max}} \tag{4.5}$$

A detailed description of the background and method of this heating correction necessary for the ODNP data analysis was introduced and provided in a review article by Franck et al. **??**. It is important to keep this distinction in mind. Though the "temperature corrected" definition provides the "true" value of the coupling factor [2], the "uncorrected" values are often useful for comparing the numbers with the available early ODNP literature, not only of Han and coworkers [88, 89, 34, 101, 99, 104] but also of Bennatti and coworkers [120, 121, 122, 123, 124], Neudert and coworkers [98], as well as Jeschke, Bordignon, and coworkers [102]. Naturally, the $k_{\sigma,uncorrected}$ values depend on the amount of sample heating and thus on the experimental setup, such as the exact cavity and NMR probe design used, as well as sample conditions, including the amount of salt and nature of the sample. Fortunately, when the latter are kept reproducible the values can be compared between themselves and provide information on the relative differences in hydration dynamics. Note that the coupling factor values compiled in Fig. 4.1 are of the "uncorrected" type, due to the prevalence of these data in the literature.

4.3.2 Saturation Factor

From Eqs. (4.4) and (4.5), it is clear that accurate knowledge of the saturation factor S_{max} is essential for accurately determining the coupling factor and interpreting the ODNP results. This is not trivial, since in nitroxide radicals the unpaired electron spin is strongly coupled to the nuclear ^{14}N nitrogen spin ($I = 1$), and consequently the EPR signal splits into three resonance lines by the hyperfine interaction. For an EPR spectrum consisting of a single line, the electron spin saturation as function of mw power is given by:

$$S = S_{max}\frac{P}{1+P} \tag{4.6}$$

where P is the applied mw power. Since in a typical ODNP experiment CW mw irradiation is applied on resonance with only one out of three EPR transitions of ^{14}N-nitroxide radicals, the extent of the cross talk between the three transitions will determine the value of S_{max}. Consequently, for ^{14}N nitroxide radical, the maximum saturation factor is given by:

$$S = \frac{1}{3} - \frac{2}{3}R \tag{4.7}$$

where $0 \leq R \leq 1$ characterizes the extent of cross talk between the three hyperfine lines under different sample conditions. Accordingly, the saturation factor can vary from $S_{max} = 1/3$ (no cross talk) to $S_{max} = 1$ (complete cross talk) [88, 2, 119, 125]

There are two different processes that can cause change in the ^{14}N quantum number and are responsible for the cross talk between different ^{14}N EPR lines: (i) Heisenberg exchange and (ii) ^{14}N nuclear relaxation (commonly abbreviated as T_{1N}). The Heisenberg exchange rate is proportional to the rate of collisions between the spin labels. Consequently, Heisenberg exchange plays a significant role only for spin probes in nonviscous samples at local concentrations above $0.5mM$. In biomolecular studies, such conditions are rarely encountered in applications of ODNP [88]. In turn, the effect of ^{14}N T_{1N} relaxation rate becomes significant ($T_{1N} \leq T_{1e}$) when spin labels are attached to macromolecules or immobilized on a surface, where the slowing of spin label tumbling motion has been shown to dramatically shorten the ^{14}N T_{1N} [121, 126]. This is the case in the majority of biochemical applications of ODNP, where the probing of water dynamics in the proximity of lipid membranes or the surfaces of proteins or nucleic acids is desired, for which tethered spin labels are employed.

A direct measurement of the saturation factor is complicated and requires either a CW EPR spectrometer capable of double resonance experiments or a pulsed electronnuclear double resonance (ELDOR) equipment [127]. If the electron relaxation time T_{1e}, ^{14}N relaxation time T_{1N}, Heisenberg exchange rate, and strength of the mw irradiation are known it is possible to precisely calculate the saturation factor S_{max} [88, 125, 127]. In practice, the determination of T_{1e} and T_{1N} for nitroxide radicals at room temperature and in aqueous solution requires sophisticated EPR instrumentation and is hardly a routine procedure [128, 126]. Fortunately, for many practical biochemical ODNP applications, the condition $T_{1N} \leq T_{1e}$ is fulfilled and consequently $S_{max} \approx 1$ [88, 126].

An important point to make here, as should be obvious from the previous discussion, is that it is difficult to directly compare the hydration dynamics of the spin labeled macromolecule and a free spin probe under the same experimental conditions. As detailed in publications by Armstrong and Han [88] and Franck et al. [2], characterization of the local water dynamics around a freely tumbling spin probe in solution requires a series of experiments with varying spin probe concentrations for careful determination of S_{max} using ODNP alone.

4.3.3 Interpretation of Measured ODNP Parameters

Here, we summarize the theory commonly applied for the interpretation of the relaxation rates and coupling factor values obtained in ODNP experiments. To translate the coupling factor into a physical picture of local water motion, a model is adopted that describes water diffusion around the spin label. Such model results in a spectral density function (either analytically or numerically) which in turn allows for derivation of the relaxation rates. In this chapter, we use the spectral density function derived based on the Force Free Hard Sphere (FFHS) model [129, 53], which is so far almost exclusively used for the analysis of the ODNP data in the context of obtaining water dynamics in the proximity of a spin label.

The self- and cross-relaxation of the ^1H water nuclei is driven by fluctuations of the electronproton dipolar interactions. The time dependence of these interactions is commonly characterized by a single correlation time τ_c. In the case of water protons interacting with the spin label, this correlation time is dominated by the physical diffusion of water relative to that of the spin label or probe, as follows:

$$\tau_c = \frac{d^2}{D_{H_2O} + D_{SL}} \tag{4.8}$$

where D_{SL} and D_{H_2O} are, respectively, the diffusivities of the spin label and water in the vicinity of the spin label, and d is the distance of minimum approach of water protons to the unpaired electron spin. The connection between relaxation rates and the correlation time is obtained through an analytical spectral density function $\mathscr{J}(\omega, \tau_c)$ obtained from the FFHS model. It provides the transition probability of the given spin relaxation process (T_{1n}, T_{zq}, and T_{dq}) at a given frequency. For dipolar interactions, k_σ and k_ρ relaxations take the form [118]:

$$k_\sigma(\omega_e, \omega_n, \tau_c) = \kappa C(6\mathscr{J}(\omega_e - \omega_n, \tau_c) - \mathscr{J}(\omega_e + \omega_n, \tau_c)) \tag{4.9}$$

$$k_\rho(\omega_e, \omega_n, \tau_c) = \kappa C(6\mathscr{J}(\omega_e - \omega_n, \tau_c) - \mathscr{J}(\omega_e + \omega_n, \tau_c) + 3\mathscr{J}(\omega_n, \tau_c)) \tag{4.10}$$

where κ is a constant given by $\kappa = \frac{4}{10}\pi\gamma_n^2\gamma_e^2 h^2$ and C is the radical concentration.

The coupling factor is consequently given by:

$$\xi(\omega_e, \omega_n, \tau_c) = \frac{(6\mathscr{J}(\omega_e - \omega_n, \tau_c) - \mathscr{J}(\omega_e + \omega_n, \tau_c))}{(6\mathscr{J}(\omega_e - \omega_n, \tau_c) - \mathscr{J}(\omega_e + \omega_n, \tau_c) + 3\mathscr{J}(\omega_n, \tau_c))} \tag{4.11}$$

Note that the κ prefactor cancels out in the coupling factor parameter, as does the dependence on the radical concentration. Thus, if possible, a coupling factor-based analysis is preferred as it eliminates the systematic error that may be present when determining the radical concentration. This is especially important in biochemical preparations where spin labeling efficiency is not always precisely known. That said, it is possible to obtain information on hydration dynamics from k_σ alone, though from our experience, experimental errors resulting in such analysis are typically larger. Up to the determination of k_σ and ξ, no approximations are made except for the well-justified assumption that the interaction of the water protons with the unpaired electron of the spin label is exclusively dipolar. However, to relate ξ to the local water diffusivity, one has to assume a model of motion that preferably results in a closed analytical form for the spectral density function $\mathscr{J}(\omega, \tau_c)$. As mentioned, the most popular model that is almost exclusively used to date for the analysis of relaxivities, including ξ, in terms of hydration dynamics, is the FFHS model, with expression for $\mathscr{J}(\omega, \tau_c)$ given in the following [53]:

$$\mathscr{J}(\omega, \tau_c) = \mathscr{R}\left(\frac{1 + \frac{(i\omega\tau_c)^{1/2}}{4}}{1 + (i\omega\tau_c)^{1/2} + \frac{4}{9}(i\omega\tau_c) + \frac{1}{9}(i\omega\tau_c)^{3/2}}\right) \tag{4.12}$$

In practice, one looks for a correlation time value τ_c that, when using the FFHS model, results in the experimentally obtained coupling factor at a given magnetic field B_0 of typically $0.35T$. Several attempts were made throughout the years to go beyond the FFHS model [130, 131, 129, 53] by both developing more encompassing analytical expressions and more recently by obtaining spectral density function $\mathscr{J}(\omega, \tau_c)$ numerically from molecular dynamics MD trajectories [132, 125, 119].

4.4 Hardware

To date, no dedicated ODNP instrument is commercially available as a complete unit. Thus, essentially every laboratory has an ODNP spectrometer of a different design. Despite the differences, all are built along the same guidelines. At the heart of an ODNP spectrometer lies typically a commercial CW EPR instrument. An overall view

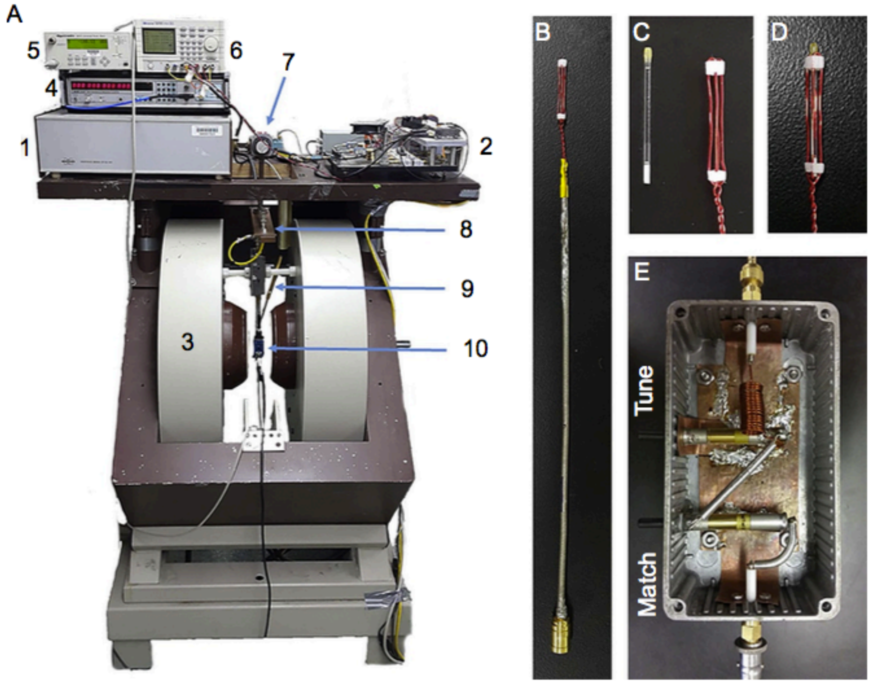

Figure 4.3: (A) Overview of the ODNP instrument employed in the laboratory of Prof. Songi Han, at the University of California Santa Barbara. 1, EPR (Bruker EMX) bridge; 2, ODNP bridge; 3, Electromagnet (Bruker EMX); 4, frequency counter (can be switched between EMX and ODNP bridges); 5, power meter (connected to ODNP bridge); 6, power supply for the ODNP bridge; 7, three port manual waveguide switch (used to switch the EPR resonator between the EPR and ODNP bridges); 8, grounding plate (used to ensure a common ground between the EPR transmission line and NMR RLC circuit); 9, NMR tuning box; 10, EPR cavity (Bruker 4123D resonator). (B) NMR probe. (C) NMR coil and sample. (D) ODNP sample mounted inside the coil. Note that EPR (EMX), NMR (Avance III) consoles, NMR preamplifier, electromagnet chiller, and power supply are not shown in the figure despite being part of the system.

of the ODNP spectrometer in the Han laboratory is shown in Fig. 4.3A. Modifications and additions to the CW EPR spectrometer required for ODNP experiments are listed below:

1. An NMR console capable of low frequency ($15 MHz$) NMR experiments. Though dedicated low frequency NMR spectrometers are available from various vendors, utilizing a heteronuclear (X) channel of an obsolete NMR spectrometer is often a good practical solution.

2. An EPR cavity with high B_1 conversion is critical, so that relatively low mw power $(3 - 10W)$ can saturate the EPR transition of the nitroxide radical. The dielectric cavity 4123D from Bruker Biopsin is an excellent choice since it tends to minimize sample heating for a given strength of mw irradiation, followed by the standard Bruker EPR resonators, such as the super high-Q and the 4102ST cavities. The Bruker ENDOR cavity EN 801 suffers both from low B_1 conversion of the mw as well as from low NMR filling factor, and thus is a poor choice for ODNP even after a resonant NMR circuit is added. However, this is by far not an exhaustive survey, and alternative cavity designs are conceivable [102, 42].

3. A low frequency NMR probe that is compatible with an existing EPR cavity. Several designs were described in the ODNP literature [52, 2, 42].

    (a) The current design that has been in use in our laboratory for several years is shown in Fig. 4.3B and C. The coil wires are oriented along the long axis of the resonator to exert minimal distortion of the mw resonator mode, while concurrently designed to maximize the NMR filling factor. We found this design to perform well in both the rectangular TE_{102} (Bruker 4102ST) and in dielectric cavities with a TE_{011} like mode (ER 4119HS, ER 4122HSQE, and ER 4123D). The ODNP sample consisting of $3 - 4\mu l$ of solution sealed inside the quartz capillary is mounted on the probe (Fig. 4.3C and D). This NMR probe connects to the NMR tuning box (Fig. 4.3E) via an SMB connector. The piece of coaxial semi-rigid cable between the coil and the SMB (SubMiniature version B) RF connector allows for the insertion/removal of the probe without the need to unmount the tuning box. Despite the overall utility and efficiency of this probe, there are several drawbacks in this current design: (i) Sample exchange requires insertion and removal of the whole NMR probe. (ii) The probe position is set by eye relative to the EPR cavity, which reduces the reproducibility of the experiment especially when performed by different experimentalists. (iii) The ODNP sample is held in place by friction against the Teflon sample/coil holders (Fig. 3D), which results in their wear and tear and eventually requires rebuilding of the probes.

   (b) We have recently developed a more robust NMR probe where the tuning box and NMR coil are combined into a single unit that is mounted from the bottom on the EPR cavity (Fig. 4.3AC). In this new design, the sample is fixed in place by a separate sample holder that can be moved independently of the NMR probe, thus allowing for one to change the sample without removing the NMR probe (Fig. 4.3B).This design negates the need to carefully reposition the NMR probe each time the system is assembled, and consequently reduces operator error as well as wear and tear on the probe.

4. Highpower $(3 - 10W)$ CW *mw* source with a suitable computer interface for finely controlling the output *mw* power. The initial design used in our laboratory is described in detail in [52]. The current version differs only in minor details.

5. A *mw* power and frequency meter to carefully monitor the *mw* frequency and power during the course of the ODNP experiment. As the *mw* power is commonly varied by an attenuator and the absolute *mw* power is not set, one must measure the incident *mw* power in order to make accurate and reproducible measurements.

Putting together the hardware alone will only allow for a manually controlled ODNP experiment. For routine applications, software that allows for automation is extremely beneficial. In fact, for delicate biological samples, automation of the entire ODNP experiment is necessary to keep experimental time as short as possible to minimize sample damage. In practice, to fully automate the experiment, one must automatically:

1. Loop through the NMR FID and inversion recovery acquisitions for the enhancement and T_1 measurements.
2. Set the mw power applied to the sample for each FID experiment in the enhancement series and for every inversion recovery experiment in the T_1 series.
3. Log the mw power applied to the sample throughout the experiments.

4.5 Data Acquisition

The specific goal of an ODNP experiment is to measure the ODNP enhancement and relaxation data for obtaining the coupling factor that in turn can be translated into physical parameters describing local hydration dynamics in close proximity ($< 1nm$) of an unpaired electron of a spin probe.

/bin/bash: /enumer: No such file or directory The common practice in the Han lab is to seal one side with the CritosealTM tube sealant and the second side with melted capillary wax (Fig. 4.3C). However, a polymer-based capillary tubing has also been used [115, 114]. It is very important to ensure good quality of the seal so that the sample does not evaporate due to the prolonged mw heating during an ODNP experiment.

In practice, ODNP experiments are preceded by a CW EPR measurement, with two goals: (i) to obtain the resonance frequency/field that is typically set to the maximum of the center peak of the nitroxide spectrum, i.e., the zero crossing of the center $m_I = 0$ line of the cw EPR spectrum and (ii) to quickly prove the samples integrity and preparation quality. Here, since ODNP reports on the average local water dynamics in close proximity to the spin probes/spin labels, it is of utter importance that the spin is localized in the target environment. Similarly, it is necessary to ensure that all unattached spin label is carefully removed. It is important to keep in mind that when two components are present in the EPR spectrum, the ODNP measurement will report on an average value representing water dynamics within all spin label environments present in the sample. Consequently, samples exhibiting only a single component in the EPR spectrum will simplify interpretation of the results.

During the acquisition of an EPR spectrum, the EPR cavity is critically coupled and the *mw* frequency is set. Since the same transmission line is used to couple the EPR and ODNP bridges, the same *mw* frequency and cavity coupling can be used for both the EPR and ODNP experiments.

The full ODNP measurement consists of three separate series of experiments, two performed on the sample with a radical: (i) NMR enhancement as function of *mw* power (Fig. 4.5A) and (ii) series of inversion recovery experiments to obtain T_1 relaxation as function of applied *mw* power (Fig. 4.5B). A third experiment, inversion recovery to obtain $T_{1,0}$, is performed on a sample of identical composition, except without the paramagnetic radical. It is of great importance to ensure that the concentration of all the constituents is equal in both samples. Ideally in the "background" sample, the spin label is replaced by its reduced analog. For example, in case of spin labeled proteins, MTSL (Fig. 4.1B) is replaced by *d*-MTSL (Fig. 4.1C). In practice, this can often be omitted if the *d*-MTSLs perturbation on the physical properties and ^1H water relaxation of the system is negligible.

Typically, 15 - 20 experimental values are measured for the ODNP enhancement curve and 5 - 7 for the $T_1(p)$ series, both spanning the same range for the applied *mw* power. In addition, one $T_{1,0}$ experiment is performed on the sample without the radical. It is possible to acquire a full $T_{1,0}(p)$ series. The goal of such a series is to ensure sample integrity over the temperature range covered during the ODNP measurement. Both $T_1(p)$ and $T_{1,0}(p)$ are predicted to increase linearly with *mw* power with the same slope [2, 133]. Ensuring the latter provides for a good self-consistency check, which is especially recommended if phase transition, sample decomposition, or other changes to the sample are anticipated with temperature increase.

For all NMR experiments, we routinely employ a standard four-step CYCLOPS phase cycle [134]. From our experience, this results in a SNR of 4050 for an unenhanced NMR signal. Note that the lineshape is determined by the homogeneity of the magnetic field inside a typical EPR magnet, so in practice the NMR lineshape is never an ideal Lorentzian. If the sample and coil are properly positioned inside the EPR resonator, the lineshape should be equal or very similar for the enhanced and unenhanced signals (Fig. 4.5F). Note that one should avoid a situation where only part of the NMR line is inverted during an ODNP experiment, as this will result in large errors when normalizing the spectra by the integral of the unenhanced signal.

The automated ODNP experiment typically takes 2 to $3h$ and will include a $5min$ delay at the beginning of the experiment after the mw source is turned on for the first time to allow the high power amplifiers to warm up, as well as a $10s$ delay every time the mw power is changed to a different value to allow for the sample temperature to reach a steady state.

4.6 Data Analysis

4.6.1 Raw Data Analysis

This section describes the step-by-step procedure to analyze the experimental ODNP data. The procedure outlined below assumes that raw NMR enhancement spectra have been integrated, normalized to the unenhanced integral, and dimensioned with the corresponding mw power to yield $E(p)$. Also that the inversion recovery experiments were integrated and fit to extract the T_1 and that each T_1 value has been dimensioned with the corresponding mw power to yield $T_1(p)$.

An example of such processed raw ODNP dataset obtained for a spin label attached to a surface exposed cite of a globular protein is shown in Fig. 4.5 ($[protein] \approx [spinlabel] \approx 200\mu M$). The ^1H signal enhancement plotted against applied mw power is shown in Fig. 4.5C, and T_1 and $T_{1,0}$ relaxation times as function of mw power shown in Fig. 4.5D. Note that the increase in T_1 with an increase in applied mw power is due to dielectric sample heating. To provide a concrete example, we provide in parenthesis the values obtained for the experimental data presented on Fig. 4.5 for each step of the analysis outlined below.

The first step is to fit the $T_1(p)$ series using a first or second order polynomial to obtain the T_1 rate for each point in the enhancement series. For this particular dataset, the first order polynomial gave a satisfactory fit (red dashed line in Fig. 4.5D). The T_1 times are then interpolated for all mw power values used in the enhancement series. The interpolated values are used to calculate the temperature corrected cross-relaxation rate as function of applied mw power according to 4.4; this is plotted in Fig. 4.5E as black squares. The uncorrected cross-relaxation rate is also shown for comparison in Fig. 4.5E as green circles. Since the mw power dependence of EPR saturation is known and given by Eq. (4.7), the $k_\sigma S(p)$ and $k_{\sigma,uncorrected}S(p))$ curves can be fitted to:

$$k_\sigma S(p) = \frac{k_\sigma S_{max} p}{a + p} \tag{4.13}$$

to obtain $k_\sigma S_{max}$ and $k_{\sigma,uncorrected}S_{max}$, respectively ($a$ is a scaling factor and is set as a free parameter in the fit). Since in most cases of interest $S_{max} \approx 1$ is given, one obtains the values for k_σ and $k_{\sigma,uncorrected}$. The next step is to calculate the self-relaxation value k_ρ from $T_1(p = 0)$ and $T_{1,0}(p = 0)$ according to Eq. (4.3). Subsequently, the corrected ξ and uncorrected coupling factor $\xi_{uncorrected}$ is calculated according to Eq. (4.2).

4.6.2 Data Interpretation

The coupling factor and the self- and cross-relaxation rates are parameters directly obtained from the ODNP experiment. What one would like to do next is to convert the coupling factor to a more intuitive and physical measurement of water dynamics, such as the correlation time or a local water diffusion coefficient.

In order to convert the coupling factor into a diffusion correlation time, one has to assume a model for the spectral density function. Here, we provide an example of ODNP data analysis using the FFHS model [53]. For a given coupling factor, a correlation time is obtained by solving Eq. (4.12) for a value of the magnetic field as used in the experiment, thus far typically $B_0 = 0.35T$ for data shown in Fig. 4.5C – E: $\tau_c = 71ps$ from the temperature corrected analysis.

For a better understanding of the water properties in a biochemical system, it is always illustrative to have a comparison with the properties of bulk water. For a nitroxide spin probe dissolved in bulk water, the coupling factor was shown to be $\xi_{bulk} = 0.27$, which corresponds to a correlation time $\tau_{c,bulk} = 54ps$, as derived from the FFHS model. Note that the typical value for the bulk water obtained without the temperature correction is $\xi_{bulk} = 0.33$ and consequently $\tau_{c,bulk} = 33.3ps$, as shown and discussed in Franck et al. [2].

A more recent approach to analysing water diffusivity on the surface of biomolecules is to use the k_σ values directly to compute the retardation (ρ) in water diffusivity by

$$\rho = \left(\frac{k_{\sigma,site}}{k_{\sigma,bulk}}\right)^{-1} \tag{4.14}$$

This approach allows for a model free analysis of the water diffusivity. However, it is helpful to understand how the k_σ retardation changes with retardation in correlation time $\tau_{c,site}/\tau_{c,bulk}$, shown in Fig 4.6B. The FFHS model was used here to calculate a direct relationship between k_σ and τ_c, while this does introduce a model it helps in basic understanding of what k_σ means [79, 2]. This approach has one main advantage over previous approaches employing the coupling factor ξ to calculate a correlation time τ_c. That is k_σ has dependence on only the ps $(1/\omega_e)$ timescale of motion whereas ξ depends on both the ps and ns timescale coming from the $1/\omega_e$ and $1/\omega_n$ dependence of the k_ρ relaxation rate, Eq. 4.10. Note the terms in k_σ, $\mathscr{J}(\omega_e \pm \omega_n, \tau_c)$, at $B_0 = 0.35T$ $\omega_e = 10GHz$ and $\omega_n = 15MHz$ the term $(\omega_e \pm \omega_n, \tau_c) \approx (\omega_e, \tau_c)$ and thus k_σ only has dependence on the $1/\omega_e$ (ps) timescale.

In the context of evaluating protein surface hydration water retardation, the convolution of ns and ps timescales of motion in the coupling factor ξ and ultimately the correlation time can be problematic due to the presence of water that is bound to the protein surface and fluctuating on the ns timescale. The presence of bound water (BW) can lead to an exaggerated apparent retardation factor for surface water diffusivity [44]. Therefore, it is beneficial and often necessary to probe the ps and ns timescales separately. We separate these timescales of motion following the procedure outlined by Franck et al. [51].

Because the terms $\mathscr{J}(\omega_e \pm \omega_n, \tau_c)$ can be written as $\approx$ $\mathscr{J}(\omega_e, \tau_c)$, k_σ and k_ρ can be simplified to Eq. 4.15 and 4.16. Of course we get that k_σ is only dependent on ω_e however we're still left with k_ρ that is dependent on both ω_e and ω_n. We subtract off the dependence on ω_e from k_ρ using k_σ and define a new term k_{Low} (Eq. 4.17) that only depends on ω_n or ns timescale motions.

$$k_\sigma \approx \kappa C 5 \mathscr{J}(\omega_e, \tau_c) \tag{4.15}$$

$$k_\rho \approx \kappa C (7\mathscr{J}(\omega_e, \tau_c) + 3\mathscr{J}(\omega_n, \tau_c)) \tag{4.16}$$

$$k_{Low} = \frac{5}{3}k_\rho - \frac{7}{3}k_\sigma = \kappa C \mathscr{J}\left(\omega_n, \tau_c\right) \tag{4.17}$$

The k_{Low} relaxation rate is sensitive to motion on the $1/\omega_n$ ($1-100s$ of ns) timescale. In the hydration layer of proteins, this timescale represents water molecules that are bound to and rotating with the protein [44]. Thus, it is necessary to account for the rotational motion of the protein in the total spectral density function representing k_{Low} as

$$\mathscr{J}_{total} = (1-n)\mathscr{J}_{FFHS} + n\mathscr{J}_{rot} \tag{4.18}$$

Here, $\mathscr{J}_{rot}$ is the rotational spectral density function that takes the rotation of the protein into account and n is a linear weighting factor that represents the fractional population of bound waters, rotating with the protein, and freely translating waters moving independently of the protein. It is important to note that the translational motion, corresponding to diffusive water, contributes a constant value to k_{Low} that is invariant to changing correlation time because of the frequency that k_{Low} probes. The spectral density function describing the rotational motion of the protein is given by

$$\mathscr{J}_{rot} = \left(\frac{\tau_{rot}}{1-(i\omega_n\tau_{rot})^2}\right) \tag{4.19}$$

$\mathscr{J}_{rot}$ is shown in Fig. 4.6A by the blue dashed line alongside $\mathscr{J}_{FFHS}$ in the red dashed line. The k_{Low} relaxation rate is enhanced on surfaces that tumble on the $1/\omega_n$ timescale and feature BW. There are two factors that lead to enhancements in k_{Low}; the fractional amount of bound waters, n, and the timescale of the protein rotational motion, τ_{rot}. The enhancement in k_{Low}, $\left(\frac{k_{Low,site}}{k_{Low,bulk}}\right)$, is shown as a function of the protein rotational correlation time, τ_{rot}, for $n = 0 \rightarrow 1$ in Fig. 4.6C. When comparing hydration water around surface sites on the same biomolecule, it is reasonable to assume that the rotational correlation time of the biomolecule, τ_{rot}, will be similar for each mutant. Thus, differences in k_{Low} enhancement can be attributed to differences in the relative population of BW, here n. However, similar interpretations of k_{Low} enhancements between biomolecules with significantly different τ_{rot} would not be valid, and must be limited as a coarse read out of whether BW is present or not at the given site. To be clear, BW must be present to detect any amount of k_{Low} enhancement.

4.7 Ongoing Development

4.7.1 Frequency Swept ODNP

One of the challenges facing the ODNP technique in the protein hydration water field of study is that there are often multiple timescales of motion of water molecules present on the protein surface. The challenge is that ODNP in it's current form and implementation can only report on two disparate timescales of motion. There is no second or third dimension to the experiment to yield more site specific information than these two timescales of motion. Going forward with this technique it would be advantageous to report on multiple correlation times at any specific timescale as well as pick out parameters such as the distance of closest approach d from Eq. 4.8 as a fitting parameter instead of as a guess. One very promising approach is to measure ODNP parameters as a function of the static magnetic field B_0 and thus change the timescale of motion that the ODNP technique is sensitive to. This section will detail a past attempt at field swept ODNP and shed light on efforts that are ongoing.

Measuring k_σ as a function of static magnetic field is in essence measuring k_σ as a function of the frequency of motion. By changing the field one changes the electron larmor frequency ω_e and you change the frequency at which one probes the spectral density function by doing so it becomes possible to experimentally measure the shape of the spectral density function. Once the shape of the spectral density function is known it's possible to fit the experimentally measured spectral density functions to a multi component $\mathscr{J}_{FFHS}$ varying the correlation time and the respective weight and determine more than one correlation time of motion as done in [135]. From Fig. 4.6 it is apparent that to scan the entire dispersion present in the spectral density it is necessary to measure k_σ over $\omega_e = 1 \rightarrow 50GHz$. It is not feasible to measure k_σ over this entire range of frequencies simply because of spectrometer limitations as well as the absorption band of water above $36GHz$ preventing transmission of microwaves. The limitation is not with the radio frequency technology or with the magnet capabilities but with the current microwave technology that would limit the bandwidth of such a spectrometer to $2 - 18GHz$.

The success of such a wideband EPR spectrometer is dependent on an appropriate resonator design that maintains the same microwave resonant mode throughout the frequency range. This is the main challenge of the spectrometer design as the development of such a resonator requires sacrificing on the filling factor or B_1 conversion factor of the resonator. Thorsten Maly at Bridge 12 has come up with an alternative solution and that is to use a series of surface planar resonators where the resonant frequency is easily tuned by a gap in the copper trace, unpublished work. In this design each resonator is designed for a specific frequency and easily swapped out by the successive resonator. Thus it is possible to perform such a frequency swept ODNP experiment.

The remaining challenge will be overcoming the tremendously long experiment time because each ODNP experiment currently takes 2 hours. One promising avenue for reducing the experiment time is to reduce or eliminate the microwave heating.

4.7.2 Reducing Microwave Heating

Another challenge facing the ODNP technique is the microwave induced sample heating that occurs during the course of the experiment. Obviously this limits the samples that ODNP can apply to as certain proteins cannot survive increased temperatures. More so this increases the total experiment time which makes two dimensional ODNP experiments sometimes prohibitively long. Recall from section 4.5 that we record the NMR enhancement and the proton T_1 as a function of power. The T_1 measurements are designed to account for the microwave heating because the proton T_1 is sensitive to temperature and allows us to accurately calculate k_σ because the temperature change is accounted for. However if the microwave did not heat the sample there would be no need to measure the proton T_1 as a function of power. In fact in absence of all microwave induced heating it would only be neccesary to measure the full microwave power proton enhancement and the full microwave power T_1 and that would accurately allow one to calculate k_σ. The proton T_1 would be measured at full power simply because of the dramatically increased signal to noise ratio that comes with the ODNP enhancement.

So how do we overcome microwave heating? First we must find out what the actual source of the heating is. The biological sample sits in a quartz capillary in the center of the resonator. The resonator is designed to maximize the magnetic field from the incoming microwaves at the sample position and minimize the electric field. For poorly tuned resonators, low Q or off resonance, this the electric and magnetic field are no longer separated and there can be a significant electric field density at the sample position. The heating that occurs at the sample is from a non zero density of the electric field at the sample position. Here the electric dipole of the magnetic field interacts with the electric dipole of the water molecules, inducing molecular rotation, friction, and heating. Therefore, to minimize or eliminate sample heating it is necessary to have minimal electric field density at the sample position. Here proper resonator design can minimize the electric field at the sample position. However, a properly tuned and resonant microwave resonator can also minimize the electric field at the sample position. Thorsten Maly, again Bridge 12, when developing commercialized instrumentation for ODNP realized that the sample heating that occurs during the experiment was detuning the resonator and thus further causing microwave heating, unpublished work. Going further he found that if he adjusted the microwave frequency to stay with the cavity resonance that the proton T_1 did not increase with increased microwave power and further that the sample temperature did not increase. This realization proves very promising because it can significantly cut the experimental time from hours to minutes allowing more multiplexed studies and also allowing for ODNP to be applicable to more delicate samples.

In collaboration with Bridge 12 and Thorsten Maly we are developing automated instrumentation that constantly keeps the microwave source tuned to the resonant position of the microwave cavity. We expect this will tremendously improve the applicability of the ODNP experiment.

4.8 Conclusion

The development in both theory and technique over the years has placed ODNP as a prominent technique in studying surface water dynamics. The techniques presented here are considered state-of-the-art for ^1H ODNP relaxometry at X-band EPR frequency for the study of hydration dynamics. In the next chapter 2 we will go through the application of ODNP to globular proteins in an attempt to rationalize the perturbation that occurs to the hydration water from the protein surface.

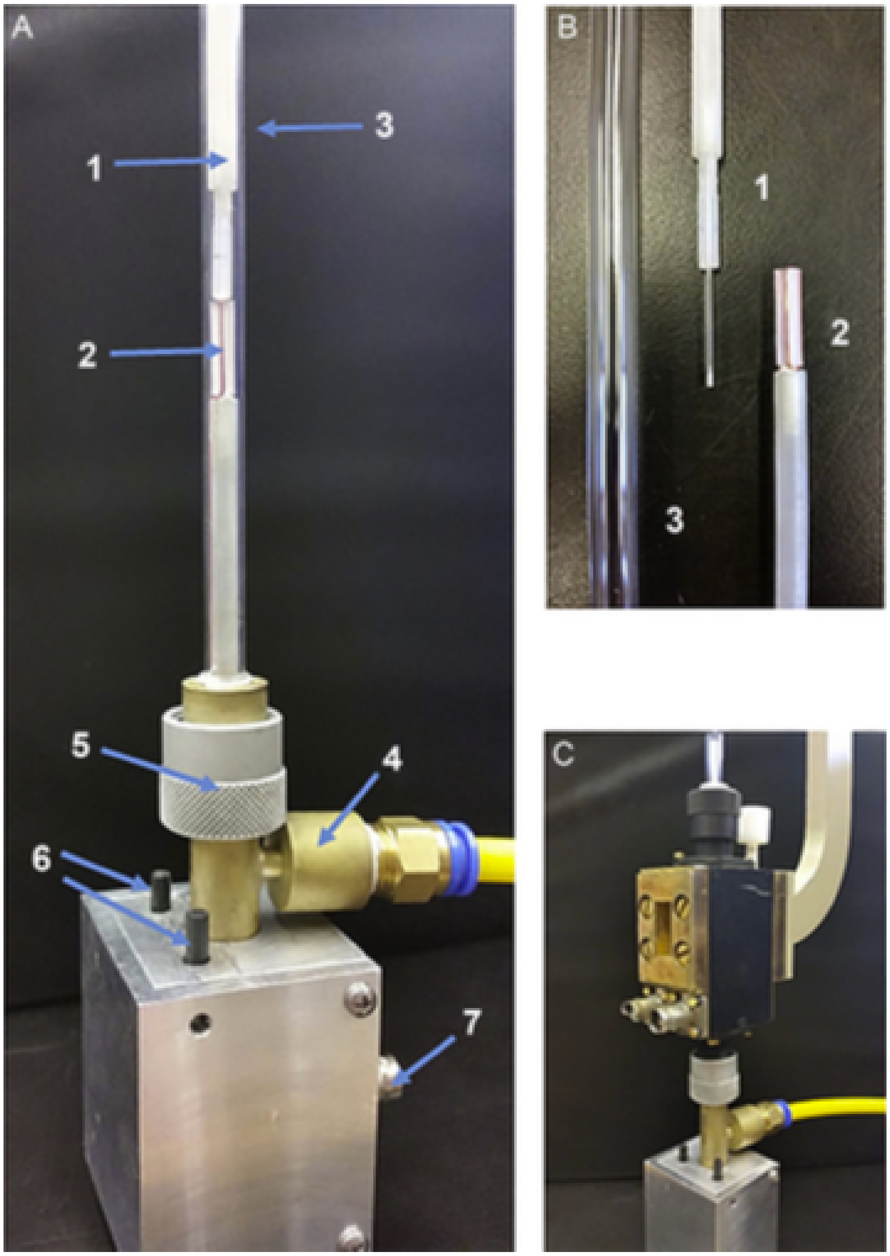

Figure 4.4: (A) Overview of the new NMR probe designed for ODNP. 1, sample holder and sample; 2, NMR coil; 3, quartz tube for aligning the sample holder and the NMR coil; 4, connector for air flow; 5, catch nut for fixing the assembly to the bottom of the microwave cavity; 6, adjustment rods for the match and tune capacitors of the RLC circuit; 7, BNC female jack for connecting to the NMR spectrometer. (B) 1, layout of the sample and sample holder; 2, the NMR probe windings in the saddle coil configuration; 3, the quartz tube used to align the sample into the NMR probe. (C) Picture of how the NMR probe assembly fits inside of the EPR cavity. Note, the cavity shown is Bruker 4102ST which is not the routine cavity used for ODNP.

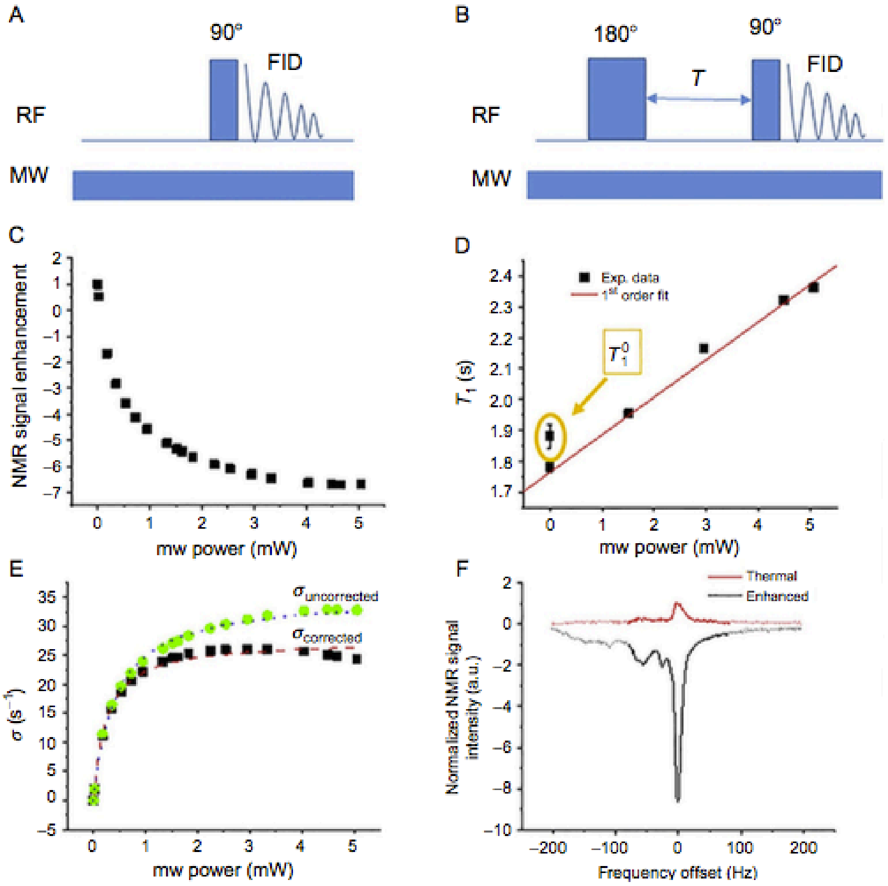

Figure 4.5: (A) Pulse sequence of the ODNP experiment (mw power is incremented). (B) Pulse sequence for the T_1 series experiment (note that both mw power and T delay are incremented for a pseudo 2D-dataset). (C) Normalized ODNP enhancement series. (D) Processed data for the T_1 series and $T_{1,0}$ experiment. (E) $k_\sigma S(p)$ curves with the temperature correction (black squares) and without (green circles); fits to Eq. (4.4) are shown by red dashed line and blue dotted line, respectively. (F) Enhanced ($p = 5mW$) (black) and unenhanced (red) NMR spectra; part of the frequency range used for signal integration is highlighted in bold. The data shown are acquired from an MTSL labeled D41C mutant of Chemotaxis Y protein at $200\mu M$ concentration.

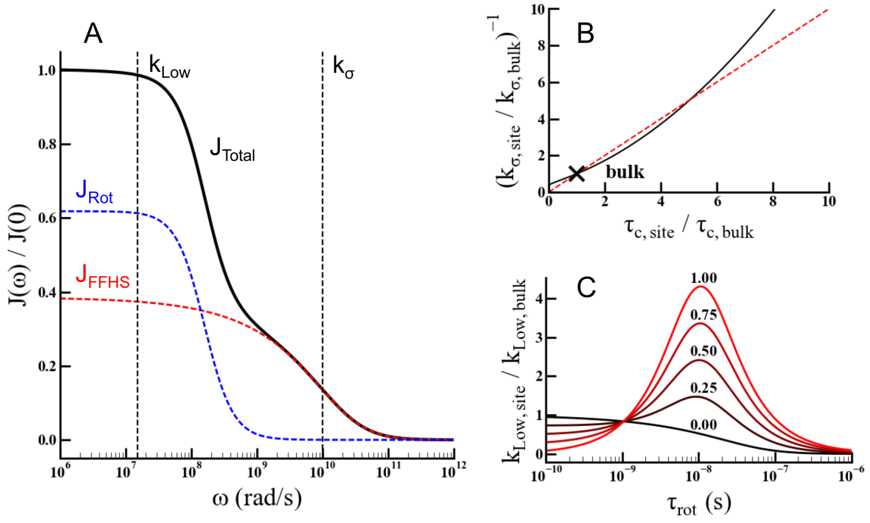

Figure 4.6: Shows the relevant relaxation rates extracted from ODNP. A, shows the FFHS spectral density function (red), the lorentzian based rotational spectral density function (blue) and the total spectral density function calculated from Eq 5 assuming an equal weighting between rotational and FFHS spectral densities (black). The frequency in which k_σ and k_{low} probe the total spectral density is shown in A. B, shows the approximate relationship between the retardation in k_σ and the retardation in the translational correlation time τ_c in black, the red dashed line indicates the diagonal, and the bulk water value is indicated with the black (x). C, shows the enhancement in k_{Low} as a function of the rotational correlation time and the relative weighting (n) between $\mathscr{J}_{rot}$ and $\mathscr{J}_{FFHS}$ indicated above the respective line.

Chapter 5

Home-Built Pulse EPR Spectrometer Featuring an AWG

5.1 Abstract

We present arbitrary control over a homogenous spin system, demonstrated on a simple, home-built, electron paramagnetic resonance (EPR) spectrometer operating at $8-10GHz$ (X-band) and controlled by a $1GHz$ arbitrary waveform generator (AWG) with $42dB$ (i.e. $14-bit$) of dynamic range.

Such a spectrometer can be relatively easily built from a single DAC (digital to analog converter) board with a modest number of stock components and offers powerful capabilities for automated digital calibration and correction routines that allow it to generate shaped X-band pulses with precise amplitude and phase control. It can precisely tailor the excitation profiles "seen" by the spins in the microwave resonator, based on feedback calibration with experimental input. We demonstrate the capability to generate a variety of pulse shapes, including rectangular, triangular, Gaussian, sinc, and adiabatic rapid passage waveforms. We then show how one can precisely compensate for the

distortion and broadening caused by transmission into the microwave cavity in order to optimize corrected waveforms that are distinctly different from the initial, uncorrected waveforms. Specifically, we exploit a narrow EPR signal whose width is finer than the features of any distortions in order to map out the response to a short pulse, which, in turn, yields the precise transfer function of the spectrometer system. This transfer function is found to be consistent for all pulse shapes in the linear response regime. In addition to allowing precise waveform shaping capabilities, the spectrometer presented here offers complete digital control and calibration of the spectrometer that allows one to phase cycle the pulse phase with 0.007° resolution and to specify the inter-pulse delays and pulse durations to $250ps$ resolution. The implications and potential applications of these capabilities will be discussed.

5.2 Introduction

Typically, pulsed X-band electron paramagnetic resonance (EPR) performance suffers from insufficient excitation bandwidths. The EPR spectra of nitroxide-labeled macromolecules typically span $80MHz$ when motionally averaged and up to $200MHz$ in the rigid limit at X-band [136, 137]. Even a state of the art spectrometer with a $1kW$ traveling wave tube (TWT) amplifier yields a 90° time on the order of $10ns$, which corresponds to a bandwidth that can barely excite a $200MHz$ bandwidth. Furthermore, the frequency-domain excitation profile of a typical rectangular pulse is far from uniform over this bandwidth [138].

One can obtain superior control over the spin system, in particular over the excitation profile, by arbitrarily shaping the amplitude and phase of microwave pulse waveforms as a function of time. Such arbitrary waveform generation (AWG) has previously been implemented for specific, customized quantum computing applications [139, 138, 140].

Also, the NMR literature has extensively shown that arbitrarily shaped pulses can excite spins over a dramatically wider bandwidth than rectangular pulses of the same power, provide highly uniform excitation profiles [141], excite sharper spectral slices [142], as well as permit extraordinary control over even coupled spin systems [143]. In fact, it could be said that AWG pulse shaping induced a paradigm shift in NMR, and a similar impact would be expected if AWG pulse shaping in X-band EPR became widely available, versatile, and precise. Indeed, there has already been much progress in the last 12 years towards developing AWG-capable EPR spectrometers by modifying commercial or other preexisting instruments [144, 145, 146].

A flexible, modular platform, as pursued in this development, that seamlessly combines the capabilities of a standard EPR spectrometer with the extensibility needed to perform precisely controlled, phase-coherent AWG would permit one to address a variety of specific issues. The ability to uniformly excite either the entire spectrum or to cleanly excite portions thereof would in particular benefit two-dimensional (2D) EPR and experiments involving indirect detection. These include double electronelectron resonance (DEER) [147], solution-state 2D electronelectron double resonance (2D-ELDOR) [148, 149, 150], and hyperfine sublevel correlation spectroscopy (HYSCORE) experiments [151, 152]. These three techniques alone have demonstrated a prominent and growing importance throughout biochemistry by, respectively: providing a tool for measuring nm-scale distances and distance distributions, probing questions about the interactions between proteins and lipid membranes, and allowing one to map out the local solvent environment in glassy sample. Indeed, recent work has already shown [144] that AWG capabilities can improve the sensitivity of DEER experiments. More generally, precise excitation is a key prerequisite to enable efficient transfer through multiple coherence pathways, such as in double quantum coherence (DQC) distance measurements, which could provide potential advantages over DEER in terms of sensitivity, in the ability to probe smaller distances, and in allowing one to extract new types of geometric information [153, 154, 155]. In practice, such a sensitivity enhancement requires the ability to excite nearly all spins in a sample here, optimized AWG pulses offer a potential route for achieving wider excitation bandwidths, while relying on amplifiers with a standard ($1kW$) power output. Meanwhile, uniform broadband saturation would improve dynamic nuclear polarization techniques, easing data interpretation by achieving quantitative maximal saturation ($S_{max} = 1$) of nitroxide probes under all sample conditions, in contrast to the present situation where the maximal saturation can vary dramatically for spin labels freely dissolved in solution vs. attached to polymer chains or surfaces [88, 127]. To achieve the greatest possible benefits for any of these techniques, it is important not only to implement AWG capability in the spectrometer but also to be able to seamlessly and coherently "switch on" this capability for any or all portions of a standard EPR pulse sequence. Such a seamless implementation of AWG will ultimately allow for EPR experiments whose pulse sequence evolve in active feedback with the detected signal, similar to that previously seen in laser spectroscopy [156], with shaped pulses optimized on-the-fly, allowing optimal spin rotations even in cases where certain experimental parameters might not be well characterized.

Earlier work in EPR that sought to overcome the long known limitations of rectangular pulses involved implementation of composite pulses [157], stochastic excitation [158], and tailored pulses [159]. These pulses offered more uniform excitation and improved signal-to-noise when compared to rectangular pulses; however, they still do not employ fully arbitrary pulse shaping capabilities and therefore did not permit arbitrary control over a spin system. This is only because AWG capabilities in EPR, especially at X-band frequencies and higher, remain a relatively new technology. Only within the last few years have arbitrary pulses with ns amplitude and phase resolution been investigated for X-band EPR. AWG radio frequency pulses, such as adiabatic rapid passages [160, 161] or Frank sequences [162] have been shown capable of providing broadband excitation, even with limited irradiation power. Recent studies have begun to employ microwave AWG pulses and have shown promise for performing broadband EPR excitation [146], improved evaluation of dipolar couplings via DEER [144, 145], dead-time reduction in high resonator quality factor (Q-factor) [163], and ultra-wideband inversion of nitroxide signals [144]. Despite these advances, relatively few spectrometers, thus far, feature arbitrary waveform generation capabilities in the X-band ($8-12GHz$) frequency regime [140, 144, 145, 163] and many of those rely on modified commercial instruments as the main platforms [144, 145]. This strategy offers the enormous benefit of allowing the user to operate within a familiar software environment, and on hardware that is already engineered to a high level of precision and verified to be fully functional. However, AWG spectrometers based on commercial instruments require integration with the commercial software, decreasing design flexibility at the current state.

A substantial amount of versatility is added if the spectrometer is home-built to be centered around a DAC (digital to analog con verter) board that operates as the main control unit a strategy primarily used in quantum computing applications [164]. This approach is necessary, for instance, if one wishes to seamlessly implement and update corrections for the resonator bandwidth and/or for amplifier saturation effects applied to the entire waveform (i.e. to all pulses simultaneously), or if one wishes to calculate the shape of an analytically specified waveform on the fly or account for variable pulse rise and fall times when calculating delays. In this study, we demonstrate that the flexibility of the design as presented here permits seamless and coherent integration of AWG capabilities into standard EPR experiments and yields entirely new opportunities. While wideband excitation has been demonstrated at X-band frequencies, most notably in the recent work by Spindler et al. [145, 146] and Doll et al. [144], many applications might rely heavily on optimizing pulses that are insensitive with respect to variations in offset and/or misset of, respectively, the pulse frequency and amplitude. Therefore, it is important to explicitly demonstrate that arbitrary shaped pulses can invoke precisely the desired spin response. In this work, we map out the excitation profile of arbitrarily shaped pulses as a function of resonance offset. In the linear response regime (tip angles of $< 30^\circ$), this excitation profile corresponds to the frequency profile of the pulse (i.e. the Fourier transform of the pulse waveform). By analyzing the response from the spins, we can thus define a transfer function which should be independent of pulse shape and which we can subsequently use to correct the shape of various pulses, as demonstrated here for square, sinc, and Gaussian pulses. We find that we can control the shape of the pulses, as seen by the spins, with high fidelity.

5.3 Experimental

A stand-alone, home-built, AWG X-band EPR spectrometer was designed to easily and precisely manipulate the spin systems of samples that could be of biological interest. A $1GHz$ digital-to-analog converter (DAC) board serves as the central control and timing unit of the spectrometer, in addition to fulfilling its primary role of controlling the amplitude ($42dB$ dynamic range) and phase (0.007° resolution) of an arbitrary waveform with $1ns$ time resolution. The resulting pulse waveform can span a $1GHz$ bandwidth that far exceeds the $200MHz$ bandwidth of a typical nitroxide spectrum. A Python-based programming platform interacts with the spectrometer to easily program phase-coherent pulse sequences that can include square or arbitrarily shaped pulses with arbitrarily timed effective pulse lengths and inter-pulse delays.

5.3.1 Hardware

The YIG-tuned oscillator (Fig. 5.1 #2) outputs a coherent microwave carrier between 8 and $10GHz$ at $10dBm$. As described in Appendix A.2.3, the output frequency of this carrier is computer-controlled. This X-band carrier wave next passes through a preamplifier (MiniCircuits ZX60-183+, Fig. 5.1 #3, Appendix A.2.3), reaching a power of $18dBm$ before passing through an IQ mixer (Marki Microwave IQ-0618 L XP, Fig. 5.1 #6) that shapes the amplitude and phase of the microwave waveform, which leaves the mixer at a power of about $10dBm$. The time-varied voltage (up to $10 - 13dBm$) modulation across the two quadrature IF (i.e. intermediate frequency) ports of the IQ mixer that define the arbitrary pulse shapes are controlled by the DAC board (Appendix A.2.6) with $1ns$ time resolution, i.e. a $1GHz$ bandwidth, (see Figs. 5.1 #4 and #2). Thus, the FT of the time-domain pulse shape, i.e. the frequency profile of the waveform exiting the IQ mixer, has an arbitrarily controlled profile in frequency space that spans $\pm 500MHz$ relative to the frequency of the carrier wave. Equivalently, the spectrometer controls amplitude and phase of the X-band pulse sequence with $1ns$ time resolution.

Next, the microwave pulses are pre-amplified by $24dB$ to $14dBm$ (MiniCircuits ZX60-183+, Fig. 5.1 #10) and further amplified by a parallel array of solid-state amplifiers (Advanced Microwave PA2803-24, Fig. 5.1 #10, Appendix A.2.3) to a peak amplitude of $41dBm$ ($12 - 13W$), before traveling through a circulator (Cascade Research X-43-2, Fig. 5.1 #11) into the microwave resonator (Bruker BioSpin ER4118X-MD5, Fig. 5.1 #12). For all experiments here, the resonator was kept at room temperature in a static magnetic field of $0.35T$ (Fig. 5.1 #1). The circulator then directs the returning EPR signal, along with the resonator ring-down (Fig. 5.1 #11), towards the heterodyne detector (Fig. 5.1 #14 #20). The quadrature heterodyne detector (Fig. 5.1 #14 #20), is a standard setup based on Rinard et al. [154], that digitizes the signal on a digital storage oscilloscope with a $1GHz$ bandwidth (Agilent Technologies MSO7104B, Fig. 5.1 #20). The low noise amplifier (Fig. 5.1 #16) is protected from high power microwave reflections by a limiter (Fig. 5.1 #15) which can tolerate short pulses from a $1kW$ TWT amplifier. The recovery time of the LNA and IQ mixer are short compared to the deadtime of the spectrometer. More details are described in Appendix A.2.4.

In order to manipulate and detect coherent waveforms with a 1° accuracy in the microwave X-band phase, the system needs to consistently synchronize every hardware component that generates or detects any pulsed waveforms so that the timing between the leading edge of any trigger pulses and the crests/nodes of any carrier waves are consistent to within a jitter of $0.3ps$ (see Appendix A.2.1 for phase noise values). An oven-controlled $10MHz$ oscillator (Electronic Research Co. Model 130, Fig. 5.1 #21) generates a clock signal and an amplifier (Stanford Research Systems Model FS735, Fig. 5.1 #22) duplicate and distributes it to the DAC board (High Speed Circuit Consultants, software build 10, Fig. 5.1 #4), digital storage oscilloscope (Agilent Technologies MSO7104B, Fig. 5.1 #20), and YIG-tuned oscillator (MicroLambda MLSL-1178, Fig. 5.1 #2). Each of the three components synchronizes to the $10MHz$ clock signal via a phase-locked-loop (PLL) mechanism.

The components used to construct the spectrometer have various imperfections. Imbalances in the DAC board output levels (see Fig. 5.2) and imbalances in the amplitude and phase characteristics of the transmit IQ mixer (Fig. 5.1 #6) lead to systematic imperfections in the amplitude and phase of the transmitted pulse waveforms, as well as a low-level bleed-through (leakage) of the carrier wave. Similar imbalances in the heterodyne detectors IQ mixer (Fig. 5.1 #18) and amplifiers (Fig. 5.1 #19) can lead to quadrature imbalance or DC offset in the detected signal. Rather than pursuing the task of improving the performance of each relevant hardware component, we simply implement digital calibration routines that correct for these imperfections, a strategy previously implemented by Martinis [164] for experiments on superconducting qubits. Such calibration routines require knowledge of the exact amplitude and phase of the waveform output by the AWG (i.e. output from the transmitting IQ mixer, Fig. 5.1 #6). In order to avoid detector imperfections coming from the mixers, diodes, or amplifiers that constitute the home-built heterodyne detector (Fig. 5.1 #14 - #20), we employ a sampling oscilloscope (Fig. 5.1 #9), which acquires only one sample point per acquisition, but does so accurately, linearly, and with a very high ($20GHz$) detection bandwidth. We stroboscopically reconstruct the amplitude and phase of the transmitting microwave waveform by feeding the sampling scope a phase-coherent (i.e. consistent to within $< 0.3ps$) trigger from the DAC board and an unmodulated reference signal from the microwave carrier. With knowledge of the exact microwave waveform that is transmitted, we can then calibrate for imperfections in the AWG and (by using the transmitted waveform as a known test signal) the detector, as described in Appendix A.2.7. While the output transfer function of the AWG system might not be significant relative to the input transfer function of the resonator (which we correct for with experiments shown in the Results and Discussion section), proper calibration for the transmitter IQ mixers quadrature imbalance can prove crucial to ones ability to properly and easily control the pulse waveforms. This is because such imbalances are non-linear - i.e. they cannot be expressed as a matrix transformation (e.g., a scaled Fourier transform) in the complex waveform space. The Python libraries can automatically include the results of these calibrations when generating output pulse sequences or detecting the free induction decay (FID) and echo signals.

In fact, it is our core strategy that the AWG EPR spectrometer is controlled entirely through in-house Python libraries (see Appendix A.2.5). These allow the user to interact with the spectrometer through simple pulse programming commands that can specify the position of the various delays and timing triggers with a minimal amount of coding. The shape of the pulse waveforms can be specified either numerically or by simply writing out their analytical forms (see Appendix A.2.5). As the Results and Discussion will demonstrate, there also is a distinct benefit to specifying the pulse sequence at an arbitrarily high resolution and allowing the Python library to automatically down-sample the waveform to the $1ns$ resolution of the DAC board (see Appendix A.2.6 for details). Similarly, a single function call allows the user to adjust the acquisition length or sampling time and to acquire signal.

5.3.2 Samples

The experiments presented here employed one of two samples, both of which were loaded into a $3mm$ i.d. $4mm$ o.d. fused quartz EPR tube (Part 3x4, Technical Glass Products, Painesville Twp., OH).

Sample A: Several flakes ($1-5mg$) of a solid BDPA (a,c-Bisdiphenylene-b-phenylallyl) complexed with benzene (1:1) were used without further modification (Product 152560, Sigma Aldrich, St. Louis, MO). Both, the T_1 and T_m relaxation times for this sample are approximately $100\mu s$ [165].

Sample B: Following the procedure used by Maly et al. [165], BDPA was dissolved in toluene and then diluted in a polystyrene matrix to a concentration of $46mmol\ BDPA/kg$ of polystyrene (Product 331651, Sigma Aldrich, St. Louis, MO). The BDPA-polystyrene-toluene paste was then dried by spreading it onto a watch glass. After sitting for $6h$, the sample was dried under vacuum overnight for $12h$. Then, $28mg$ of the powdery, dilute sample was packed into the EPR tube. The T_1 relaxation time, determined by inversion recovery, was $5\mu s$, and the phase memory time, T_m, determined by spin-echo measurements, was $500ns$.

5.4 Results and Discussion

In this section, we characterize the AWG X-band EPR spectrometer and demonstrate the ability to obtain the desired spin response for a given pulse. We first (Section 5.4.1) perform four tests to verify that this digitally calibrated single-channel spectrometer allows one to perform standard EPR experiments: (1) We characterize the phase stability and noise of the instrument. (2) By measuring the fidelity of the pulses amplified by a solid-state amplifier, we judge the spectrometers ability to generate shaped microwave pulses at higher power. (3) Despite the absence of traditional phase-shifter components, we successfully implement standard 16-step (echo sequence) and 4-step (FID sequence) phase cycles to remove experimental artifacts, thus demonstrating precise control over the phase of our digitally calibrated pulses. (4) We perform a standard Tm relaxation measurement to test the interpulse spatial resolution achieved with the DAC board. Finally (Section 5.4.2), by observing the spin response over a range of resonance offsets, we obtain the frequency profile of the pulse waveforms that are seen by the spins. This allows us to correct for the response profile of the spectrometer in order to generate rectangular, Gaussian, and truncated sinc pulses with very high fidelity.

5.4.1 Verification of Spectrometer Performance

To show that the various hardware components remain phase coherent, EPR signal was detected (on **Sample A**) with a varying number of averages, n. With perfect phase coherence, the SNR would scale linearly with $\sqrt{n}$. A $\pi/2$ rectangular pulse of $60ns$ length was repeated n times at a rate of $100kHz$, yielding FIDs that were signal averaged on the oscilloscope and Fourier transformed to yield a spectrum. The SNR was determined from the integrated signal peak divided by the standard deviation of the noise. The SNR was re-determined for values of n ranging from 500 to 29,500 and plotted against

$\sqrt{n}$ as shown in Fig. 5.3. The linear dependence of the SNR on $\sqrt{n}$ shows that the transmitter and receiver systems maintain excellent phase coherence through the course of many signal averages. Thus, the standard oven controlled oscillator that we use for our experiments has the stability necessary to perform standard pulsed EPR experiments for biochemical applications, if necessary over long timescales required to secure sufficient signal to noise.

The absolute SNR reported in Fig. 5.3 is not optimized to the level reported for other home-built or commercial X-band instruments ($SNR = 25$ from 1 scan on $6.3x10^{14}$ total spins in a 1 kGy gamma irradiated quartz sample [166]). However, the reasons for this are well understood. First, we have not yet implemented a switch to close off the pre-amplifier ($20dB$ gain) and solid-state amplifier ($36dB$ gain), which thus presently transmit relatively high power noise to the detector. By adding a switch we expect to reduce the noise power density from the measured value of $4.1x10^{-16}(W/Hz)$ ($-124dBm/Hz$) to approximately the level of thermal noise of the resonator ($4.1x10^{-12}(W/Hz)$, i.e. $-174dBm/Hz$, at $300K$), and thus improve the SNR. The loss from the resonator to the LNA in the detector is approximately 3 dB, which could be optimized. Also, the noise figure of our detection system itself ($10dB$ degradation in the SNR) is much higher than expected ($2.51dB$) from the design previously published in [154], corresponding to another 2.4-fold gain in the $(V_{signal}/V_{rms})SNR$. A systematic diagnosis of the detection system determined that the first amplifier in the receiver train has a noise figure higher than specifications, and work is currently underway to resolve this.

Next, we test the ease and fidelity with which our spectrometer generates a complex pulse sequence at a moderately high output power. We defined waveforms analytically at an arbitrarily high resolution (Appendix A.2.5) to describe a composite pulse ($+x$, x, $+y$, y), a triangular pulse, a Gaussian pulse, a truncated sinc pulse, and an adiabatic rapid passage sech/tanh pulse [161]. The Python libraries automatically calibrate (Appendix

A.2.7) and down-sample the waveforms to $1ns$ resolution to generate suitable instructions for the DAC board (Appendix **??**). The pulse sequence was captured on the sampling oscilloscope with absolute phase information after being amplified to a power of $12-13W$ ($41dBm$). Slight deviations in pulse amplitude and phase (Fig. 5.4) can be seen when exceeding 70% of the maximum output power of the AWG, but are negligible at lower powers. The amplitude and phase offsets are caused by amplifier saturation which, in principle, can be corrected for separately from resonator distortions. We therefore expect that we are not limited by non-linearities present even in higher power amplifiers such as TWTs.

Next we test the ability of this spectrometer to perform standard phase cycling sequences, which are essential for pulsed EPR experiments due to their ability to select signal belonging to particular coherence transfer pathways and their ability to correct for receiver imbalances and other imperfections. Some applications, in particular double quantum coherence (DQC)-based distance measurements [167], demand highly accurate phase cycling capabilities. This is typically achieved by directing the microwave pulse waveform through one of several channels with pre-set phase delays, e.g. requiring 4 channels to cycle between $+x$, x, $+y$ and y phases. However, the spectrometer presented here implements a single channel with fully functional phase cycling that is achieved simply by adjusting the relative scaling in the two AWG quadrature inputs. Though not utilized here, this scheme offers the possibility to exploit arbitrary phase values if needed.

A Hahn echo sequence (Fig. 5.5(a)), with a $60ns$ $\pi/2$-pulse and a $120ns$ π-pulse (τ of $1000ns$), was employed to acquire signal from Sample B at a resonator Q of 1000. In order to isolate the echo signal without cycling the phase of the pulses and receiver, one must acquire an off-resonance “background scan” that is subtracted from an on-resonance signal. We performed such an experiment for comparison. Then, we carried out experiments using a 16-step phase cycle that selects the coherence transfer pathway of the echo (Fig. 5.5(b)) to remove any spurious pulse ring-down signal and DC offset, as well as unwanted residual FID signal, from the second pulse without the need for a background scan. As expected and shown by Fig. 5.5(c), both background subtraction and phase cycling yield clean, identical echo signals, while the SNR of the phase cycled result is approximately twice as large when the same number of total scans are used for both methods. This SNR improvement is expected since half the scans for the background subtraction experiment were acquired off-resonance, resulting in half the signal amplitude.

In the case where we are collecting an FID, phase cycling no longer offers the same advantage in removing the ring-down from the signal. However, it is well known that phase cycling can effectively eliminate instrumental imperfections. For instance, if the two quadrature detection channels are not precisely 90° out of phase with each other or have different sensitivities, a negative frequency mirror peak appears in the Fourier transform of the FID [168]. As shown in Fig. 5.6, when an FID signal is acquired with a 4-step phase cycle, the phase cycling provided by the spectrometer successfully removes the artificial mirror peak that occurs in the Fourier transform of the FID. Along with the previously demonstrated selection of the echo signal, this demonstrates the precision and stability of the mixer-based, digital AWG phase cycling method, which does not require separate pre-set phase delay channels.

Many home-built spectrometers offer a timing resolution significantly better than $1ns$ [144, 157]. Such high timing resolution might be needed in the currently presented spectrometer for select experiments, especially after upgrading the amplifier to a high power TWT. Since the fundamental timing resolution of the AWG presented here is only $1ns$, a concern might arise over how well this spectrometer can control inter-pulse spacing or calibrate the pulse lengths with sufficient precision. However, while the $1ns$ time resolution of the DAC board fundamentally limits the band width of the pulses in frequency space (and therefore limits the sharpness of the edges of the pulses), the pulse lengths and inter-pulse delays can still be defined with a time resolution finer than $1ns$. This can be accomplished by defining the desired waveform at an resolution, such as $10ps$, where the inter-pulse delays and lengths are defined with a resolution that is intentionally higher than that achievable with the DAC board. This high resolution waveform is then convolved with a $1ns$ Gaussian, filtering out frequency components outside the bandwidth of the DAC board, while preserving a high dynamic range that finely defines the pulse amplitude. Then, the pulse is converted to the resolution of the DAC board by reducing the bandwidth in frequency space to $1GHz$ to match the bandwidth of the DAC board.

This "down-sampling" procedure makes use of the large dynamic range of the DAC board to preserve the distance between the centers (or edges) of the pulses with a resolution of better than $250ps$, as Fig. 5.7 experimentally demonstrates.

To conclude this section, we present a proof-of-principle EPR experiment that implements both sub-ns changes in delay times and phase cycling. We employ a phase-cycled Hahn echo pulse sequence (as in Fig. 5.6(ab)) to acquire signal from Sample A at a resonator Q of 500 and $\pi/2$ length of $60ns$. Here, the delay time, τ, between the $\pi/2$ and the π-pulse was varied to carry out measurements of phase decoherence (i.e. measurement of T_m) and signal was acquired with 5000 averages (Fig. 5.8). The best-fit exponential decay determined the T_m relaxation time to be $490 \pm 14ns$. Fig. 5.8 (inset) shows the same measurement at a $250ps$ resolution in τ. This higher resolution data smoothly interpolates between the lower resolution points, closely following the best-fit exponential decay. We thus find that AWG-based systems offer the benefit of observing the spin-echo relaxation decay with nearly unprecedented time resolution. This should allow one to determine subtle features in T_m, such as those coming from multiple overlapping relaxation contributions [165], with high precision and also to resolve short decay times. Although we are limited by the rising and falling edges when generating short pulses, we can specify the length of a pulse to within $250ps$ by our downsampling procedure, in a similar way to finely tuning the delay length. In situations where longer pulses are required, such as matched pulses in ESEEM which have been shown to increase modulation depth by an even order of magnitude in some cases [169], we can provide precise tip angles in the case of constant B_1 amplitude.

5.4.2 Spin Response to Transfer Function Corrected Pulses

The AWG capabilities of the spectrometer presented here allow us to generate any arbitrary pulse shape as part of a coherent pulse sequence. However, the pulse waveform that acts on the spins inside the cavity does not exactly match that leaving the AWG. In previous studies, a pickup coil has been used to monitor the microwave waveform inside the cavity. However, the pickup coil can introduce unknown spatial distortions to the microwaves inside the cavity and also subjects the measured waveform to its own transfer function, which may not be consistent for all setups. Therefore, we instead directly monitor the spin response from a sample with a narrow linewidth, which selects the amplitude of a narrow spectral slice of the excitation profile of the pulse. By sweeping the field, we map out the excitation profile of the pulse as a function of resonance offset. This technique allows us to verify and optimize precise control of the waveform seen by the spins.

The pulse is convolved in the time-domain with an impulse response function that depends on the resonator Q-factor, residual miscalibration of the final AWG output, and additional group delays and imperfections from the transmission lines (to name some of the most obvious sources):

$$y(t) = x(t) * h(t) = \int_{-\infty}^{\infty} h(t-\tau)x(\tau)d\tau \tag{5.1}$$

Here $x(t)$ is the waveform of the programmed pulse, $y(t)$ is the waveform of the pulse inside the resonator, and $h(t)$ is the impulse response function. In the frequency domain, the convolution above is equivalent to a multiplication, i.e.:

$$Y(\nu) = X(\nu)H(\nu) \tag{5.2}$$

where the functions $Y(\nu)$, $X(\nu)$, and $H(\nu)$, are Fourier transforms of $y(t)$, $x(t)$, and $h(t)$, respectively. We directly obtain the experimental excitation profile, $Y(\nu)$, by reading out the spin response in the linear response (i.e. small tip angle) limit. We can then determine the frequency-domain transfer function, $H(\nu)$, of the spectrometer system as Eq. **??**

$$H(\nu) = \frac{Y(\nu)}{X(\nu)} \tag{5.3}$$

We can then define a corrected pulse, $x'(t)$, whose Fourier transform is $X'(\nu)$,

$$X'(\nu) = \frac{X(\nu)}{H(\nu)} \tag{5.4}$$

which experimentally yields the frequency response of the desired waveform, i.e. $Y'(\nu) = X(\nu)$, where $Y'(\nu)$ is the frequency profile seen by the spins:

$$Y'(\nu) = H(\nu)X'(\nu) = X(\nu) \tag{5.5}$$

Thus, when the AWG generates the corrected pulse, $x'(t)$, the waveform inside the cavity, $y'(t) = \mathscr{F}^{-1}(Y'(\nu))$, will now match the target waveform, $x(t)$. Thus, by determining and correcting for the transfer function, $H(\nu)$, one can arbitrarily control the waveform, $x(t) = y'(t)$, seen by the spins inside the resonator. Note that the transfer function, as defined above, would also include distortions due to frequency-dependent detection sensitivity, therefore, for greater accuracy, we could include the detector frequency response.

As a proof of concept, we seek to show that this spectrometer can arbitrarily tailor the excitation profiles of pulses over a $60 MHz$ bandwidth. To start with, the transfer function of the spectrometer system must be determined over a broad bandwidth relative to the corrected pulses. Therefore, the excitation profile of a short $10ns$ rectangular test pulse (10° tip angle) was determined (Fig. 5.9(a)). The magnetic field was swept over a range of $\pm 35G$ (with $1G$ resolution) around the resonant magnetic field, while the FID of a BDPA sample ($FWHM = 1.4G$) was recorded. The FID was Fourier transformed, and the integrated signal amplitude ($60MHz$ integration width) was plotted against the resonance offset (converted from field using $g = 2.00$). To calculate the transfer function, $H(\nu)$, we divide the experimental excitation profile, $Y(\nu)$, by the Fourier transform of the pulse, $X(\nu)$ (Eq. (5.3)). Because the Fourier transform of the $10ns$ rectangular test pulse first crosses zero only at $\pm 100MHz$, the excitation profile of the test pulse presents significant signal amplitude over the $60MHz$ bandwidth of this experiment. Therefore, we can accurately determine the transfer function over the bandwidth of this experiment. To verify that the transfer function is independent of the pulse shape, we repeated this procedure with a $50ns$ truncated sinc pulse as the test pulse (Fig. 5.9(b)). As expected, the resulting transfer function was in reasonable agreement with that from the $10ns$ rectangular test pulse.

We applied the transfer function to correct three different pulse waveforms rectangular, Gaussian, and truncated sinc in order to verify a subsequently increased control over the spin system. The rectangular pulse was $100ns$ long. The sinc pulse with the same maximum power was truncated after the 2^{nd} side lobe and was adjusted to a length of $250ns$ so that it yielded similar signal amplitude. The Gaussian pulse was $250ns$ long with a $FWHM$ of $88ns$ and also featured the same peak power and signal amplitude.

The excitation profiles were mapped out with sample A as shown before, except the magnetic field was swept over a narrower range of $\pm 12G$ in steps of $0.25G$. When not performing the transfer function correction, the $24MHz$ bandwidth of the resonator ($Q = 400$) attenuates the side features of the excitation profile (Fig. 5.10). This is especially apparent for the rectangular (a) and sinc pulses (c). As expected, once we apply the transfer function correction (df), the detected excitation profile matches the Fourier transform of the desired pulse with very high fidelity (Fig. 5.10).

The transfer function corrected excitation profiles shown in Fig. 5.10 were obtained by defining an absolute value transfer function and contain no phase information. If instead, we define a complex transfer function, we can correct both the real and imaginary parts of the excitation profile corresponding to the X and Y components of magnetization in the rotating frame. A square $100ns$ pulse was sent to the microwave resonator, which was overcoupled to a Q of 500. As indicated by the excitation profile Fig. 5.11(b), the pulse is significantly distorted by the bandwidth of the resonator and by imperfections in the various transmission line components (i.e. waveguides, circulator, etc.). After the complex transfer function correction, the corrected pulse is significantly different from the original square pulse Fig. 5.11(c). The transfer function correction makes the pulse more broadband, thus introducing new frequency components that cause oscillations in the waveform of the pulse. These oscillations also indicate that the transfer function of the resonator is not as intuitive as the Lorentzian-shaped response function that is predicted by an RLC circuit-like model. Additionally, the small amplitude peaks at the beginning and end of the pulse can be accounted for by noting that they help compensate for the finite rise and fall time inherent to the resonator, i.e. these peaks force the resonator to charge and de-charge, respectively. Once the complex transfer function is applied to the original pulse, both the real and imaginary parts of the excitation profile are significantly improved. Remarkably, despite being initially highly attenuated, after correction, the off-resonance features are scaled properly, as given by Fig. 5.11(d), where they closely match the target excitation profile ($100ns$ square pulse).

Thus, to support our claim of coherent control over a spin system, we have demonstrated control over the phase of the excitation profile. In other words, The DAC board-centered spectrometer can generate arbitrary pulse sequences phase coherently. Coherent excitation is necessary not only for proper phase cycling, but is also a prerequisite for transferring polarization through multiple quantum coherence states. Both of these are fundamental for performing double quantum coherence distance measurements, which with arbitrarily shaped pulse sequences can be done in an optimized manner or for any other pulse sequence that relies on coherence transfer. It should be noted that although we have obtained good agreement between the target and experimental excitation profiles, these experiments were done with relatively long pulse lengths and narrow bandwidth samples, where the experimental opportunities should be fully explored by transitioning to high-power amplifiers.

5.5 Conclusion

With this work, we demonstrate precise control over the spin system in standard pulsed EPR experiments achieved with an X-band AWG EPR spectrometer, entirely home-built around a DAC platform as the main control unit. In particular, we precisely shape the offset-dependent response of the spins to follow a variety of different excitation profiles. The spectrometer presented here thus overcomes the limitations of rectangular pulses by enabling truly arbitrary waveform capabilities for pulsed EPR. At the same time, it represents an alternative approach to spectrometer design. Arbitrary control over the phase and amplitude of the pulses, as well as the timing of all spectrometer components are combined into one digital control unit. This provides the technical capability for generating precisely controlled and optimized coherent pulse sequences, dramatically decreasing the complexity of the instrument and allowing for a detailed level of control and ability to further optimize the instrument. A Python-based interface easily masks the complexity such instrumentation might otherwise introduce, by allowing the user to program the instrument as though controlling a standard pulse sequence with an arbitrarily high resolution and permitting the user to specify pulses inline using analytical descriptions of the relevant functions. Down-sampling to the intrinsic DAC bandwidth and various calibrations are handled automatically and "behind the scenes" within the Python-based interface. Thus, we believe this control system offers significant advantages over what is currently available as state-of-the-art platforms for pulsed EPR spectrometers.

Similar to other recent work [144, 145, 163], we find that a design based on mixing a shaped intermediate frequency wave with a higher frequency carrier proves to be extremely versatile and practical. In particular, we note that the carrier frequency can be changed without the need to recalculate the entire waveform. This setup could also be directly adapted to several other frequency bands, including K-band ($18-26.5GHz$) and Q-band ($33-50GHz$), simply by replacing the X-band-specific components (the micro wave source, mixer, and the microwave resonator and bridge components). The only limitation for applying the same AWG technology to much higher frequencies is that the intrinsic $1GHz$ bandwidth would no longer cover the bandwidth of the resonator; however commercial DAC boards that operate at higher bandwidths are already available [144, 170], and, with more effort, the design of the present DAC board could be scaled to a faster sampling rate and subsequently higher bandwidth. Furthermore, even in wideband EPR spectrometers without resonators or with low-Q resonators, where power becomes the main factor limiting excitation bandwidth, experiments should substantially benefit from the enhancement in excitation bandwidth provided by arbitrarily shaped pulses.

This work contains similar developments to those by Spindler et al. [145, 146] and Doll et al. [144] that have implemented add-on AWG units to pre-existing X-band EPR spectrometers, and have developed techniques to correct for the response of the resonator as well as the non-linear response of the TWT amplifier. In this study, we have investigated the fidelity of the excitation profiles of arbitrarily shaped pulses. As more advanced AWG EPR experiments are developed, the precision of the arbitrary pulses will be come increasingly important and a necessary consideration in generating multiple quantum coherence pulse sequences.

Further improvements can capitalize on the advances presented here. Optimization procedures and on-the-fly feedback techniques can be implemented in this design to improve the excitation profiles. This work was performed on narrow bandwidth samples at relatively low microwave powers. Thus, integrating a high-power TWT into this setup is required before AWG capabilities are demonstrated to become truly advantageous over standard EPR techniques. A high-power TWT would allow one to implement the same level of high-fidelity control, while exciting spins over a significantly larger bandwidth. By allowing one to excite significant signal amplitudes from fast-relaxing samples, it would also allow one to take advantage of the $250ps$ resolution in pulse length and delay timing to acquire highly resolved relaxation measurements. This would be of great and direct benefit to characterize fast relaxing samples (i.e. samples with a short T_m or T_1), such as found with many nitroxide labels or transition metal probes under ambient conditions, and are relevant for many biological applications. At high power, one should be able to implement very similar methodologies to those presented here. The shape of the waveforms seen by the spins can still be directly mapped out in the linear response regime to verify reproduction of the exact waveform desired. Then (with appropriate correction for any amplifier nonlinearities), the power could be scaled up into the regime of nonlinear spin response to generate a variety of interesting effects [171]. In fact, the sampling-scope detection scheme presented here should allow one to measure and thus correct for a significant portion of the nonlinear distortions generated at high powers, near the saturation point of the TWT, thus easily allowing for the types of nonlinear corrections that have been implemented by Spindler et al. and Doll et al. [146, 144]. Therefore while offering flexibility, control, and ease of use at X-band, it is of significant value that this spectrometer platform design can successfully shape the excitation profiles of the spins in fact matching the theoretical profiles with fidelity beyond our expectations, and thus promising significant improvements for a variety of EPR measurement techniques.

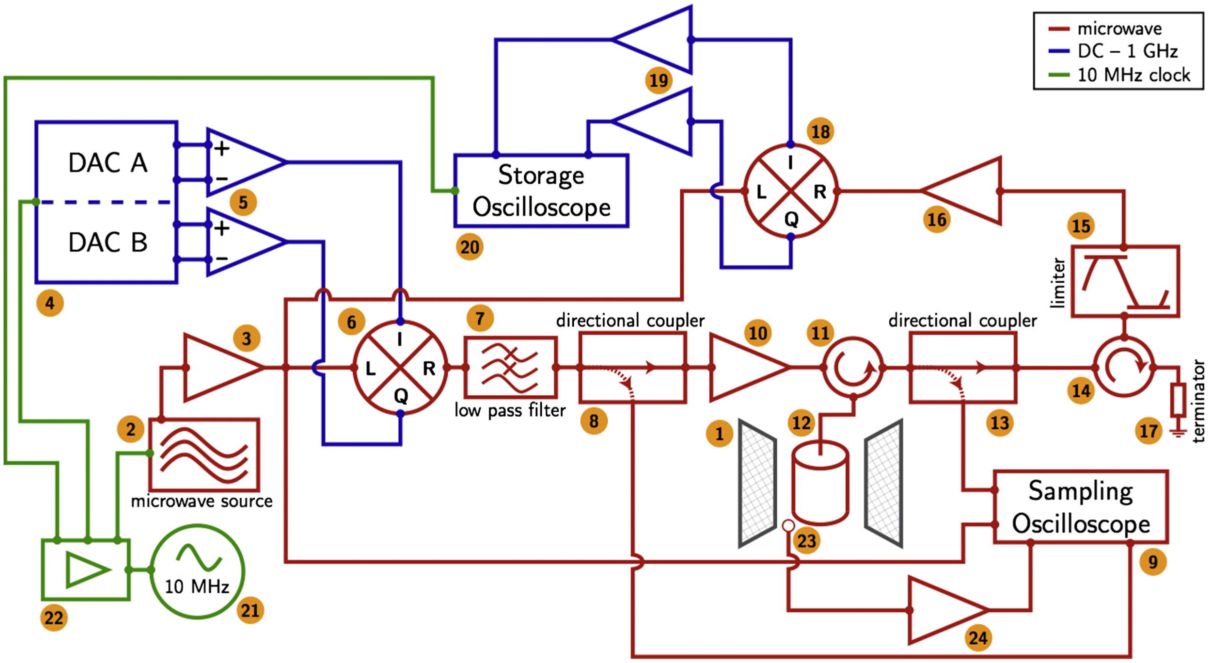

Figure 5.1: Schematic overview of the pulsed AWG X-band EPR spectrometer. X-band microwave paths, indicated in red, transmit the pulse waveforms and carry the returning signal via coaxial cables, except for components #11, #13, #14, and #17, which are X-band waveguide components. The microwave carrier is generated (#2) and amplified (#3) and then mixed (#6) with two digitally controlled, quadrature $1GHz$ transmit waveforms that are generated by the DAC board (#4) and amplified by two differential amplifiers (#5) to generate shaped X-band pulses at $10dBm$. The output waveform is filtered (#7), amplified to $43dBm$ (#10), and sent to the resonator (#12). The returning signal is power-limited (#15), and amplified (#16), before being sent to a heterodyne detector comprising an IQ mixer (#18) that generates two quadrature $1GHz$ intermediate frequency (IF) waveforms, which are amplified (#19) and detected by the storage oscilloscope (#20). DC to $1GHz$ signal paths are shown in blue and are present in both the AWG unit and the heterodyne detector. The reference oscillator (#21) is connected to a distribution amplifier (#22) and supplies a $10MHz$ signal, shown in green, which synchronizes the microwave source, DAC board, and detector. Appendix A.2.1 describes the various labeled components in detail.

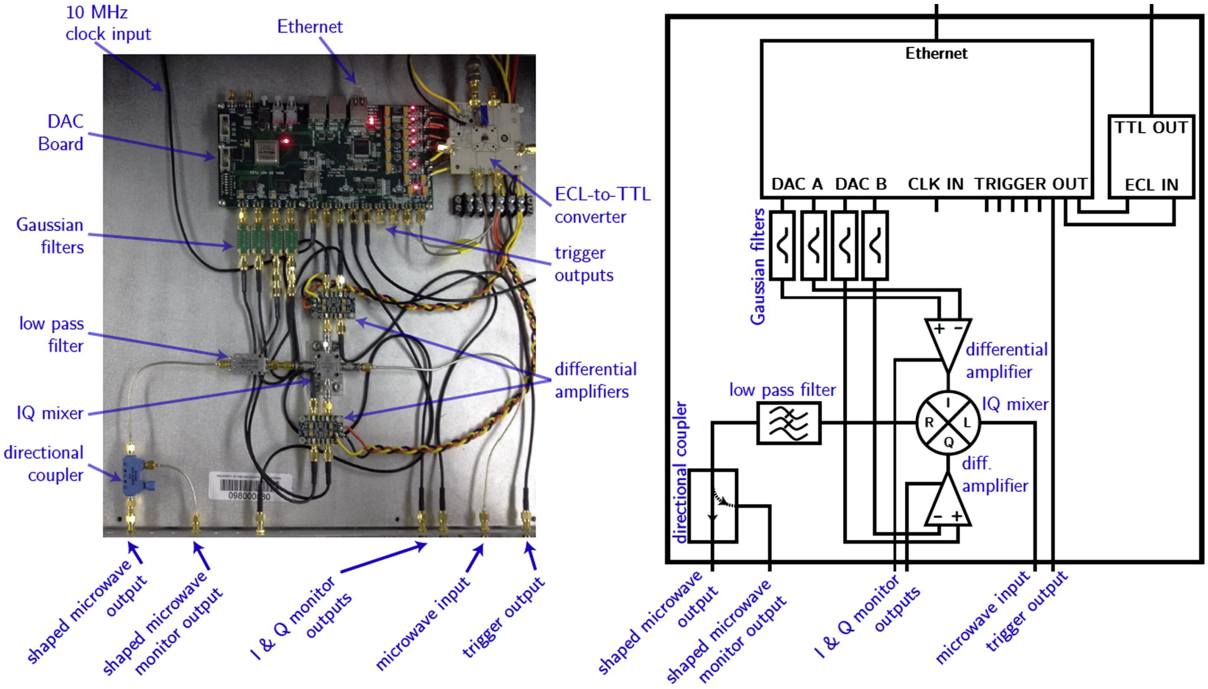

Figure 5.2: Photograph and schematic of the arbitrary waveform generation (AWG) unit. The figure shows the 1 GHz digital-to-analog converter (DAC) board and the associated components used to modulate the shaped X-band waveform and to deliver a TTL timing trigger to the detector. Details are discussed further in Appendix A.2.2.

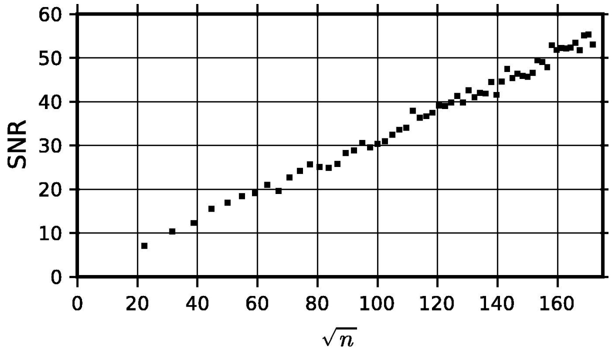

Figure 5.3: Signal coherence test. SNR, calculated as explained in the text, as a function of $\sqrt{n}$, where n is the number of scans that are averaged.

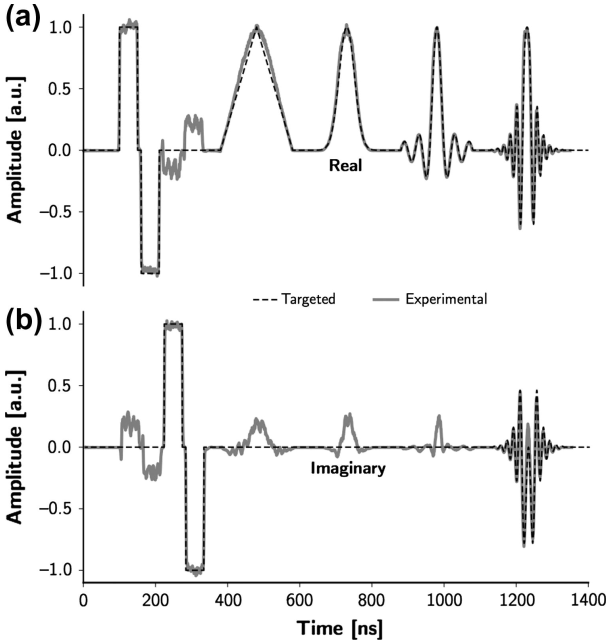

Figure 5.4: Captured pulse sequence with multiple shaped pulses. Real (a) and imaginary (b) components of a targeted waveform (black dashed lines) are compared to the microwave waveform captured on the sampling oscilloscope (gray, solid lines) following the procedures described in Appendices A.2.6, A.2.7. The target waveform consists of a sequence of composite pulses, a triangular pulse, a Gaussian pulse, a truncated sinc pulse, and a sech/tanh adiabatic rapid passage (left to right, respectively).

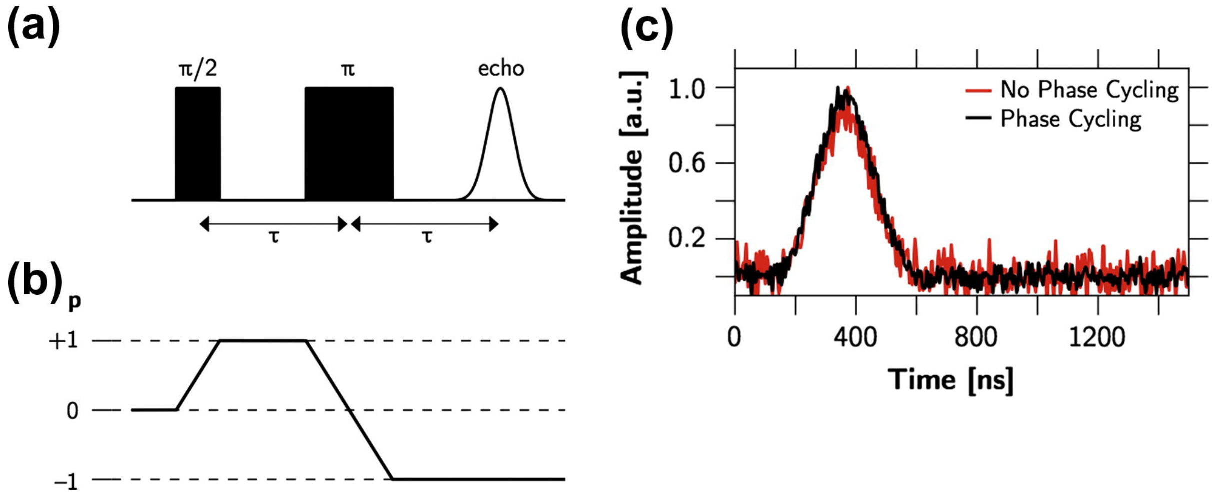

Figure 5.5: Hahn echo measurement verifies functionality of AWG-based phase cycling. Hahn echo pulse sequence (a) and respective coherence transfer pathway (b), as well as comparison of the signal (c) retrieved with off-resonance background subtraction (red) vs. a 16-step phase cycle (black) appropriate for the coherence pathway shown in (b). A $400MHz$ digital band-pass filter was applied to the signal shown in (c). The SNR (integrated echo intensity vs. $RMSD$ of the noise) is 9.6 for off-resonance background subtraction and 18.4 for phase cycling.

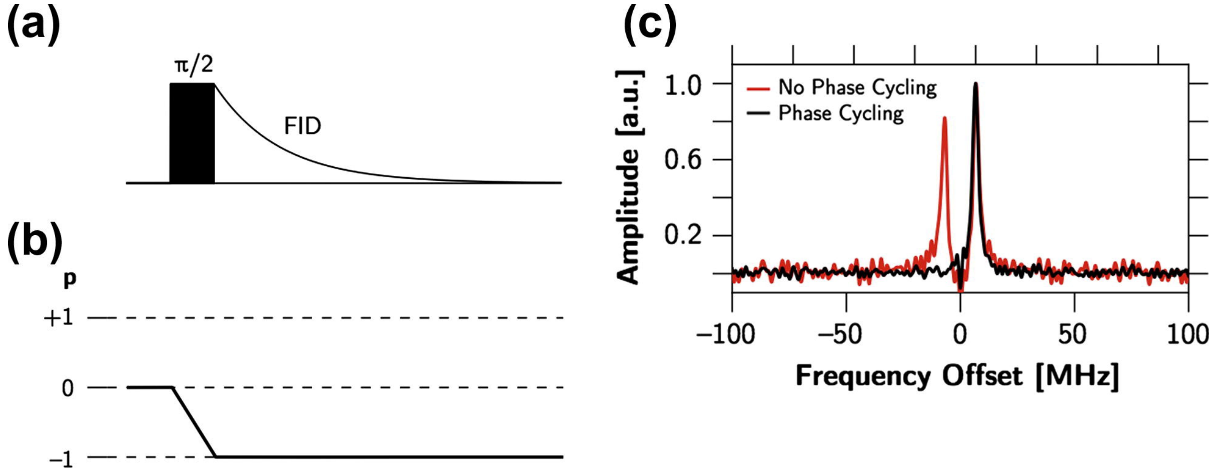

Figure 5.6: FID measurement verifies functionality of AWG-based phase cycling through removal of receiver imbalance artifacts. FID pulse sequence (a) and coherence transfer pathway (b). Fourier-transform of FID with magnetic field set 2.4 G off-resonance (c). The negative frequency peak due to receiver imbalances is successfully eliminated with a digitally calibrated, mixer-based phase cycle.

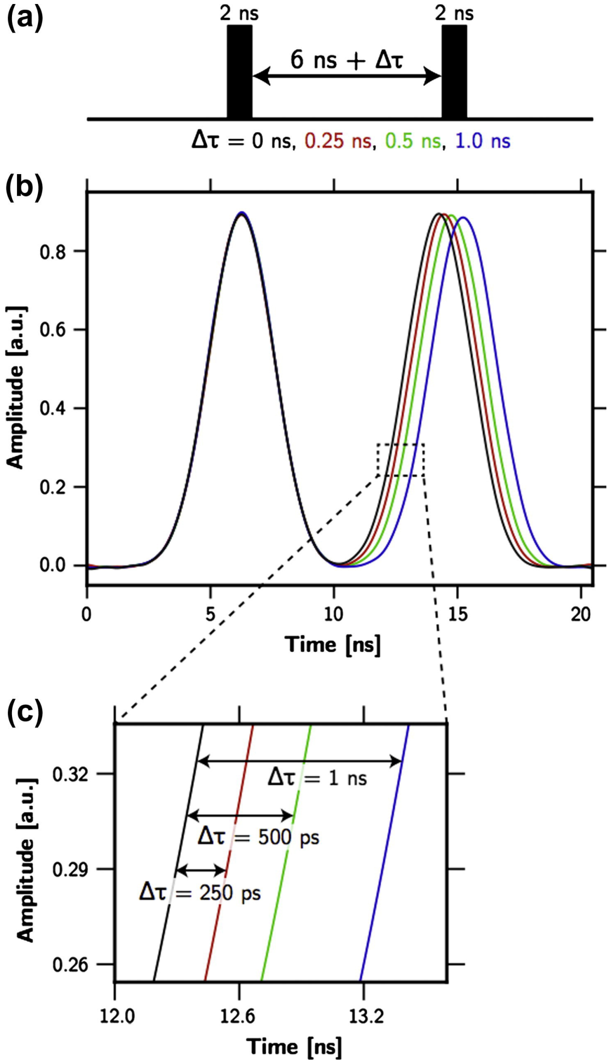

Figure 5.7: Pulse sequence showing delays that are defined with $\leq 250ps$ time resolution. The pulse sequence (a) consists of two $2ns$ wide pulses with a varying inter-pulse delay of $6ns$, $6.25ns$, $6.5ns$, and $7ns$ and generates a microwave waveform (b) that is captured on the sampling oscilloscope and digitally filtered with a $1GHz$ bandpass. As the higher resolution inset (c) shows, delays with $\leq 250ps$ resolution are generated with high fidelity.

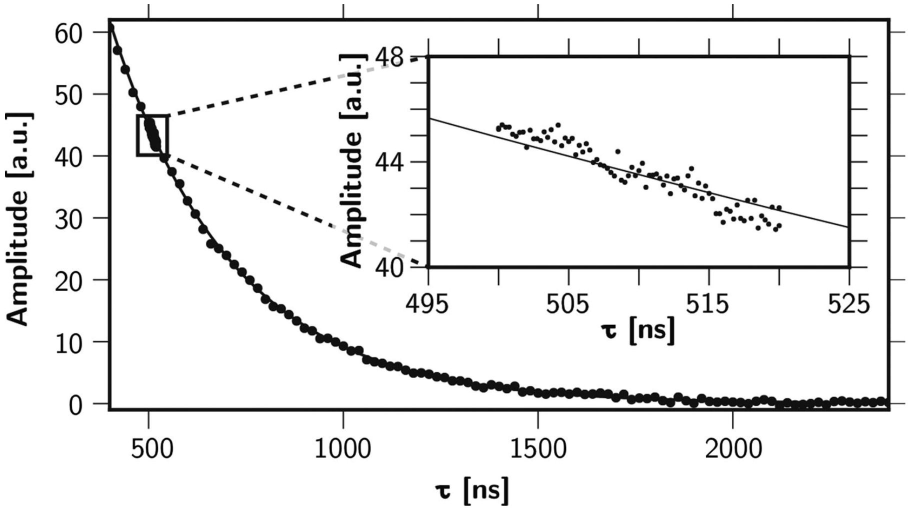

Figure 5.8: T_m relaxation curve with $250ps$ step size. This figure presents a Tm relaxation curve recorded from a Hahn echo sequence on Sample B. A $12MHz$ digital bandpass filter was applied to the data and the echo area was integrated and plotted against the delay time, τ, between the pulses, which was varied in $34ns$ steps. The solid black line (in both the main plot and inset) gives the exponential fit of this data, with $T_m = 490 \pm 14ns$. The inset shows the same measurement, acquired with higher time resolution; for this data, a $250ps$ step size was used for the pulse delay.

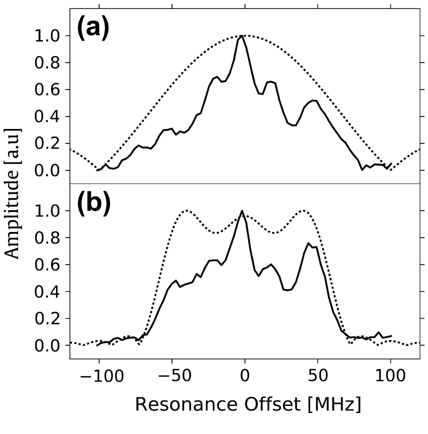

Figure 5.9: Spin response to broadband pulses. The spin response from (a) $10ns$ square and (b) $50ns$ truncated sinc pulses used to calculate the resonator transfer function. The solid lines illustrate the experimental excitation profiles and the dashed lines illustrate the Fourier transform of the output pulse waveforms. The transfer functions calculated from the ratio of the experimental excitation profile and Fourier of the pulse waveform for (a) and (b) are in good agreement.

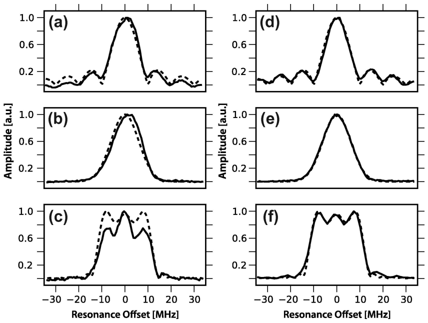

Figure 5.10: Spin excitation profiles resulting from shaped pulses. Normalized spin excitation profiles (solid lines) generated by a rectangular (a), Gaussian (b), and truncated sinc (c) pulses, acquired as described in the text. The analogous transfer function corrected pulses for (ac) are shown in (df), respectively. The dashed lines show the Fourier transforms of the excitation pulses as generated by the AWG, which represent the excitation profiles of the pulses predicted by the small tip angle approximation (which is valid for these measurements), whereas the solid lines show the experimentally measured excitation profile of the spins as a function of resonance offset.

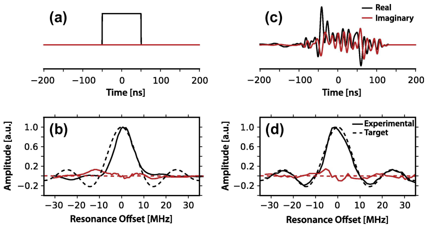

Figure 5.11: Phase sensitive transfer function correction for square pulse. Black and red lines represent real and imaginary part, respectively. For excitation profiles, solid and dashed lines represent experimental and target excitation profiles, respectively. (a) Time-domain $100ns$ square pulse. (b) Spin response to $100ns$ square pulse. (c) Complex transfer function corrected pulse. (d) Spin response to complex transfer function corrected pulse. As before, excitation profiles were collected using pulses in the linear response (i.e., small tip angle) regime.

Chapter 6

Active Cancellation for Zero Dead-Time Pulse EPR

6.1 Abstract

The necessary resonator employed in pulse electron paramagnetic resonance (EPR) rings after the excitation pulse and creates a finite detector dead-time that ultimately prevents the detection of signal from fast relaxing spin systems, hindering the application of pulse EPR to room temperature measurements of interesting chemical or biological systems. We employ a recently available high bandwidth arbitrary waveform generator (AWG) to produce a cancellation pulse that precisely destructively interferes with the resonant cavity ring-down. We find that we can faithfully detect EPR signal at all times immediately after, as well as during, the excitation pulse. This is a proof of concept study showcasing the capability of AWG pulses to precisely cancel out the resonator ring-down, and allow for the detection of EPR signal during the pulse itself, as well as the dead-time of the resonator. However, the applicability of this approach to conventional EPR experiments is not immediate, as it hinges on either (1) the availability of low-

noise microwave sources and amplifiers to produce the necessary power for pulse EPR experiment or (2) the availability of very high conversion factor micro coil resonators that allow for pulse EPR experiments at modest microwave power.

6.2 Introduction

In recent years pulse electron paramagnetic resonance (EPR) has seen many advances in its ability to study paramagnetic or spin labelled chemical and biological systems of interest due to substantial improvements in instrumentation and measurement methods [172, 147, 45, 173, 174, 146, 175] and the necessary theory for quantitative interpretation of data [126, 176, 177, 178]. However in the most common applications of pulse EPR at $10 - 35GHz$ frequency, the necessary high power microwave pulse, required to excite the magnetic resonance of the electron spin system, induces a ring-down during which the pulse energy dissipates from the resonant microwave cavity. The cavity ring-down causes a finite detector dead time after the microwave pulse that can last up to $200ns$ at cavity quality factors common for pulsed EPR measurements, preventing the detection of EPR signals that rapidly decay during this time. This not only limits the prospects for Fourier transform pulse EPR but, more immediately, prevents the detection of fast decaying signals of interest, such as the T_2 of spin labelled proteins in the hydrated powder state used for evaluating the protein dynamic transition [45, 179] as in chapter **??**. Many have explored ideas to suppress the resonator ringing in magnetic resonance studies; by means of damped circuit designs [180, 181, 182], use of orthogonal excitation and detection coils [183, 184, 185, 186], by induction mode detection [187], or by use of a suppression pulse to de-charge the resonant circuit from the excitation pulse [163, 188]. One of the most common solutions to ring-down at X-band frequencies is to decrease the effective Q-factor of the microwave resonant cavity (e.g., by over-coupling) to minimize the ring-down, to as little as $10 - 200ns$ in the best case scenario [189, 190], however reduction of the Q-factor also significantly decreases the B_1 conversion factor so one must use very high rf pulse power (1 kW) to generate sufficient B_1 field strength and compensate for the loss. Even so, a dead-time of $10 - 200$ ns is too long to fully capture the timescales and signatures of rapidly decaying signal of many electron spin systems of interest.

Expanding on previous ideas [191, 192] we completely remove the resonator ring-down and detect signal at all times during or after a pulse by means of a previously unavailable high bandwidth Arbitrary Waveform Generator (AWG) that synthesizes a separate “cancellation pulse”. We capitalize on the fact that the resonator ring-down depends only on the electronic properties of the resonator. Therefore, once the ring-down is accurately measured for given experimental conditions, a modern AWG can faithfully produce a cancellation pulse to precisely and destructively interfere with this ring down, thus unveiling the initially buried EPR signal. We refer to this procedure as “active cancellation” of the resonator ring-down.

6.3 Experimental

The accurate cancellation of the resonator ring-down immediately following, and even during the microwave excitation pulse, is enabled by a home-built pulse EPR instrument that features AWG capabilities at $1GHz$ bandwidth and $14 - bit$ dynamic range [193], similar to recent developments by others [172, 163, 144, 194, 145, 170]. To realize the full capabilities of the field programmable gate array (FPGA) core of the AWG, originally produced by Bialczak and Martinis et al. [164], we developed a pulse EPR instrument that is entirely coordinated and synchronized by the FPGA [193]. The benefit of centralizing the complete EPR instrument on the FPGA core is the overwhelming simplification of the instrument operation [170, 195], a fully phase-locked instrument, and the capability for precise calibration of microwave amplitude, phase, and timing, included as an intrinsic feature of the spectrometer. In fact achieving precise destructive interference of the complex resonator ring-down at the detector is only possible with a phase-locked AWG, microwave source, and detection oscilloscope. To calculate a cancellation pulse we determine the shape and phase of the excitation pulses ring-down with the magnetic field set off resonance to prevent the unwanted detection of induced electron spin signal. Precise destructive interference at the signal detector will occur if the shape and phase of the cancellation pulse are achieved at the signal detector. We account for the distortions that occur to the cancellation pulse en-route to the signal detector by applying a transfer-function, this allows us to calculate the necessary pulse shape to be synthesized to achieve the desired cancellation pulse shape at the signal detector, with more precise details given in the SI (Fig. A.8).

In order to detect true EPR signal at any time during or after the excitation pulse, the AWG-generated cancellation pulse must reach the detector without perturbing the spin system dynamics during the time in which we record signal. We avoid the need for two separate pulse sources one for the excitation pulse, and one for the cancellation pulse that destructively interferes with the resonator ring-down by implementing a waveguide assembly (Fig. 6.1A) that splits a given microwave pulse in two, sending one half of the microwave pulse directly to the detector (Fig. 6.1B “shortcut pathway”) and the other half of the pulse through a delay line leading to the microwave resonator and finally to the detector (Fig. 6.1B “resonator pathway”). Ultimately both waveforms show up at the detector; the leading of the two waveforms coming from the shortcut pathway and the trailing coming from the resonator pathway, (Fig. 6.1B “waveform at detector)”. Here the leading edge of the waveform from the resonator pathway is delayed relative to the waveform from the shortcut pathway by approximately $35ns$, due to the length of the delay line (roughly $1.1m$) inserted before the microwave resonator. This $35ns$ delay between the waveforms, shown in Fig. 6.1B and C as vertical red dashed lines, from the two separate pathways "buys" a $35ns$ window of time to cancel the excitation pulses ring down and detect signal, after which time the cancellation pulse enters the resonator and perturbs the spin response to the excitation pulse. We place a $35ns$ long cancellation pulse behind the excitation pulse after a set delay (Fig. 6.1C "synthesized waveform"). The cancellation pulse is designed to destructively interfere with the specific portion of the resonator ring-down that overlaps with the cancellation pulse at the signal detector. We calculate the cancellation pulse by detecting the resonator ring-down, picking a section of the ring-down to cancel (Fig. 6.1B "waveform at detector" blue dashed line), and taking the negative of that section of the ring-down to form the cancellation pulse (Fig. 6.1C "synthesized waveform" circled in red). Upon synthesizing the waveform in Fig. 6.1, the cancellation pulse follows the excitation pulse, and passes through both the resonator and shortcut pathways (the cancellation pulse is circled in red in both pathways in Fig. 6.1C). The timing and sequence of the waveforms are designed such that after passing through both the resonator and shortcut pathways, the cancellation pulse from the shortcut pathway precisely overlaps with and destructively interferes with the select section of the resonator ring-down at the detector, resulting in the "cancellation window" highlighted by the vertical red dashed lines in Fig. 6.1C "waveform at detector". The cumulative effect of the cancellation pulse from each pathway is shown in the respective colors in Fig. 6.1C "waveform at detector". Once the cancellation window is achieved, it is possible to detect electron spin resonance signal from the interaction between the excitation pulse and the spins of the sample alone within the cancellation window. After the $35ns$ long cancellation window, defined by the length of the delay line, the cancellation pulse enters the resonator and perturbs the spin response from the excitation pulse (Fig. 6.1C "resonator pathway" highlighted in the red circle). We discard the last $5ns$ of the signal detected inside of the cancellation window to prevent any erroneous signal due to the cancellation pulse.

The current implementation of the delay line and cancellation window is strictly to demonstrate the effectiveness of active cancellation of EPR resonator ring down with AWG capabilities using currently available hardware at hand. In reality, the $35ns$ long cancellation window, in which we detect signal, presents a severe limitation to the method as this dramatically extends the experiment to prohibitively long times. One work-around is to increase the length of the delay line, thus increasing the length of the cancellation window. However a simpler solution includes a separate AWG source aimed directly at the signal detector. In this scheme the cancellation pulse only travels to the signal detector, and not the spin-system, allowing one to design the cancellation pulse to destructively interfere with the entirety of the ring-down, such that the entirety of signal could be captured in one shot. Thus, once the high fidelity of AWG pulses for active cancellation can be demonstrated and the merit of the general approach found, alternative and more sustainable hardware solutions will be developed.

Due to the relatively high power of the excitation pulses resonator reflection, up to $10W$, we implement a two-stage optimization procedure to initially calculate a cancellation pulse and further optimize the cancellation pulse such that the EPR signal is uncovered and detectable within the cancellation window. In the first stage we attenuate the excitation pulses high-power ring down to approximately 1 mW and detect the attenuated excitation pulse resonator reflection on a sampling oscilloscope (Tektronix 11801C) (Fig. 6.2B). We select a $35ns$ long portion of the ring-down to cancel and take the cancellation pulse as the negative of this portion of the ring-down (Fig. 6.2C). We apply the transfer-function to the cancellation pulse in order to preemptively account for the systematic distortions that occur to the cancellation pulse in the shortcut pathway en route to the detector. We place the transfer-function corrected cancellation pulse in the original digital excitation waveform (Fig. 6.2D) and synthesize the new waveform. Timing is crucial, so that the cancellation pulse is placed at a precisely tuned time after the excitation pulse in series, such that when the cancellation pulse exits the shortcut pathway it is properly aligned with the (delayed) portion of the excitation pulses resonator ring down that the cancellation pulse was designed to destroy. The fidelity of the cancellation pulse is evaluated by capturing the residual microwave waveform remaining inside of the cancellation window (Fig. 6.2E). If the power of the residual microwave waveform inside of the cancellation window is above a $2.5\mu W$ threshold (saturation limit of the signal detector) we improve the cancellation pulse shape using the residual waveform in (Fig. 6.2E) to calculate a new cancellation pulse. We then apply the transfer-function to the new cancellation pulse and add the transfer-function corrected cancellation pulse to the previous cancellation pulse. We iterate this process of additively improving the cancellation pulse until the residual microwave waveform inside of the cancellation window is below $2.5\mu W$ (usually $2-3$ iterations). At this point, we proceed to the second stage where we detect the residual microwave waveform inside of the cancellation window with the heterodyne detection train of the spectrometer configured to detect the low power EPR signal on a storage oscilloscope (Agilent MSO7104B). By detecting the un-attenuated residual microwave waveform in the cancellation window, we are able to increase the dynamic range for the amplitude resolution, and with such refinement are able to further reduce the residual microwave waveform to $10nW$ (the noise floor of the solid-state amplifier) after employing the same additive cancellation scheme described in stage 1. After these refinement steps, we are able to linearly detect the EPR signal within the cancellation window after background subtraction.

The model system of choice to demonstrate the active cancellation scheme is BDPA (a,c-Bisdiphenylene-b-phenylallyl) embedded in a polystyrene matrix (45mmol BDPA/kg PS referred to as BDPA/PS) that presents relaxation times of $T_2 = 300ns$ and $T_1 = 5\mu s$

[193, 165]. To demonstrate the fidelity of the active cancellation method, a near-critically-coupled ($Q = 900$) Bruker MD5 probe head was used to cause a long detector dead-time of $500 - 600ns$ and a B_1 field of approximately $6MHz$ at $10W$ of pulse power. A $20W$ solid-state amplifier array was employed (4 Advanced Microwave PA2803-24 amplifiers arranged in parallel [52]). Due to the power splitting resulting from the delay line assembly, $10W$ pulses are achieved in both the shortcut pathway and the delay line/resonator pathway.

6.4 Results and Discussion

The two-stage active cancellation procedure reduces the excitation pulses cavity reflection from at most $10W$ to $< 10nW$ (noise level of the $20W$ pulse amplifier), which amounts to $90dB$ attenuation in total. In an effort to demonstrate that the active cancellation method can be employed as a practical scheme to recover unperturbed EPR signal in the presence of high power microwaves, we detect the Rabi oscillation of the spin system at room temperature during a $400ns$ long hard pulse that generates excitation as well as four subsequent inversions of the spin system (Fig. 6.3).

To detect signal during the pulse itself using the active cancellation method (signal persists for $500ns$), it is necessary to compile the signal detected in individual cancellation windows ($35ns$ long) which overlap in time on the trailing edge by $5ns$ and span the entire $500ns$ time range to capture the signal. Recall the need to detect signal in the $35ns$ long cancellation window to ensure the signal detected is due to the influence of the excitation pulse alone, and not by the tandem cancellation pulse interacting with the spins. The EPR signal is detected in each cancellation window by off-resonance background subtraction. By stitching the signal detected from each cancellation window together, we were able to recover the Rabi oscillation of the spins during, as well as after the $400ns$ long excitation pulse of the BDPA/PS sample (Fig. 6.3). We observe that the Rabi oscillation precesses about the axis of excitation with a B_1 field strength of approximately $5MHz$ (with 90°, 180°, and 270° times of 50, 95, and $140ns$ respectively).

For comparison, the Rabi oscillation of the spin system was also measured via Hahn echoes positioned after the decay of the ring-down, where the integrated amplitude of each echo is recorded as a function of increasing length of both the 90° and the 180° pulses (Fig. 6.3). We observe 90°, 180°, and 270° times of 45, 85, and $125ns$ respectively, yielding a B_1 field strength of approximately $6MHz$. When comparing the two methods of measuring the Rabi oscillations, an initial lag period in the nutation frequency is observed in the active cancellation-detected Rabi oscillation, noted in the slightly longer 90° and 180° times. This difference is due to the finite build up time for the excitation pulses B_1 field to reach full amplitude. By comparing the spacing of the 180° and 270° times to the 90° time during the pulse in the active cancellation method, we see this build up time to be $15ns$. Once the B_1 field of the pulse inside of the cavity has built up to maximum strength, the spins then nutate at the expected frequency of $6MHz$ for the given cavity conditions and pulse power.

The key motivation for uncovering the hidden signal under the cavity ring-down, $10--200ns$ long (depending on the size and dielectric constant of the sample and given resonator conditions) under typical pulsed EPR operations, is to access spin systems with prohibitively short relaxation times. While the measurement of fast decaying T_2 spin systems is not currently possible with our low power implementation we seek to demonstrate that our active cancellation strategy can faithfully uncover signal hidden in the ring-down. We perform T_2 measurements of our model BDPA/PS spin system at room temperature with a previously determined T_2 of $315ns$ [165] and with the cavity Q set purposefully to 800, i.e. impractically high for pulsed EPR experiments, to demonstrate the ability of the active cancellation method to recover echoes that are entirely buried in the resonator ring-down with high fidelity. The echo, for a given pulse spacing s, is recovered in a manner similar to which the Rabi oscillation signal was recovered, that is, the entire echo signal ($400ns$ long) is recorded piecewise in a series of $35ns$ long windows (constrained by the length of the cancellation window) that span the $400ns$ long time domain echo signal. Representative echo traces are shown in the inset of Fig. 6.4. To eliminate any deleterious effects from the FID after the 180○ pulse, we implement a two-step, $90_x - \tau - 180_x$ and $90_x - \tau - 180_{-x}$, phase cycling scheme, where the inverted phase of the 180° pulse causes the subtraction of the FID when adding the echo signals. The integrated amplitude of each phase-cycle corrected echo is recorded as a function of the inter-pulse spacing to generate the T_2 decay curve shown in Fig. 6.4. We observe echoes that begin to refocus during the end of the 180° pulse (Fig. 6.4A), echoes during the ring-down (Fig. 6.4B), and echoes detected after the ring-down has decayed below the saturation limit of the signal detector (Fig. 6.4C). The time-domain decay of the echoes from sections B and C of Fig. 6.4 fit to a mono exponential decay with a time constant of $314 \pm 6ns$, which agrees with the previously determined T_2 of $315ns$ for this sample [165]. The distorted echo signal at an inter-pulse spacing of less than $200ns$ (Fig. 6.4A) is likely due to the interference with residual pulse power inside of the resonator, as discussed in Appendix **??**.

6.5 Conclusion and Outlook

In summary, we find that by actively cancelling the resonator ring-down we can measure unperturbed signal from the EPR spin system at any time during a given pulse sequence, including within the pulse duration and during the pulse ring-down. At the current stage of hardware development, the active cancellation technique is successful with a solid-state amplifier at relatively low power ($10-20W$) compared to a TWTA that offers high powers in the $1kW$ range as employed for traditional pulse EPR applications. However, with recent advances in resonator design, in particular micro coil resonators with very high conversion factors, it is feasible to carry out many conventional pulse EPR experiments with high fidelity even with low microwave power (W to mW) [189, 196, 197, 198, 199]. One could thus imagine employing the AC method in conjunction with a micro coil setup in practical pulse EPR settings. Obviously, the utility of the active cancellation method would be more immediate and far greater if traditional TWTAs yielding kW powers can be employed, or if solid-state amplifiers with ¿100 W output became broadly available. We see two obstacles to overcome in employing the active cancellation method with the TWTA: (1) the physical limitation of the gated noise from the TWTA saturating the detection electronics and preventing signal detection, which imposes an intrinsic limitation on the microwave power one can apply to the method, and (2) the cancellation waveform fidelity operating in the non-linear output regime of the TWTA. For the active cancellation method to succeed, it is necessary to detect signal while the amplifier is on. Thus, the limitation on the maximum power that can be applied is not from the peak pulse power, but from the noise that originates from the high power amplifier. The TWTA employed for this study (Applied Systems Engineering M/N 117) has a gated noise of approximately $1mW$ that saturates the detection electronics, such that the detection of signal is not possible during the gated output of the TWTA. It is worth noting that the noise output of the solid-state amplifier (approximately 10 nW) pushes the detection electronics to near the saturation regime. However, with sufficient averaging the detector behaves linearly and we are able to detect signal. For the detector employed in the study a noise power of approximately 100 nW completely overwhelms the detection electronics and prevents detection of signal. Thus, with the current detection electronics and hardware, the use of the TWTA for the active cancellation method is not feasible. This limitation may be overcome with new high power low noise solid-state amplifiers and low noise microwave sources, or a detector configuration that allows for a higher saturation point, which may be obtained by placing an attenuator in front of the microwave limiter. The other issue is to overcome the non-linear nature of the TWTA, such that one could accurately control the shape and phase of the output waveform. The high power non-linear distortion of the TWTA on the shape and phase of an output waveform is reproducible. Therefore, in scenario lacking a physical model describing the transformation, one can calibrate for this via a lookup table or other empirical scheme, thus reliably controlling the output shape and phase of a given waveform.

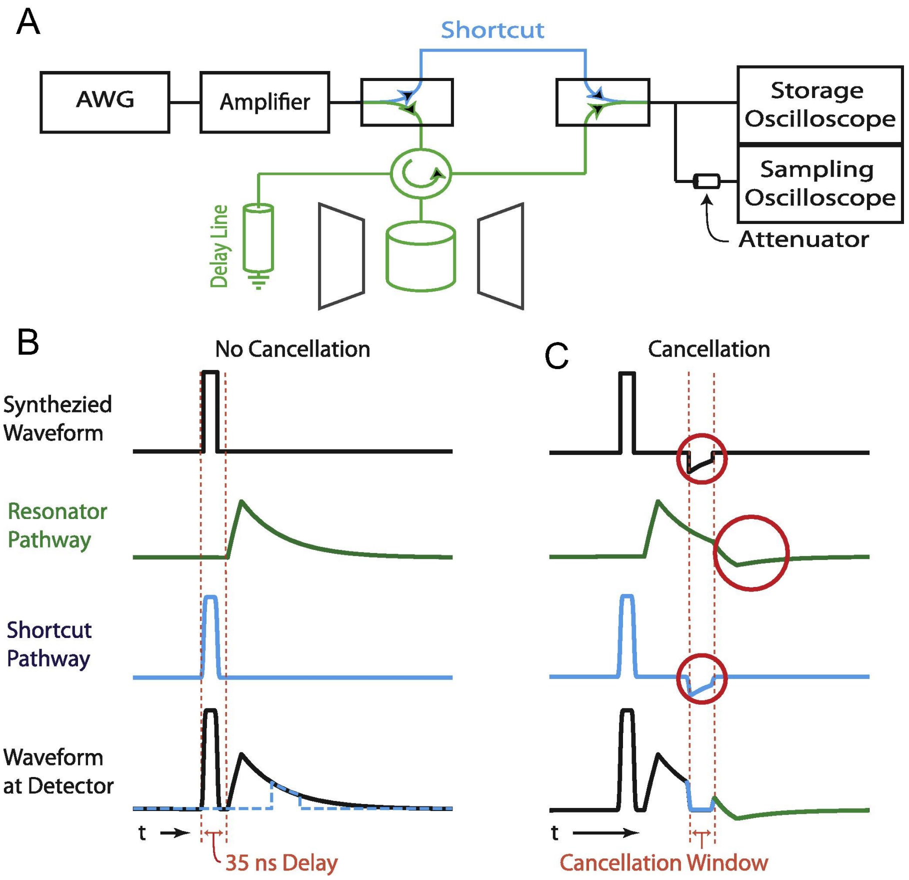

Figure 6.1: The schematic of the delay line assembly is shown in A. The effect the delay line assembly has on a given excitation pulse is shown in B. A cancellation pulse is calculated from the ring-down shown in blue dashed line in B "waveform at detector". The cancellation pulse, the negative of the blue dashed trace in B "waveform at detector", is shown in the red circle behind the excitation pulse in C "synthesize waveform". The cancellation pulse is shown circled in red in both the resonator and shortcut pathways of C. The cumulative effect of the cancellation pulse is shown in C "waveform at detector" where the respective colors correspond to the effect of the cancellation pulse from each individual pathway. The cancellation window is generated from the cancellation pulse, from the shortcut pathway, meeting with and destructively interfering with the ring-down, from the resonator pathway. Electron spin signal from the action of the excitation pulse alone is detectable inside of the 35 ns long cancellation window.

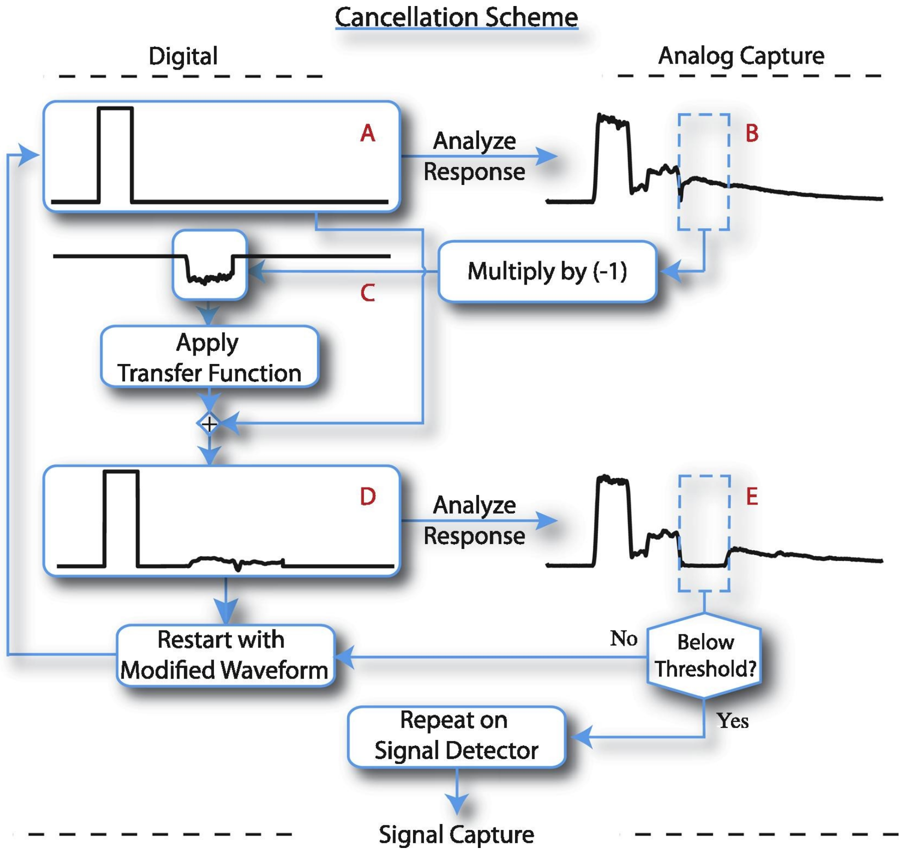

Figure 6.2: The optimization scheme for producing and optimizing a given cancellation pulse. An initial digital excitation pulse (A) is synthesized, amplified, sent through the waveguide assembly, attenuated, and measured on a sampling oscilloscope (B). The transfer function for this specific cancellation pulse (shown as negative magnitude in C) is calculated and subsequently applied. The transfer function corrected cancellation pulse is spliced into the original digital excitation pulse at the correct relative time (D). Waveform (D) is synthesized and the residual microwave power remaining in the cancellation window is measured (E). If the residual power is above the threshold, the cancellation pulse is optimized by restarting the scheme with waveform (D) in place of waveform (A), and the corrected cancellation pulse is added to the original cancellation pulse in waveform (A) instead of replacing the original cancellation pulse. Once the residual microwave power is below the threshold the higher sensitivity heterodyne signal detector is used to further optimize the cancellation pulse shape following the same scheme. Once the residual microwave power inside of the cancellation window is below $10nW$ it is possible to observe EPR signal.

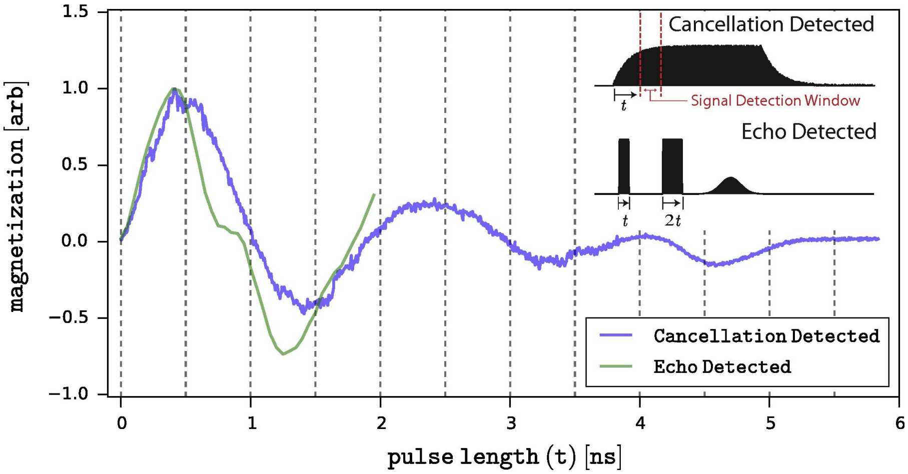

Figure 6.3: The Rabi oscillation of the unpaired electron in the BDPA/PS sample measured with (blue) and without active cancellation (green). The inset illustrates the two separate schemes in which the Rabi oscillations are detected.

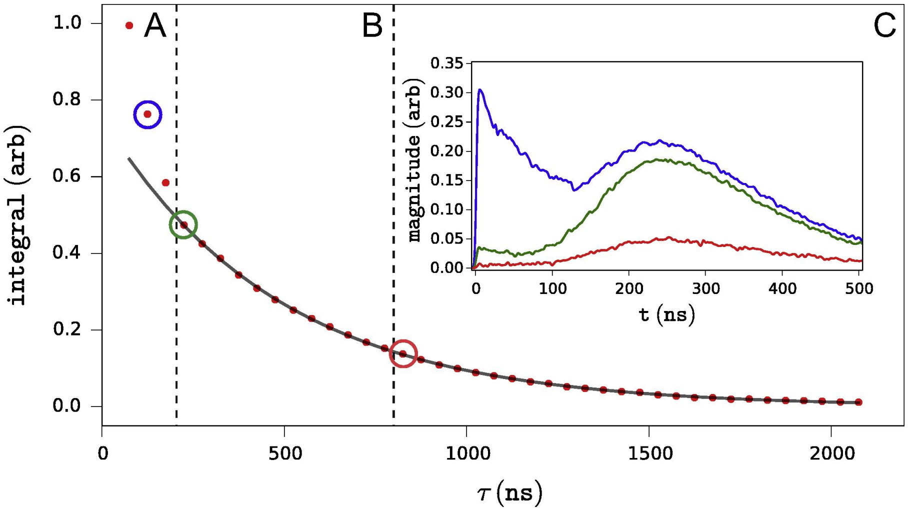

Figure 6.4: The Hahn echo decay of the unpaired electron of BDPA embedded on a polystyrene matrix measured with a resonator Q of 800. The echoes corresponding to the coloured circled data points are shown in the inset, where the time axis corresponds to the start of signal detection. Three regions are noted. In region C the echoes are detected after the ring-down has sufficiently decayed to allow for signal detection. In region B the echoes that are recovered during the detector dead-time by active cancellation. In region A the echoes are recovered by active cancellation but distorted by the 180° pulse.

Chapter 7

High Field Pulsed EPR with AWG

7.1 Abstract

We report here on the implementation of arbitrary waveform generation (AWG) capabilities at $200GHz$ into an Electron Paramagnetic Resonance (EPR) and Dynamic Nuclear Polarization (DNP) instrument platform operating at $7T$. This is achieved with the integration of a $1GHz$, 2 channel, digital to analog converter (DAC) board that enables the generation of coherent arbitrary waveforms at Ku-band frequencies with $1ns$ resolution into an existing architecture of a solid state amplifier multiplier chain (AMC). This allows for the generation of arbitrary phase- and amplitude-modulated waveforms at $200GHz$ with $> 150mW$ power. We find that the non-linearity of the AMC poses significant difficulties in generating amplitude-modulated pulses at $200GHz$. We demonstrate that in the power-limited regime of $\omega_1 < 1MHz$ phase-modulated pulses were sufficient to achieve significant improvements in broadband ($> 10MHz$) spin manipulation in incoherent (inversion). We also discuss the application of optimal control to the high field AWG to show that validity of AWG at high field.

7.2 Introduction

High field Electron Paramagnetic Resonance (EPR) is an established technique that has provided important insights in many material and biological applications. The use of advanced pulsed and multi-dimensional EPR techniques at high magnetic fields, despite its obvious prospects, is hampered by the limited available microwave power at frequencies above W-band ($> 100GHz$) where high-power amplifiers $> 150mW$ are not available, or are prohibitively expensive. The limited microwave power available for high-field EPR results in low nutation frequency ω_1 values of at most $4.2MHz$ at $180GHz$ and $2.1MHz$ at $275GHz$, even when using an efficient TE_{011} single mode resonator. This hampers the feasibility or quality of important pulsed EPR experiments, including double electron-electron resonance (DEER) at high fields. The low ω_1 available at high field/frequency of a few MHz is in stark contrast to the $70MHz$ ω_1 routinely achieved at X-band frequencies where DEER and other pulsed EPR experiments are routinely performed.

EPR experiments are typically limited by the available pulse bandwidth, hence the push for higher power and shorter pulses. Amplitude and phase modulated microwave pulses, generated by an arbitrary waveform generator (AWG), have proven a viable solution to the limitations in the available pulse bandwidth. AWG-generated waveform-modulated pulses allow for high level of control over spin manipulations which results in a dramatically improved pulse performance at a given microwave power. Owing to such capabilities, AWG pulses have been successfully applied for decades in nuclear magnetic resonance (NMR), and have become integral to virtually all modern NMR spectroscopy and imaging experiments. In contrast, only recent advances in high speed electronics permitted the implementation of AWGs in pulsed EPR experiments. There are numerous recent applications detailing the use of AWGs in pulsed EPR experiments at conventional, X-band ($\sim 9.5GHz$) and Q-band ($\sim 35GHz$), frequencies that showcase the gains afforded by arbitrary amplitude and phase modulation of microwave pulses. However, AWG controlled pulsed EPR at higher frequencies have not been demonstrated to date.

The application of AWGs to pulsed EPR spectroscopy is expected to have an even greater impact at higher magnetic fields. The rational is twofold: (1) the available microwave power ($50200mW$) and thus the pulse bandwidth ($1MHz$) is significantly less compared to lower microwave frequencies and (2) the EPR spectral width is typically much wider due to the increased g-factor resolution. For instance the spectral width of a simple nitroxide radical is $1GHz$ at $7T$ and spans a few GHz or more for common transition metal ions. This discrepancy between the typical pulse excitation bandwidth ($1MHz$) and the width of the EPR spectra ($fewGHz$) significantly limits the sensitivity of high field pulse EPR experiments, as well as presents an opportunity for significant sensitivity gains by AWG implementation. The cost of overcoming the pulse bandwidth limitation without increasing microwave power is an increased pulse length. This poses a limitation on the shaped-pulse utility for systems with short relaxation times (compared to the required pulse length) or strong electron spin-spin couplings (compared to the inverse pulse length), and requires a compromise between the length of the best performing shaped pulse and the relaxation time or the electron spin-spin coupling strength.

To this end we integrate a homebuilt AWG system with $1GHz$ bandwidth into a $200GHz$ microwave bridge with dual EPR and Dynamic Nuclear Polarization (DNP) capabilities for the purpose of confronting the pulse bandwidth limitation. We implement the AWG into the $12GHz$ pulse forming network of the microwave bridge. The AWG features two digital to analog converter (DAC) boards that drive the I and Q channels of an IQ mixer. The IQ mixer mixes the DAC outputs with the $12GHz$ microwave. The output microwave pulses are then up-converted to $200GHz$ by an amplifier multiplier chain (AMC). This design achieves amplitude and phase modulation at $200GHz$, similar to other systems designed for rotational spectroscopy at sub-THz frequencies.

In the following we describe the integration of the AWG unit into a $200GHz$ solid-state source powered EPR/DNP spectrometer platform. We showcase broadband manipulation of up to $20MHz$ bandwidth of the EPR spectrum at $200GHz$ using phase-modulated chirp pulses that largely exceeds the bandwidth possible with standard rectangular pulses at the available microwave power. Using phase modulated pulses we demonstrate broadband inversion and coherent echo formation on electron spins in a BDPA/poly styrene mixture, and in the P_1 centers of a ^{13}C enriched diamond sample. Finally, we present the performance and limitations of the $200GHz$ IQ mixer and AMC-based microwave bridge for generating both amplitude and phase modulated pulses.

7.3 Results

7.3.1 Hardware setup and design

The conventional approach for implementing arbitrary phase and amplitude modulated pulses at X-band frequencies is to mix the arbitrary waveform with a carrier frequency at (or close to) the final operating X-band frequency of around $9.5GHz$ using an IQ mixer. The drop in power due to insertion loss of the $12GHz$ IQ mixer ($79dB$) is compensated for by further amplification after mixing, culminating in the final high-power amplification stage of the $1kW$ TWT amplifier. However, the absence of a microwave amplifier operational at high frequencies ($> 100GHz$) prevents us from replicating this approach at $200GHz$, where the power drop due to the insertion loss of a 200 GHz mixer cannot be compensated for by subsequent amplification. Instead, we integrate the AWG into the spectrometer at the $12GHz$ base frequency, before the AMC. To achieve this, an additional channel that includes the IQ mixer for mixing the AWG waveform with the 12 GHz base signal was added to the pulse-forming unit of our spectrometer.

The overall design of the 200 GHz quasi optics (QO) bridge for dual EPR and DNP operation was described in detail in a recent publication [200]. The system utilizes three digitally programmable, continuous wave (CW) $12GHz$ synthesizers to operate (i) the main microwave transmitter channel source for pulsed and CW EPR and (ii) the second transmitter channel for pump-probe Electron Double Resonance (ELDOR) experiments, as well as (iii) to generate the LO (local oscillator) reference for the 200 GHz sub-band mixer in the heterodyne receiver system. The microwave output of the main $12GHz$ CW transmitter source (i) is sliced, and if desired mixed, with coherent AWG waveforms produced with a fast ($1GHz$) DAC board for phase and amplitude modulation. The generation of this $12GHz$ AWG waveform occurs in the pulse-forming unit before it is sent to the $*16$ amplifier multiplier chain (AMC) chain to produce the pulsed and shaped output at $200GHz$. The induction mode-selected $200GHz$ EPR signal is routed via the QO bridge to the $200GHz$ sub-band mixer, where it is down-converted to an intermediate frequency of $3GHz$. The $3GHz$ signal is amplified using a $46dB$ gain low-noise amplifier, before being down converted to a DC signal by mixing with a coherent $3GHz$ signal from a reference arm, and then digitized for detection.

7.3.2 Pulse forming unit

The pulse forming unit operating at $12GHz$ frequency consists of three main modules. In the AWG module the CW signal from the transmitter source is mixed, using the IQ mixer (IQ0618LXP by Marki microwave), with the AWG waveform. The digital to analog converter (DAC) board used for arbitrary waveform generation in this work consists of an Ethernet accessible FPGA board (Altera Stratix II by Altera) that drives two independent DAC boards with $14-bit$ resolution and $1GHz$ bandwidth that form two analog output channels that are used to produce the real and imaginary DAC $1GHz$ waveforms. In addition, there are three digital ECL (emitter-coupled logic) channels synchronized with the analog ones, by virtue of operating at the same high frequency clock, which can be used to trigger/control other devices, such as microwave switches and digitizers. The AWG can be set to generate the programmed waveform, either immediately after finishing the data transfer or upon receiving an external trigger. This DAC board was previously used in a digital X-band EPR spectrometer constructed in our lab [193] and was designed by the Martinis group at UCSB [164]. The shaped $\sim 12GHz$ waveform output after the IQ mixer passes through a low pass filter (FLP-1740 by Marki microwave), mainly to suppress the leakage signal at the 2nd harmonic of the carrier frequency ($24GHz$). It is important to ensure careful calibration of the power level of the shaped pulses such that the input power of the full-amplitude shaped pulse is sufficient to operate the AMC at saturation while the leakage at carrier and image frequencies is below the power threshold for engaging the AMC. Subsequently the shaped signal is routed into the phase cycling unit. The manually selectable bypass channel, selected by a manual SP2T switch, (SM-2min by RLC electronics) in the AWG module is installed to carry out experiments that do not require AWG operation with the same transmitter source as used for AWG, and to maintain backward compatibility with existing pulse sequences and operating procedures. The bypassed signal is routed into the same phase cycling module as the shaped signal.

The signal generated from the AWG module is routed via a fast $< 10ns$ SP2T (F9120AH by General Microwave) switch to either a bypass channel (0° phase shift) or through a voltage controlled phase shifter hardware that is set nominally for an 11.25° phase shift at the $12GHz$ operating frequency, thus resulting in a 180° degree phase shift at $200GHz$ (following $*16$ multiplication in the AMC). While phase cycling can of course be achieved without relying on an analog phase shifter unit by digitally reprogramming the waveform produced by the AWG, it is beneficial to retain the hardware-based phase cycling capability, especially when delays associated with AWG data transfer rates become significant. The source switching module is designed to allow for quick ($< 10ns$) switching between the main and the ELDOR source (transmitter source 2) to allow for pulsed double-resonance experiments. The two SPST switches used in the source switching module are identical (SWM-DJV-1DT-2ATT by American Microwave Corporation) with a $1ns$ rise and fall time. In principle the AWG eliminates the need for a dedicated ELDOR source to generate multiple frequencies. However, this functionality is retained for experiments that require long ELDOR pulses that exceed the $15\mu s$ memory limit of the current AWG module.

7.3.3 Timing and control software

To properly integrate the pulse shaping capabilities into the pulsed EPR spectrometer, it is necessary to accurately synchronize (preferably to $< 1ns$) the (i) waveform generation by the DAC, (ii) microwave switch operations: the SP2T switch in the phase cycling module and the two switches in the source switching module, and (iii) digitizer triggering for detection (not shown on the schematic). In the previously debuted digital X-band AWG spectrometer developed in the Han lab [164], precise switch and detector synchronization with the waveform generation and transmission were achieved by utilizing three auxiliary ECL digital channels available on our DAC board to operate all microwave switches, as well as to trigger the oscilloscope that was used to digitize the signal. These ECL channels are timed to the same precise $250MHz$ internal (on board) clock to time the generation of the arbitrary waveform, therefore avoiding any synchronization issues between waveform generation and device triggering. However, the number of currently available ECL channels (three) is not sufficient to operate the three switches in the $200GHz$ setup, as well as trigger the digitizer in the more complex $200GHz$ spectrometer. Thus, an alternative control scheme was implemented. Specifically, the microwave bridge is now controlled by a 24 channel PulseBlasterESR-Pro (PB) TTL pattern generation board (SpinCore Technologies Inc) that handles the overall timing of the experiment. The PB controls the hardware timing of all three mw switches, externally triggers the DAC board for waveform generation, and the triggers the digitizer for signal detection. The drawback of this method of timing control is a $4ns$ jitter in the timing of the AWG waveform output relative to the timing of the mw switches and the digitizer that are now all directly controlled by the PB. This jitter is a consequence of the PB and AWG operating on different internal clock frequencies of $300MHz$ and $250MHz$, respectively. Waveform generation by the DAC board starts in sync with the $250MHz$ clock cycle. By virtue of the PB and AWG boards not having their internal clock cycles synchronized, a PB trigger can be received any time during the $4ns$ clock cycle of the AWG, and thus resulting in a $< 4ns$ jitter that generates uncertainty in the position of the waveform relative to the time of the trigger received by the AWG. Currently, this does not present a problem given the maximum excitation bandwidth used in this work of $20MHz$ which corresponds to an echo widths of $> 50ns$ and with $< 4ns$ jitter does not cause a significant broadening problem. If needed achieving more precise timing in the future is rather straightforward, since it is possible to operate the relevant mw switches and digitizer trigger using the auxiliary ECL channels available on the AWG board, and leave the less critical timing to be controlled by the PB board. However, an advantage of the current combined configuration, where the AWG is operating in slave mode relative to PB, is that it allows for the generation of pulse sequences that exceed the $15\mu s$ memory limit of the currently available AWG, as long as only part ($< 15\mu s$) of the pulse sequence involves shaped pulses. In the future, the installment of an AWG with greater memory than $15\mu s$ will alleviate such limitations.

The overall software control of the 200GHz spectrometer, including arbitrary waveform generation for shaped pulses, is carried out using the Specman4EPR software (FeMi Instruments, LLC). In its current implementation the software includes a library of several standard parameterized shaped pulses and a possibility to load user-generated waveforms. For operation using standard parameterized shaped pulses the waveform parameters are accessible as user-defined variables in the experiment, thus allowing for easy and real-time adjustment and optimization of the pulse shapes. To deal with non-standard waveforms it is possible to load user-defined waveforms directly into the Specman4EPR software that were generated with other programs (e.g. MATLAB, Python, Mathematica) and saved as ASCII files. The user-defined waveforms can be interpolated to a given pulse duration, additionally the offset from the carrier frequency, as well as the phase of the user-defined pulse can be adjusted by the user. In addition to generating waveforms for shaped pulses and controlling the overall timing of the experiment, the SpecMan4EPR software also controls the frequency of the two digitally programmable transmitter sources, the voltage controlled phase shifter in the phase cycling module, the voltage controlled attenuator in the ELDOR channel (located between the transmitter source II and preceding the source switching module), and the overall intensity of the AMC output. The output power of the AMC is regulated via changes in voltage applied to user controlled attenuation (UCA) port of the AMC chain. The variable voltage used to control the voltage controlled phase shifter, the voltage controlled attenuator of the ELDOR source and voltage controlled AMC output is provided by the USB-6001 DAQ (National Instruments).

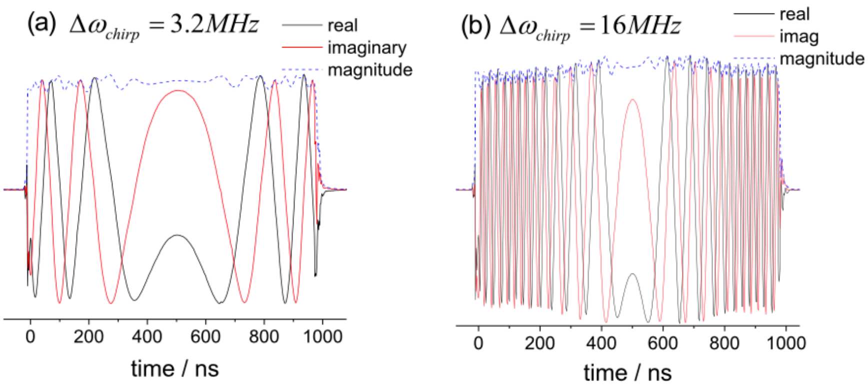

Figure 7.1: Experimentally acquired waveforms for $1\mu s$ long chirp pulses at $197.549GHz$ as acquired via the leak into the induction mode using phase sensitive detector.

7.3.4 Spectrometer performance

Adiabatic inversion

Phase-modulated linear chirp pulses can perform inversion of the magnetization over a very large bandwidth which, excluding the edge effects and relaxation, is equal to the width of the chirp pulse ($\Delta\omega_{chirp}$) and is commonly referred to as an adiabatic passage pulse. During the course of an adiabatic passage (from low to high frequency) the effective B_1 magnetic field vector in the rotating frame changes from being aligned along the $+z$ direction (pulse frequency is below resonance) to being in the xy plane (on resonance) and finally to being aligned along the $-z$ direction (pulse frequency is above the resonance). When the adiabaticity condition:

$$\frac{kT_2}{\omega_1} >> 1 >> \frac{k}{2\pi\omega_1^2} \tag{7.1}$$

is fulfilled, the electron spin magnetization vector will stay aligned parallel (or antiparallel in the case of the sweep from high to low frequency) with the direction of the effective B_1 magnetic field vector, resulting in the inversion of its direction at the end of the pulse. Here, ω_1 is the nutation frequency of the B_1 magnetic field vector, k the chirp sweep rate and T_2 the transverse electron spin relaxation time. The right side of Eq. 7.1 ensures that the change in the direction of the magnetic field vector is adiabatic so the magnetization vector can follow the magnetic field vector. Given this relationship the chirp rate k can be increased when higher microwave power (higher ω_1) is available, and thus for a given pulse length the inversion bandwidth $\Delta\omega_{chirp}$ can be increased without compromising the adiabaticity. Fulfilling the left side of Eq. 7.1 ensures that the passage through the xy plane is rapid enough so that no significant dephasing occurs while the magnetization resides in the xy plane. The adiabaticity is minimal exactly on resonance where the magnitude of the effective magnetic field vector is the smallest. It follows that the dependence of the inversion efficiency is conveniently described using the on-resonance adiabaticity, also known as critical adiabaticity (Q_{crit}). For a linear frequency sweep with constant irradiation strength, ω_1, the on-resonance or critical adiabaticity is given by

$$Q_{crit} = \frac{2\pi\omega_1^2}{k} \tag{7.2}$$

From Eq. 7.2 it follows that for high fidelity inversion the requirement can be simplified as $Q_{crit} >> 1$ since it ensures the right side of Eq. 7.1 is fulfilled for the entire adiabatic pulse. For a non-resonant setup (no mw cavity) as described here the $150mW$ output of the AMC at $200GHz$ results in a nutation frequency of $\omega_1 \approx 0.60.8MHz$ for non-lossy thin samples such as diamond. In practice when setting $Q_{crit} = 5$, the "adiabatic" chirp rate for our setup becomes $k = 2\pi\omega_1^2 5 \approx 0.450.8\frac{MHz}{\mu s}$. Since slight reduction of the critical adiabaticity $Q_{crit} < 5$ can still be tolerated and it is more beneficial to have a faster chirp rate to diminish effects of relaxation decay during the pulse. We chose the maximum chirp rate for our inversion experiments to be $k = 1MHz/\mu s$.

The situation is different for higher volume samples where the sample thickness ex-

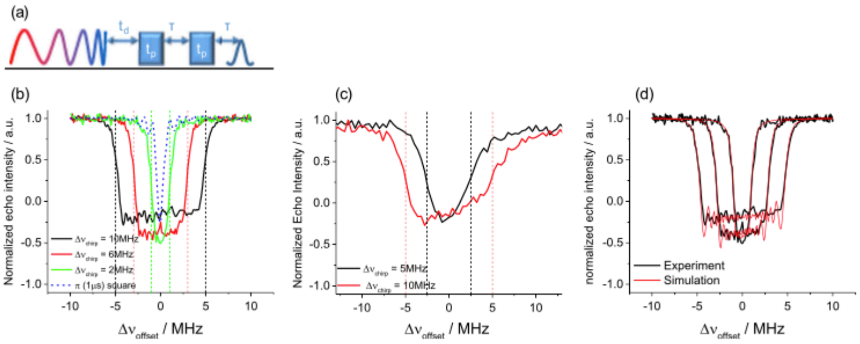

Figure 7.2: Pulse sequence used for measuring inversion profile of a chirp pulse. (a) Experimental inversion profiles of a $10\mu s$ chirp pulse for BDPA in o-terphenyl sample (b) and P_1 center of diamond (c). Vertical dashed lines denote the nominal $\Delta\omega_{chirp}$ for each pulse bandwidth respectively. Overlay of experimental and simulated data for BDPA in o- terphenyl sample. (d) Experimental parameters BDPA sample: $t_p = 500ns$; $s = 800ns$; $td = 2.4\mu s$; Frequency $197.589GHz$; Diamond sample: $t_p = 400ns$; $s = 800ns$; $t_d = 500ns$; Frequency $197.529GHz$.

ceeds the $200GHz$ wavelength ($1.5mm$). In this case lower nutation frequencies and larger ω_1 inhomogeneity were observed. For 1% BDPA in o-terphenyl sample the nutation frequency was $\omega_1 = 0.353MHz$, determined by the analysis of the nutation and square pulse inversion experiments.

To experimentally measure the inversion profile of a chirp pulse we used a three-pulse experiment (Fig. 7.2a), where the effect of the chirp pulse (first pulse) is monitored by changes in the echo produced by the last two pulses. The experimentally detected inversion profiles obtained for 1% BDPA in o-terphenyl sample using a $10\mu s$ long chirp pulses for $\Delta\omega_{chirp} = 10$, 6 and $2MHz$ are shown in Fig. 7.2b as black red and green curves, respectively. The inversion profile obtained for a $1\mu s(\pi)$ pulse is shown as blue dashed line for comparison. Fig. 7.2c shows similar inversion experiments performed on a center line of a P_1 center in 10% ^{13}C enriched diamond using a $10\mu s$ long chirp pulses with $\Delta\omega_{chirp} = 10$ and $5MHz$ as red and black curves, respectively. The vertical dashed lines denote the nominal bandwidth of these two chirp pulses. It is evident that broadband spin manipulation is successfully achieved over the whole $\Delta\omega_{chirp}$ bandwidth in both cases.

The electron spin relaxation times for the BDPA sample are $T_1 = 260\mu s$ and phase memory time $T_m = 3.3\mu s$, and for the diamond sample are $T_1 = 115\mu s$ and phase memory time $T_m = 800ns$, as measured by saturation recovery and two-pulse echo decay experiments, respectively. Substituting the above values for T_m in place of the T_2 into Eq. 7.1 reveals that the left side of the equation is not fulfilled for $k \sim 1MHz$ and $\omega_1 < 1MHz$ for both BDPA and diamond samples.

Consequently, we expect significant reduction of the inversion efficiency due to the transverse relaxation (T_2) during the pulse. Indeed, as expected, from not fulfilling the left side of Eq. 7.1 a complete inversion is not achieved due to signal loss from the dephasing. Nevertheless, to illustrate the gain in inversion efficiency achieved with the broadband chirp pulses we plotted, the inversion profile of a $1\mu s$ rectangular (π) pulse a blue dashed line on Fig. **??**b. It is clear that the inversion profile width of the $10MHz$ chirp pulse exceeds that of the rectangular π pulse by approximately one order of magnitude without compromising the inversion efficiency. This is of course at the expense of the longer $10\mu s$ versus $1\mu s$ pulse length. For EPR experiments such as DEER, where maximizing the overall change in the magnetization (ΔMz) for all spin packets over a broad bandwidth is of interest such chirp pulses will be clearly beneficial, granted higher microwave power (higher ω_1) becomes available at $200GHz$, as demonstrated for X- band an Q-band experiments.

For the diamond sample the shape of the inversion profiles is visibly skewed. This is the effect of T_1 relaxation. For the diamond sample the length of the pulse ($10\mu s$) is not negligible relative to the T_1 relaxation time ($115\mu s$), so that the spin packets that were affected in the beginning of the chirp pulse have more time to relax back to equilibrium before they are detected by an echo compared to spin packets that are affected at the end of the chirp pulse. Note that the chirp pulse sweep direction was from positive to negative offset frequency. As expected for the BDPA sample the slope of the inversion profile is much more gradual due to a reduced effect of the T_1 relaxation ($T_1 = 260\mu s$) during the $10\mu s$ pulse.

Interestingly, for the BDPA sample, $5MHz$ and $2MHz$ chirp pulses show better on-resonance inversion efficiency compared to the monochromatic rectangular pulse. This is despite longer time between inversion and detection for the chirp versus rectangular pulse. To understand this effect and to quantitatively access the performance of our phase-modulated pulses, we compare the experimental data to simulated results for a $S = 1/2$ system including the effects of the T_2 and T_1 relaxation times. The results of these simulations, overlaid with the experimental data are presented in Fig. **??**C for BDPA sample. For a much larger BDPA sample a ω_1 inhomogeneity was taken into account explicitly, it was neglected for the much smaller and thinner diamond sample. For the latter the ω_1 intensity was estimated from a nutation experiment that was published previously. Notably for both BDPA and diamond samples we had to use $T_2 > T_m$ in the simulations to arrive at a good agreement with the experimental data. This is not surprising since the T_m measurement provides only a lower limit for T_2. This is attributed to either effects of instantaneous diffusion or to the need to use a rotating frame relaxation time (T_{1q}) which accounts to the fact that relaxation with and without on-resonance mw irradiation is different.

7.4 Ongoing work

7.4.1 Optimal control pulses - Coherent control

We applied known optimal control techniques to the high field EPR experiment in an attempt to show the viability of the AWG. We show how the pulse is optimized to achieve a certain target state. In this case we set the target state such that a spin echo forms a given time τ after the pulse.

For simplicity, we focus on pulses for uncoupled spins, where the equation of motion reduces to the well-known Bloch equations. We consider the problem of transferring an initial magnetization vector $\vec{M}(0) = (0,0,1)^t$ (where the superscript t indicates the transpose of the vector) to a desired target state $\vec{F}$ for a specified range of offsets $\nu_{min} \leq \nu \leq \nu_{max}$ and with a desired degree of tolerance with respect to B_1 inhomogeneity or B_1 miscalibration, which is specified by a B_1 scaling factor $s_{min} \leq s \leq s_{max}$. In order to optimize a given (shaped) pulse with x and y amplitudes $u_x(t)$ and $u_y(t)$ and overall duration T, we need to define an overall quality factor that quantifies the performance of the pulse [143]

$$\Phi = \frac{1}{N_{off} N_s} \sum_{k=1}^{N_{off}} \sum_{l=1}^{N_s} \phi(\nu_k, s_l) \tag{7.3}$$

where N_{off} and N_s are the numbers of equidistant samples at offsets ν_k and the B_1 scaling factor s_l, respectively. Defining a final magnetization vector $\vec{M}(T)$ and the target vector $\vec{F}$, the choice for the local quality factor $\phi(\nu_k, s_l)$ are:

$$\phi(\nu_k, s_l) = \vec{M}(T) \cdot \vec{F} \tag{7.4}$$

The local quality factor $\phi(\nu_k, s_l$ is maximized. Based on the definition of the global quality factor Φ, the optimal-control-based GRAPE (gradient ascent pulse engineering) algorithm can be used to optimize a given initial pulse shape by calculating the gradient $\frac{\delta\Phi}{\delta u_\alpha(j)}$ where $u_x(j)$ and $u_y(j)$ are the x and y pulse amplitudes at time slice j,assuming that the pulse shape is digitized in N time slices with $1 \leq j \leq N$. The overall gradient $\frac{\delta\Phi}{\delta u_\alpha(j)}$ is simply the average of the local gradients $\frac{\delta\phi(\nu_k,s_l)}{\delta u_\alpha(j)}$, which can be efficiently calculated based on only one forward propagation of the magnetization vector $\vec{M}(t)$ (starting from the given initial magnetization vector $\vec{M}(0) = (0,0,1)^t$ and one backward propagation of the so-called adjoint vector $\vec{\lambda}(t)$, starting from $\vec{\lambda}(T) = \left(\frac{\delta\phi}{\delta M_x}, \frac{\delta\phi}{\delta M_y}, \frac{\delta\phi}{\delta M_z}\right)^t$. Where $\vec{\lambda}(T) = \vec{F}$. With the magnetization vector $\vec{M}_j$ and the adjoint vector $\vec{\lambda}_j$ at each time slice j, the local gradient is simply $(\vec{M}_j \times \vec{\lambda}_j)_\alpha$, i.e. the x and y components of the cross product. Based on the overall gradient a given initial pulse can be improved in an iterative fashion by either following the gradient direction with a small step size or by using more elaborate methods such as conjugate gradients or quasi Newton methods.

Appendix A

Appendix

A.1 Hydration Dynamics

A.1.1 Correlation between Diffusive Water Retardation and Peptide Hydropathy

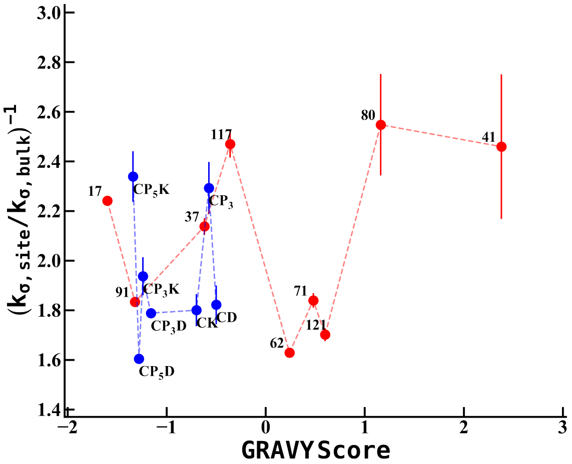

Figure A.1: k_σ retardation (DW retardation) plotted against the GRAVY score for each peptide. The number adjacent to each data point corresponds to the peptide label. The red data points show the CheY inspired 5-residue long peptides and the blue data points show the poly proline peptides described in Table A.1

We explore the correlation between the DW and surface hydropathy on the CheY inspired 5 residue long peptides. We compute the GRand AVerage of hydropathY (GRAVY) score for each peptide, listed in Table A.1 along with the relevant chemical properties. The GRAVY score is computed by taking the average of the hydropathy values of each amino acid in the peptide. The hydropathy values for each amino acid are given by Kyte and Doolittle [201]. We find that there is no correlation between the DW measured on the surface of the peptides and the GRAVY score of each peptide.

Table A.1: Properties of the 5-residue long peptide segments and the poly proline peptides. The hydrophilicity of each peptide is given by the grand average of hydropathy ($GRAVY$) score, computed by protparam.

Peptide	Sequence	Molecular Weight (Da)	# of Charged Residues	# of Aliphatic Residues	GRAVY Score
M17C	STCRR	621.71	2	0	-1.600
E37C	EACDG	493.39	2	2	-0.620
D41C	GVCAL	461.58	0	4	2.380
N62C	MPCMD	595.74	1	3	0.240
T71C	LKCIR	631.83	2	2	0.480
A80C	MSCLP	549.70	0	3	1.160
K91C	EACKE	578.64	3	1	-1.320
E117C	TLCEK	592.71	2	1	-0.360
N121C	KLCKI	603.82	2	2	0.600
CD	CD	236.24	1	0	-0.5
CK	CK	249.33	1	0	-0.7
CP3	CPPP	412.50	0	3	-0.575
CP3K	CPPPK	540.68	1	3	-1.24
CP3D	CPPPD	527.59	1	3	-1.16
CP5K	CPPPPPK	734.91	1	5	-1.342
CP5D	CPPPPPD	721.83	1	5	-1.285

A.1.2 Correlation between k_σ and k_{Low}

To show that the relaxation rates k_σ and k_{Low} and ultimately the DW and BW are decoupled we plot the retardation in k_σ against the enhancement in k_{Low} in Fig.

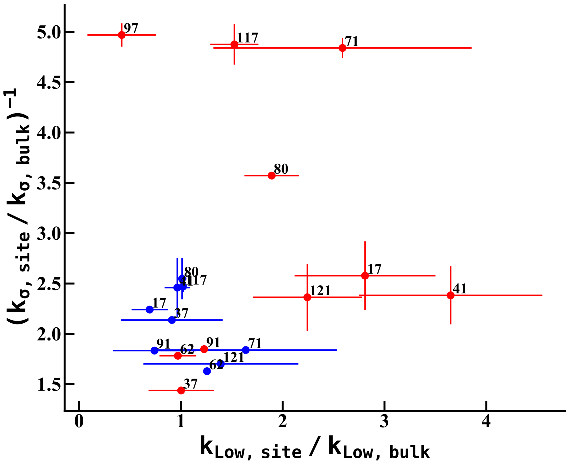

Figure A.2: Correlation between k_σ and k_{Low} for the CheY protein in red and the CheY inspired 5-residue long peptides in blue. The label adjacent to each point indicates the site on the protein or the composition of the peptide.

??. There is no correlation between the k_σ retardation and the k_{Low} enhancement. The empirical interpretation implies that the two relaxation rates are probing separate timescales of motion and are thus decoupled from one another.

A.1.3 Analysis of Diffusion Time on MSD Values from MD Simulation

We examine the retardation in the MSD as a function of delay time (τ) for the CheY protein, 5 residue peptide segments, and the 5 residue cys mutant peptide segments. The delay time describes how long water molecules are allowed to diffuse before the MSD is calculated. Fig. A.3 shows the effect of the delay time on the MSD retardation for the three systems. The trend in MSD retardation from site to site on the CheY protein and the 5 residue peptides is robust in that the trend is qualitatively invariant to changes in the delay time. In the main text we show results from a 10ps waiting time because this produces the largest contrast from site to site on the protein.

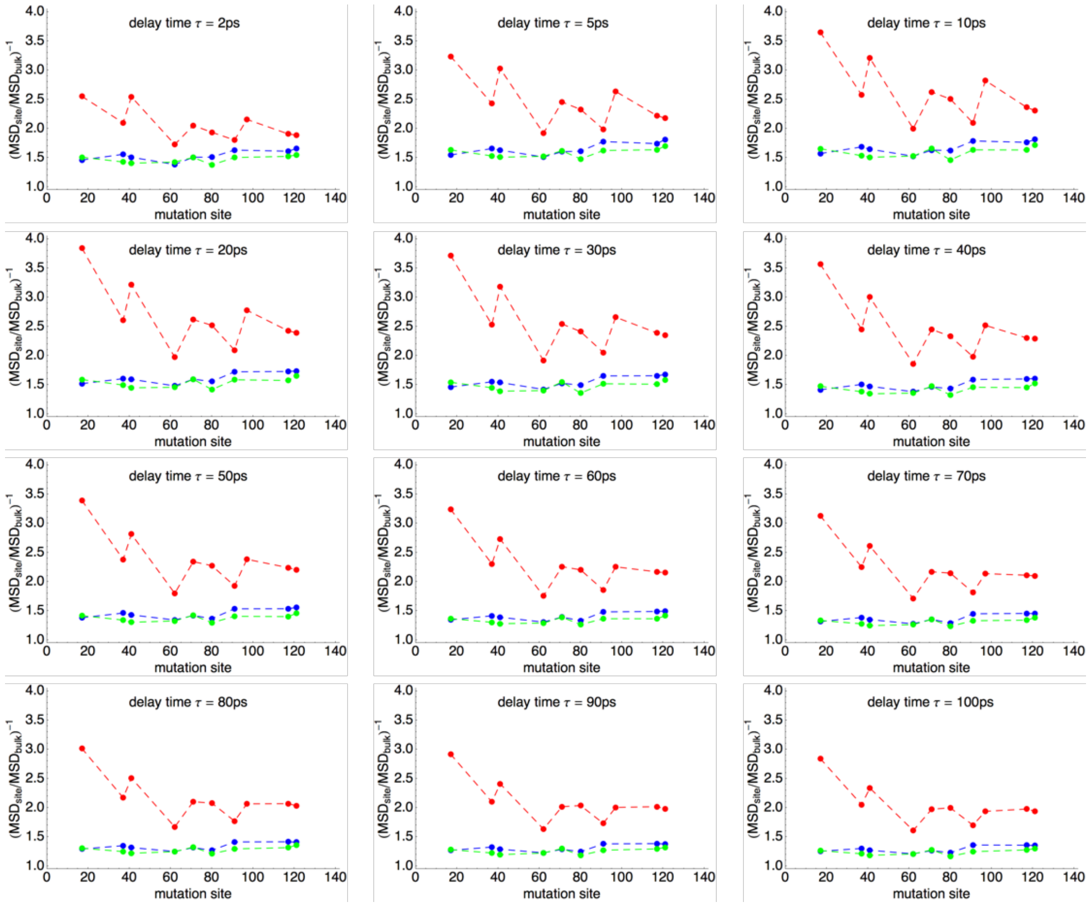

Figure A.3: The MSD retardation for the sites on the CheY protein are shown in red, the 5 residue CheY peptides in blue, and the 5 residue cys mutant peptides in green is shown as a function of delay time τ, indicated at the top of each plot.

A.1.4 Analysis of Spin Label Motion

First derivative ESR spectra were acquired on a Bruker EMX X-band ($9.8GHz$) spectrometer at room temperature equipped with a high-sensitivity dielectric ER102 cavity. The spectra were acquired on protein samples of $3.5\mu L$ volume, placed into quartz capillaries of $0.6mm$ inner diameter (VitroCom), which was then held by a Teflon sample holder and mounted inside the microwave cavity. ESR spectra were acquired using signal averaging of $\sim 6 - 16$ scans over a field sweep of $100 - 120G$, a microwave power of $\sim 18mW$, and modulation amplitudes of $0.4G$, which was optimized to the

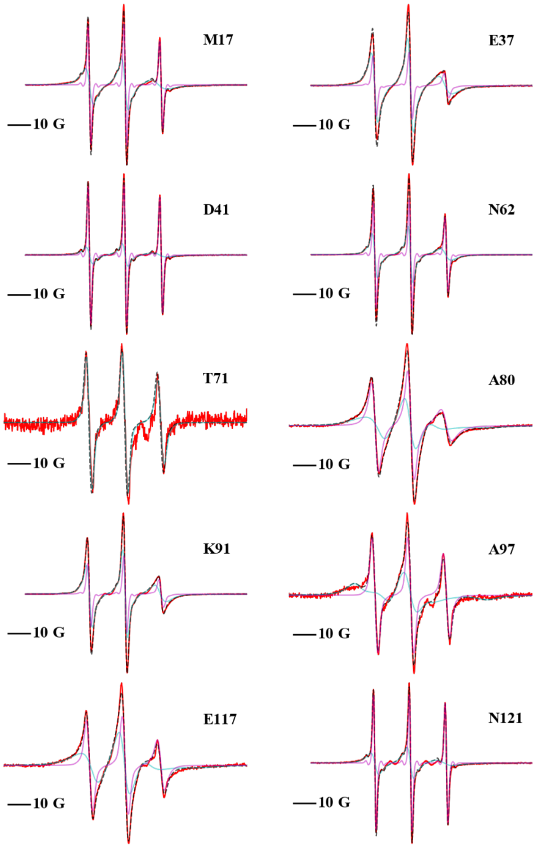

Figure A.4: The cw-EPR spectrum of all spin labeled sites on CheY (red), the fit (black), and the separate components to the fit in (cyan and magenta).

natural line width of the spectra.

The line shape of the EPR spectra serve as a readout of the spin label motion. The line width and position is sensitive to both the motion and the local environment of the nitroxide radical of the spin label [176]. Following the methods of Freed and Hubbell we use line shape analysis to estimate a correlation time of the spin label motion. For each site, except T71, we find two characteristic motions. The fast motion ($10-100s$ of ps) is representative of the spin label rotating about the bonds that connect the spin label to the protein. The slower motion ($1-10s$ of ns) is representative of the spin label moving in concert with the protein backbone [67, 66, 65]. All spectra were fit with the multi component EPR fitting package produced by Christian Altenbach (that can be downloaded at `http://www.biochemistry.ucla.edu/biochem/Faculty/Hubbell/`) using the NLSL fitting routine developed by Budil [176]. The experimentally measured spectra and the corresponding fits, including each component are shown in Fig. A.4.

Table A.2: The cw-EPR extracted correlation times of protein ($\tau_{Protein}$) and spin label (τ_{SL}) motion for each site on the protein.

Mutant	$\tau_{Protein}$ (ps)	τ_{SL} (ns)
M17C	86.7	1.81
E37C	376	1.47
D41C	48.8	1.51
N62C	109	1.15
T71C	202	–
A80C	835	4.15
A97C	290	1.11
E117C	227	5.27
N121C	404	3.30

A.1.5 Analysis of Correlations with Spin Label Motion

The spin label attached to the protein adds an extra degree of heterogeneity. Here we analyze any impact this added degree of heterogeneity may have on the measured ODNP parameters or any correlation the spin label motion may have with the protein surface parameters. We measured cw-EPR spectra of the spin label attached to the CheY surface and we determined the correlation time of motion of the spin label by line shape analysis, detailed in the next section. As expected we find that there are two timescales of spin label motion for all sites on the protein, excluding site T71C. There is a fast time scale, $10s$ to $100s$ of ps, that corresponds roughly to independent spin label motion the spin label rotating about the disulfide bond that attaches it to the protein, and a slower time scale, $1 - 10ns$, that corresponds roughly to the protein sidechain motion [67, 66, 65].

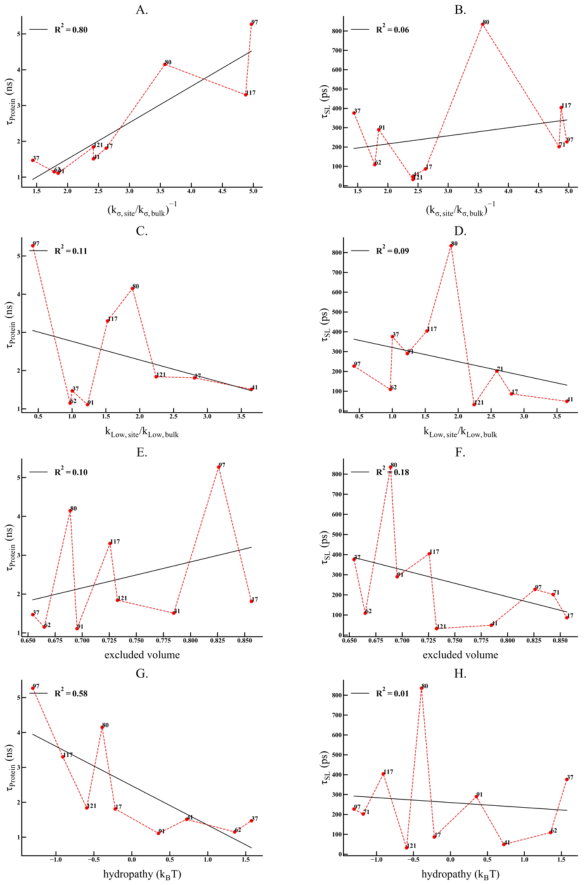

Figure A.5: Shows the correlations between the spin label timescales of motion with the relevant ODNP parameters k_σ (A & B) and k_{Low} (C & D) and the excluded volume (E & F) and hydropathy (G & H) of the protein surface.

We investigate any correlations that may exist with the spin label motion. We compare the slow timescale of spin label motion to k_σ and find that there is a moderate to strong correlation with $R^2 = 0.8$ Fig. A.5A. We compare the fast timescale of spin label motion to k_σ and find no correlation Fig. A.5B meaning that the independent spin label motion is uncoupled from the hydration water motion. Taken at face value, this suggests that the protein motion, captured by the slow timescale of spin label motion, is coupled to the hydration water motion. However, these results can only be taken as preliminary as the spin label motion only serves as a rough proxy for protein backbone and side chain dynamics. This will be the area of a future study. It is important to point out that motion on the ns timescale (slow timescale) is too slow to directly influence the k_σ relaxation rate.

We do not find any correlation between k_{Low} and either timescale of spin label of motion Fig. A.5 C & D. We do not find any correlation between excluded volume and either timescale of spin label motion Fig. A.5 E & F. We also find a moderate correlation ($R^2 = 0.58$) between surface hydropathy and the slow timescale of spin label motion which mirrors the correlation between k_σ and hydropathy that suggests the motion is slower at more hydrophobic sites.

A.1.6 Analysis of Hydrophilic Sites on CheY Surface

We further investigate the role of excluded volume on hydration water retardation by separating the sites based on their respective hydropathy. We find that the hydrophilic sites on CheY have a strong correlation to the excluded volume ($R^2 = 0.92$), Fig. A.6A, and that the hydrophobic sites have no correlation to the excluded volume, Fig. A.6B.

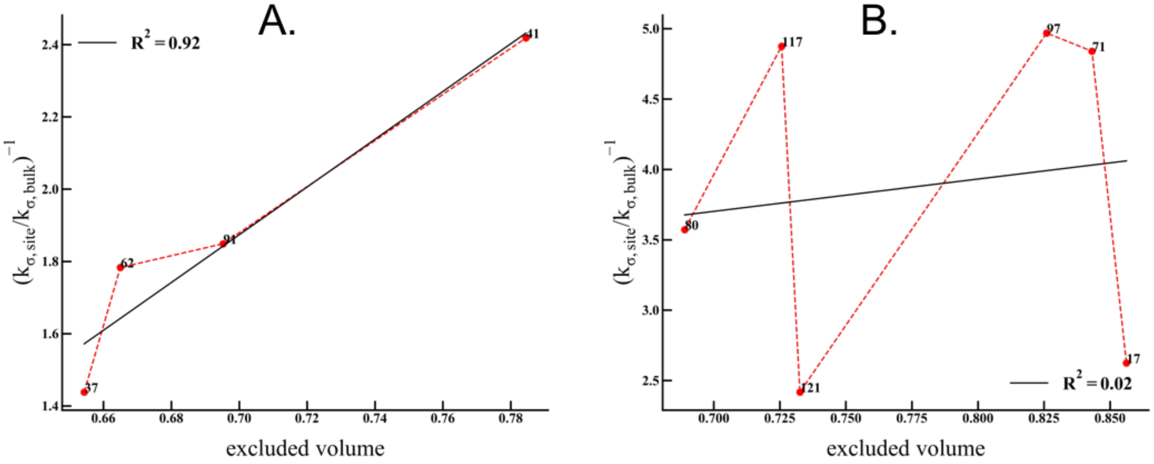

Figure A.6: This shows the correlation between k_σ retardation and the excluded volume that exists for the hydrophilic sites (A) and hydrophobic sites (B) on CheY.

A.2 AWG Development

A.2.1 Magnet and Microwave Source

A schematic overview of the spectrometer is shown in Fig. 5.1 in the main text. A field controller (Bruker ER 032M) controls the $0.35T$ static field generated by the electromagnet (Bruker ER 070, Fig. 5.1 #1). A YIG-tuned oscillator (MicroLambda MLSL-1178, Fig. 5.1 #2) generates a low-phase-noise ($53dBc/Hz$ at $100Hz$ offset, $60dBc/Hz$ at $1kHz$ offset, $93dBc/Hz$ at $10kHz$ offset) $+10dBm$ cw X-band sine wave, which is split, with one channel pre-amplified (MiniCircuits ZX60-183+, Fig. 5.1 #3) to $18dBm$ and fed into the home-built AWG unit (Fig. 5.2) and the other channel sent to the heterodyne receiver. Communication with the field controller occurs through a GPIB connection; a GPIB-Ethernet Controller 1.2 by Prologix, LLC allows the Python library to communicate with this and all other GPIB devices through a TCP/IP socket. The microwave source is computer controlled with a USB interface (FTDI FT245R embedded in the UM245R development board) together with the FTDI D2XX drivers that allow direct access to the device in the "bit-bang" mode, which permits one to set the voltage levels on the various pins simultaneously. Both the static field and microwave frequency can be set from a Python script, which can also read out the current Hall probe reading and whether or not the microwave source is currently phase-locked.

A.2.2 AWG Unit

The AWG unit is comprised of a two-channel 1 GHz DAC board (High Speed Circuit Consultants, software build 10, Fig. 5.1 #4), [202] four Gaussian filters (High Speed Circuit Consultants) that reduce output noise, two differential amplifiers (Fig. 5.1 #5) that drive the I and Q channels of an IQ mixer (Marki Microwave IQ- 0618, Fig. 5.1 #6), a low pass filter (Marki Microwave FLP-1250, Fig. 5.1 #7) that suppresses harmonics generated by the IQ mixer, and a directional coupler (Fig. 5.1 #8) that allows monitoring of the shaped microwave output of the AWG unit with $10dB$ of attenuation on a sampling oscilloscope (Tektronix 11801C, Fig. 1 #9) with two sampling heads (Tektronix SD 24, Tektronix SD 22). Additionally, each of the two differential amplifiers has a secondary output that can be monitored on a standard digital storage oscilloscope.

The DAC board was developed by John Martinis at UCSB [202] in collaboration with Steve Waltman (High Speed Circuit Consul- tants), and features two differential (i.e. two port) outputs with a $14 - bit$ (i.e. $42dB$) dynamic range and $1ns$ time resolution. The memory of the board allows for storage of up to $16\mu s$ long waveforms. Additionally, parts of the pulse sequence can be called independently and delays of arbitrary lengths can be inserted. The bandwidth limitation of the AWG unit is set by the I and Q inputs of the IQ mixer, which feature a bandwidth of $500MHz$ and thus make the IQ mixer the bandwidth limiting component in the setup. A significant advantage over commercially available AWGs is that the DAC board provides four differential ECL trigger outputs that can be utilized to control other components of the spectrometer. For this spectrometer, an ECL-to-TTL converter was built (ON Semiconductor ECLSOIC8EVB and MC100ELT21) to open and close the gate of a TWT amplifier. Another ECL trigger output triggers the sampling oscilloscope as well as the oscilloscope connected to the heterodyne receiver. Thus, the DAC board not only controls the phase and shape of the microwave pulses, but also functions as the central timing unit. The FPGA-based design of the DAC board also allows for custom modifications of its functionality, if desired.

A.2.3 Microwave Transmission

The shaped pulse output of the AWG, approximately $10dBm$ coming out of the mixer, is pre-amplified (MiniCircuits ZX60- 183+) by $24dB$ and further amplified (Fig. 5.1 #10) by either a $1kW$ traveling wave tube (TWT) amplifier (Applied Systems Engineering Model 117), which has a gain of $60dB$ and a P_1dB of $61dBm$, or an array of four solid-state amplifiers. The four amplifiers (Advanced Microwave PA2803-24) each yield a gain of $30dB$ (P_1dB of $35dBm$ each) and are adjusted with phase shifters to yield coherent outputs that are combined for a net gain of $36dB$ to reach a maximum power of approximately $12 - 13W$ of power ($41dBm$). Specifically, the array of solid-state amplifiers uses 3 splitters (MiniCircuits ZX10-2-126) to divide the signal into 4 pathways, 3 phase shifters (Aeroflex Weinschel 980-4) to adjust the phase of 3 of the pathways to match the first one, before the signal is fed into the 4 amplifiers, and 4 isolators (UTE Microwave, CT-5450-OT) to protect the amplifier outputs from reflections before the 4 pathways are combined (Narda Microwave 4326-4) again. The amplifiers are powered by a linear power supply (Protek 18020M), mounted on a thick aluminum block and additionally cooled by computer fans. A 4-port circulator, with port 4 terminated (Cascade Research X-43-2, Fig. 5.1 #11), directs the microwave pulses to the resonator (Bruker ER4118X-MD5, Fig. 5.1 #12) that holds the sample and returns the reflected signal to the detector.

For the purposes of monitoring the system, a directional coupler (Fig. 5.1 #13) directs $20dB$ of reflected signal to the sampling oscilloscope. A second directional coupler, placed in front of the YIG-tuned source (Fig. 5.1 #2), directs $20dB$ of the X-band carrier wave to the second channel of the sampling oscilloscope, where it is used as a reference to determine the reflected microwave signal with absolute phase information.

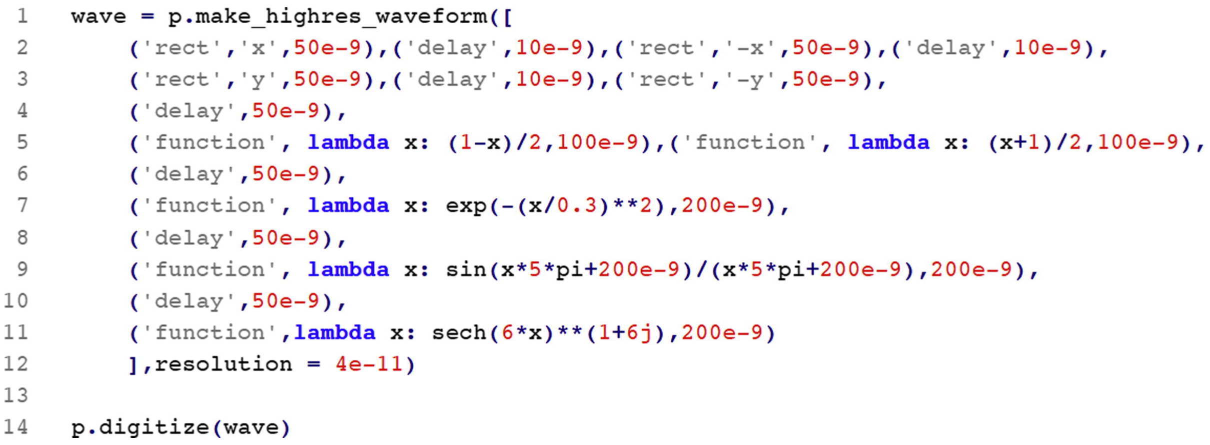

```
wave = p.make_highres_waveform([
    ('rect','x',50e-9),('delay',10e-9),('rect','-x',50e-9),('delay',10e-9),
    ('rect','y',50e-9),('delay',10e-9),('rect','-y',50e-9),
    ('delay',50e-9),
    ('function', lambda x: (1-x)/2,100e-9),('function', lambda x: (x+1)/2,100e-9),
    ('delay',50e-9),
    ('function', lambda x: exp(-(x/0.3)**2),200e-9),
    ('delay',50e-9),
    ('function', lambda x: sin(x*5*pi+200e-9)/(x*5*pi+200e-9),200e-9),
    ('delay',50e-9),
    ('function',lambda x: sech(6*x)**(1+6j),200e-9)
    ],resolution = 4e-11)

p.digitize(wave)
```

Figure A.7: Code that generates a pulse sequence in this case a composite pulse comprising 4 rectangular pulses of different phases, a triangular pulse, a Gaussian pulse, a truncated sinc pulse, and an adiabatic rapid passage sech/tanh pulse.

A.2.4 Microwave Detection

The microwave signal returning from the resonator is sent to a 3-port circulator (Cascade Research X43-10-1, Fig. 5.1 #14) and from there to a PIN-diode limiter (Aeroflex ACLM-4571FC31 K, Fig. 5.1 #15), which protects the low-noise amplifier (Miteq AMF- 3F-09001000-13-8P-L-HS, Fig. 5.1 #16) from damage due to high power microwaves. The aforementioned circulator (Fig. 5.1 #14) directs any microwave power reflected from the limiter into a high-power terminator (Fig. 5.1 #17).

To obtain heterodyne detection, the amplified signal and the output of the microwave carrier are input into another IQ mixer (Marki Microwave IQ-0618, Fig. 5.1 #18), generating two IF (i.e. intermediate frequency) signals in quadrature, which have a frequency range between DC and 500 MHz. These signals are amplified by two amplifiers (MiniCircuits ZFL-500+, Fig. 5.1 #19) and detected with a (time-base) digital storage oscilloscope (Agilent Technologies MSO7104B, Fig. 5.1 #20) or a high speed digitizer card (Agilent Acqiris 1082A).

A.2.5 Waveform Generation

The Python scripts that communicate with the DAC board allow arbitrary waveforms to be generated on-the-fly. These can be based on analytical descriptions or specified with arbitrary time resolution. Fig. A.7 shows an example: this pulse sequence generates the waveform shown in Fig. 5.4.

The function "make_highres_waveform(list, resolution)" can be called with a list of tuples that define (1) the type of pulse, (2) the phase of the pulse, and (3) the length of the pulse or delay. The first parameter can be "rect" (rectangular pulse), "delay", or "function" (defined by a function here a lambda (i.e. inline) function giving an analytical expression for the pulse waveform). A rectangular pulse uses the second argument to define the pulse phase, which can be either "x", "y", "-x", "-y" or any angle between 0° and 360° (Fig. A.7, lines 2 and 3). The third parameter defines the length of a pulse in units of seconds. In case of a delay, the second parameter defines its length. If the pulse type "function" is chosen, the second parameter is a function that defines the pulse shape as a function of time; here we employ lambda (inline) functions to generate analytically described functions that can be edited on-the-fly. Fig. A.7 shows a triangular pulse (line 5), a Gaussian pulse (line 7), a truncated sinc pulse (line 9) and an adiabatic rapid passage sech/tanh pulse (line 11) as examples. The parameter "resolution" defines the time resolution for the pulse sequence $40ps$ in this case that can be arbitrarily chosen.

The function "digitize (wave)" (line 14) takes the desired waveform as an argument, filters it with a $1GHz$ Gaussian bandpass and down-samples it to a $1ns$ time resolution. The previously acquired calibration parameters (Appendix A.2.7) and transfer function calibration (Appendix **??**) are applied, the waveform is translated into commands for the DAC board, transferred to the DAC board, and synthesized as described in Appendix A.2.6. The language for pulse programming was kept simple to maximize user-friendliness. Arbitrary pulse shapes can be generated within a fraction of a second, and simple loops can be set up to perform two dimensional experiments, such as the T_2 experiment.

A.2.6 Digitization and Waveform Generation

To digitize and generate an arbitrary waveform with the AWG from analytical descriptions, the desired waveform is defined with arbitrary length and resolution, then filtered with a $1GHz$ Gaussian bandpass filter and down-sampled to a $1ns$ time resolution to match the resolution of the DAC board. The IQ mixer calibration (Appendix **??**) as well as the transfer function calibration (Appendix **??**) are applied to take hardware imperfections into account and match the desired waveform as closely as possible. Subsequently, the waveform is translated into commands for the DAC board and transferred to the system. The following describes this procedure:

1. Define a desired waveform of arbitrary length and resolution $w(t)$.
2. Filter with $1GHz$ Gaussian: $w(t) * e^{-\left(\frac{t}{1ns}\right)^2}$.
3. Reduce bandwidth to $1GHz$:$w_i = \int_0^\infty w(t)\delta(t - t_i)dt$ for t_i in $1ns$,$2ns$,...,pulse length.
4. Apply IQ mixer calibration (Appendix A.2.7)
5. Apply transfer function correction (Appendix **??**).
6. Translate w_i to DAC board commands.
7. Transfer waveform to DAC board.

where “$*$” indicates time-domain convolution.

A.2.7 IQ Mixer Calibration

The IQ mixer used for waveform synthesis exhibits three correctable imperfections:

1. An amplitude imbalance between the two channels, i.e. “parity imbalance”.
2. The phase angle between the two channels is not necessarily 90°.
3. Microwave leakage occurs when no voltage is applied to both channels.

To correct for all three of these issues, a plane wave U_{in} is generated via the DAC board, mixed with the reference oscillator via the IQ mixer, and the output waveform U_{out} is captured on the sampling oscilloscope. In general, where an input waveform, U_{in}, has the form

$$U_{in}(t) = \rho_{in} e^{(\imath\phi_{in}(t))} \tag{A.1}$$

where ρ_{in} and ϕ_{in} are real numbers giving, respectively, the amplitude and phase modulation of the waveform, the amplitude and phase of the output waveform will be altered according to equations

$$\mathscr{R}|U_{out}(t)| = (1 + B_{\mathscr{R}})A_{\mathscr{R}\rho_{in}}(t)\cos(\phi_{in}(t) + \nu_{\mathscr{R}}) + C_{\mathscr{R}} \tag{A.2}$$

$$\mathscr{I}|U_{out}(t)| = (1 + B_{\mathscr{I}})A_{\mathscr{I}\rho_{in}}(t)\cos(\phi_{in}(t) + \nu_{\mathscr{I}}) + C_{\mathscr{I}} \tag{A.3}$$

as a result of these imperfections. The $A_{\mathscr{R}}$ and $A_{\mathscr{I}}$ represent the output parity imbalance, the $B_{\mathscr{R}}$ and $B_{\mathscr{I}}$ represent the input parity imbalance, the $\nu_{\mathscr{R}}$ and $\nu_{\mathscr{I}}$ denote a phase shift (arising from slightly different path lengths in each channel), and the $C_{\mathscr{R}}$ and $C_{\mathscr{I}}$ represent the DC offset of the real (Eq. (A.2)) and imaginary (Eq. (A.3)) components of the output waveform.

Specifically, after outputting a plane-wave U_{out}, the real and imaginary components of the output waveform, which are captured on the sampling scope, are fit to equations (Eq. (A.2)) and (Eq. (A.3)), respectively, as a function of the input phase.

Once these calibration parameters have been determined, one can solve Eqs. (A.2) and (A.3) with a standard zero-finding algorithm to determine the input values of ρ_{in} and ϕ_{in} needed to yield any desired output amplitude and phase (i.e. $|U_{out}|$ and angle (U_{out})), respectively. This corrects the amplitude and phase of the output waveform. In particular, the microwave leakage is corrected by subtracting the terms $C_{\mathscr{R}}$ and $C_{\mathscr{I}}$ from the input waveforms real and imaginary components, respectively. This applies a voltage to each channel of the mixer to minimize microwave leakage at the output and allows for an isolation of more than $50dB$ post amplification.

The IQ mixer used for detection exhibits the same issues as the mixer used for waveform synthesis. Therefore, an analogous calibration procedure can be applied, the difference being that nonlinearities are accounted for in post processing.

A.2.8 Transfer Function Correction

To maximize the fidelity with which pulses are generated, the transfer function of the spectrometer can be taken into account as a final step by capturing the generated waveform and comparing it to the desired pulse shape. Linear response theory states that the output waveform, $p_{out}(t)$, can be described as a convolution of the input waveform, $p_{in}(t)$, with the impulse response of the system i.e. the inverse Fourier transform of the transfer function, $H(\nu)$), of the system. We represent this as

$$p_{out}(t) = p_{in}(t) * \mathscr{F}^{-1}H(\nu)(t) \tag{A.4}$$

where $\mathscr{F}^{-1}\ldots$ represents the inverse Fourier transform and $*$ again represents a time-domain convolution. After Fourier transformation, the transfer function in frequency space can be found, following from

$$\mathscr{F}p_{out}(t)(\nu) = \mathscr{F}p_{in}(t)(\nu)H(\nu) \tag{A.5}$$

The transfer function, $H(\nu)$, can be subsequently applied to the initial waveform function to generate the desired waveform $p_{cor}(t)$ as described in the procedure below.

Instead of using the desired output pulse to determine the transfer function, a $1ns$ rectangular pulse on each DAC channel can be used to determine the impulse response function of the spectrometer and the transfer functions for both channels H_A (corresponding to a real $1ns$ pulse) and H_B (corresponding to an imaginary $1ns$ pulse) are added to determine the total transfer function, H. The procedure is described below. This procedure was not utilized in the experiments presented, but offers opportunity for future applications.

Generate $1ns$ square pulse $p_{in}(t)$ on DAC channel A and capture impulse response $p_{out}(t)$ on sampling oscilloscope

1. Fourier transform the generated waveform to yield $\mathscr{F}p_{in}(t)(\nu)$ and the impulse response to yield $\mathscr{F}p_{out}(t)(\nu)$.
2. Find the transfer function $H(\nu) = \frac{\mathscr{F}p_{out}(t)(\nu)}{\mathscr{F}p_{in}(t)(\nu)}$.
3. Repeat steps 1 through 3 with DAC channel B to find total transfer function $H(\nu) = H_A + \imath H_B$

A.3 Active Cancellation

A.3.1 Transfer Function: To Produce a Cancellation Pulse

The cancellation pulse will exactly destructively interfere with the excitation pulses cavity reflection only if the precise amplitude and phase of the cancellation pulse is achieved at the signal detector. By defining the distortions that occur to the cancellation pulse en-route to the detector as a convolution Eq. A.6 of the system input (cancellation pulse) $x(t)$ with the impulse response function $h(t)$ we are able to account for the distortions caused by $h(t)$ on the input $x(t)$. It is more convenient to think of the convolution in frequency space Eq. A.7 in which the transfer-function $H(\nu)$ simply scales the frequencies of $X(\nu)$ to produce the output $Y(\nu)$.

$$y(t) = \int_{-\infty}^{\infty} h(t-\tau)x(\tau)dt \tag{A.6}$$

$$Y(\nu) = H(\nu)X(\nu) \tag{A.7}$$

Thus by determining $H(\nu)$ with sufficient accuracy, one is free to invert Eq. A.7, define a system output (e.g. the cancellation pulse), and calculate the system input $X(\nu)$ that produces the predefined system output $Y(\nu)$.

To calculate the transfer function $H(\nu)$, we synthesize a 1 ns square pulse (Fig SI-1 $x(t)$) (1 GHz bandwidth), send this pulse through the transmission line that connects the AWG to the signal detector, and detect the distorted 1 ns square pulse on the signal detector (Fig SI-1 $y(t)$). Upon Fourier transformation of $x(t)$ (the square pulse) and $y(t)$ (the detected distorted square pulse) (Fig SI-1 $X(\nu)$ and $Y(\nu)$) we calculate the transfer-function (Fig SI-1 $H(\nu)$) that describes the system from the AWG to the signal detector, which we apply to the cancellation pulse to achieve the correct cancellation

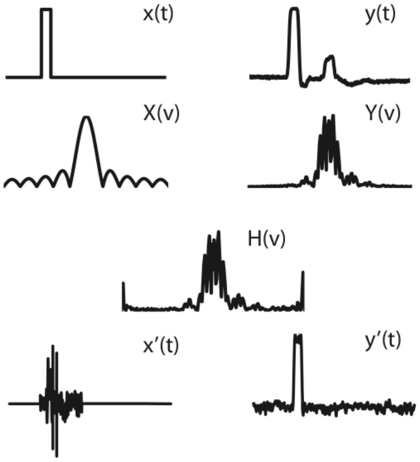

Figure A.8: An Illustration of the transfer-function calculation and use. A 1 ns square pulse $x(t)$ is synthesized and sent through the waveguide assembly generating $y(t)$ at the detector. $H(\nu)$ is calculate from the Fourier transform of $x(t)$ and $y(t)$ via Eq. A.7. $x(t)$ is calculated by inverting Eq. A.7 and generates $y(t)$ at the detector.

pulse shape and phase at the detector. For example we apply the transfer-function to the square pulse $x(t)$ and calculate a pulse (Fig SI-1 $x(t)$) that achieves the square pulse shape at the detector (Fig SI-1 $y(t)$). It is worth noting that this methodology is only successful when all of the microwave components that make up the pathway described by the transfer function are operated in the linear response regime w.r.t. both power and phase.

A.3.2 Rationalization of Distorted Echo Shape

In the inset of Fig 4 of the paper we show echo traces for various inter-pulse spacings. Its seen that the blue echo trace, corresponding to the integrand value circled in blue, is distorted, more so in the T_2 decay curve of Fig 4 its seen that the integrand of the distorted echo does not follow the mono exponential curve. First, we note that the phase cycling scheme employed removes the contribution of any FID arising from the inversion pulse to the echo shape. Interestingly, this distortion arises only when the inversion pulse is near maximum amplitude, and is possibly due to one or more of following reasons: the overlap of the 90° and 180° pulses inside of the resonator, the residual B_1 field of the hard 180° pulse interacting still with the spins at the time of the echo, or the lack of cancellation of an FID arising from the 90 excitation pulse.

Bibliography

[1] E. F. Pettersen, T. D. Goddard, C. C. Huang, G. S. Couch, D. M. Greenblatt, E. C. Meng, and T. E. Ferrin, *UCSF ChimeraA visualization system for exploratory research and analysis*, *Journal of Computational Chemistry* **25** (Oct., 2004) 1605–1612.

[2] J. M. Franck, A. Pavlova, J. A. Scott, and S. Han, *Quantitative cw Overhauser effect dynamic nuclear polarization for the analysis of local water dynamics*, *Progress in Nuclear Magnetic Resonance Spectroscopy* **74** (Oct., 2013) 33–56.

[3] M. F. Perutz, M. G. Rossmann, A. F. Cullis, H. Muirhead, G. Will, and A. C. T. North, *Structure of Hmoglobin: A Three-Dimensional Fourier Synthesis at 5.5-. Resolution, Obtained by X-Ray Analysis*, *Nature* **185** (Feb., 1960) 185416a0.

[4] T. M. Raschke, *Water structure and interactions with protein surfaces*, *Current Opinion in Structural Biology* **16** (Apr., 2006) 152–159.

[5] P. Ball, *Water as an Active Constituent in Cell Biology*, *Chemical Reviews* **108** (Jan., 2008) 74–108.

[6] J. A. Rupley and G. Careri, *Protein Hydration and Function*, in *Advances in Protein Chemistry* (C. B. Anfinsen, F. M. Richards, J. T. Edsall, and D. S. Eisenberg, eds.), vol. 41, pp. 37–172. Academic Press, Jan., 1991. DOI: 10.1016/S0065-3233(08)60197-7.

[7] H. S. Frank and M. W. Evans, *Free Volume and Entropy in Condensed Systems III. Entropy in Binary Liquid Mixtures; Partial Molal Entropy in Dilute Solutions; Structure and Thermodynamics in Aqueous Electrolytes*, *The Journal of Chemical Physics* **13** (Nov., 1945) 507–532.

[8] W. Kauzmann, *Some Factors in the Interpretation of Protein Denaturation11the preparation of this article has been assisted by a grant from the National Science Foundation.*, in *Advances in Protein Chemistry* (C. B. Anfinsen, M. L. Anson, K. Bailey, and J. T. Edsall, eds.), vol. 14, pp. 1–63. Academic Press, Jan., 1959. DOI: 10.1016/S0065-3233(08)60608-7.

[9] Y. Levy and J. N. Onuchic, *Water Mediation in Protein Folding and Molecular Recognition*, *Annual Review of Biophysics and Biomolecular Structure* **35** (2006), no. 1 389–415.

[10] T. N. Bhat, G. A. Bentley, G. Boulot, M. I. Greene, D. Tello, W. Dall'Acqua, H. Souchon, F. P. Schwarz, R. A. Mariuzza, and R. J. Poljak, *Bound water molecules and conformational stabilization help mediate an antigen-antibody association.*, *Proceedings of the National Academy of Sciences* **91** (1994), no. 3 1089–1093.

[11] D. N. LeBard and D. V. Matyushov, *Proteinwater electrostatics and principles of bioenergetics*, *Physical Chemistry Chemical Physics* **12** (Nov., 2010) 15335–15348.

[12] J.-M. Zanotti, M.-C. Bellissent-Funel, and J. Parello, *Hydration-Coupled Dynamics in Proteins Studied by Neutron Scattering and NMR: The Case of the Typical EF-Hand Calcium-Binding Parvalbumin*, *Biophysical Journal* **76** (May, 1999) 2390–2411.

[13] S. K. Pal, J. Peon, and A. H. Zewail, *Biological water at the protein surface: Dynamical solvation probed directly with femtosecond resolution*, *Proceedings of the National Academy of Sciences* **99** (Feb., 2002) 1763–1768.

[14] P. W. Fenimore, H. Frauenfelder, B. H. McMahon, and R. D. Young, *Bulk-solvent and hydration-shell fluctuations, similar to - and -fluctuations in glasses, control protein motions and functions*, *Proceedings of the National Academy of Sciences of the United States of America* **101** (Oct., 2004) 14408–14413.

[15] . Szyc, M. Yang, E. Nibbering, and T. Elsaesser, *Ultrafast Vibrational Dynamics and Local Interactions of Hydrated DNA*, *Angewandte Chemie International Edition* **49** (May, 2010) 3598–3610.

[16] S. Ebbinghaus, S. J. Kim, M. Heyden, X. Yu, U. Heugen, M. Gruebele, D. M. Leitner, and M. Havenith, *An extended dynamical hydration shell around proteins*, *Proceedings of the National Academy of Sciences* **104** (Dec., 2007) 20749–20752.

[17] H. Lichtenegger, W. Doster, T. Kleinert, A. Birk, B. Sepiol, and G. Vogl, *Heme-Solvent Coupling: A Mssbauer Study of Myoglobin in Sucrose*, *Biophysical Journal* **76** (Jan., 1999) 414–422.

[18] Y. Qin, L. Wang, and D. Zhong, *Dynamics and mechanism of ultrafast waterprotein interactions*, *Proceedings of the National Academy of Sciences* **113** (July, 2016) 8424–8429.

[19] J. Nickels, H. ONeill, L. Hong, M. Tyagi, G. Ehlers, K. L. Weiss, Q. Zhang, Z. Yi, E. Mamontov, J. Smith, and A. Sokolov, *Dynamics of Protein and its Hydration*

Water: Neutron Scattering Studies on Fully Deuterated GFP, *Biophysical Journal* **103** (Oct., 2012) 1566–1575.

[20] K. Wood, M. Plazanet, F. Gabel, B. Kessler, D. Oesterhelt, D. J. Tobias, G. Zaccai, and M. Weik, *Coupling of protein and hydration-water dynamics in biological membranes*, *Proceedings of the National Academy of Sciences of the United States of America* **104** (Nov., 2007) 18049–18054.

[21] J. R. Lewandowski, M. E. Halse, M. Blackledge, and L. Emsley, *Direct observation of hierarchical protein dynamics*, *Science* **348** (May, 2015) 578–581.

[22] J. L. Silva, T. C. R. G. Vieira, M. P. B. Gomes, A. P. A. Bom, L. M. T. R. Lima, M. S. Freitas, D. Ishimaru, Y. Cordeiro, and D. Foguel, *Ligand Binding and Hydration in Protein Misfolding: Insights from Studies of Prion and p53 Tumor Suppressor Proteins*, *Accounts of Chemical Research* **43** (Feb., 2010) 271–279.

[23] T. Li, A. A. Hassanali, Y.-T. Kao, D. Zhong, and S. J. Singer, *Hydration Dynamics and Time Scales of Coupled WaterProtein Fluctuations*, *Journal of the American Chemical Society* **129** (Mar., 2007) 3376–3382.

[24] F. Pizzitutti, M. Marchi, F. Sterpone, and P. J. Rossky, *How Protein Surfaces Induce Anomalous Dynamics of Hydration Water*, *The Journal of Physical Chemistry B* **111** (July, 2007) 7584–7590.

[25] A. C. Fogarty and D. Laage, *Water Dynamics in Protein Hydration Shells: The Molecular Origins of the Dynamical Perturbation*, *The Journal of Physical Chemistry B* **118** (July, 2014) 7715–7729.

[26] F. Sterpone, G. Stirnemann, and D. Laage, *Magnitude and Molecular Origin of Water Slowdown Next to a Protein*, *Journal of the American Chemical Society* **134** (Mar., 2012) 4116–4119.

[27] D. Russo, G. Hura, and T. Head-Gordon, *Hydration Dynamics Near a Model Protein Surface*, *Biophysical Journal* **86** (Mar., 2004) 1852–1862.

[28] D. Russo, R. K. Murarka, J. R. D. Copley, and T. Head-Gordon, *Molecular View of Water Dynamics near Model Peptides*, *The Journal of Physical Chemistry B* **109** (July, 2005) 12966–12975.

[29] D. Chandler, *Interfaces and the driving force of hydrophobic assembly*, *Nature* **437** (Sept., 2005) 640–647.

[30] S. Strazdaite, J. Versluis, E. H. G. Backus, and H. J. Bakker, *Enhanced ordering of water at hydrophobic surfaces*, *The Journal of Chemical Physics* **140** (Feb., 2014) 054711.

[31] A. J. Patel, P. Varilly, and D. Chandler, *Fluctuations of Water near Extended Hydrophobic and Hydrophilic Surfaces*, *The Journal of Physical Chemistry B* **114** (Feb., 2010) 1632–1637.

[32] D. Cui, S. Ou, and S. Patel, *Protein-spanning water networks and implications for prediction of proteinprotein interactions mediated through hydrophobic effects*, *Proteins: Structure, Function, and Bioinformatics* **82** (Dec., 2014) 3312–3326.

[33] A. Oleinikova, N. Smolin, I. Brovchenko, A. Geiger, and R. Winter, *Formation of Spanning Water Networks on Protein Surfaces via 2d Percolation Transition*, *The Journal of Physical Chemistry B* **109** (Feb., 2005) 1988–1998.

[34] B. D. Armstrong, J. Choi, C. Lpez, D. A. Wesener, W. Hubbell, S. Cavagnero, and S. Han, *Site-Specific Hydration Dynamics in the Nonpolar Core of a Molten Globule by Dynamic Nuclear Polarization of Water*, *Journal of the American Chemical Society* **133** (Apr., 2011) 5987–5995.

[35] W. Qiu, Y.-T. Kao, L. Zhang, Y. Yang, L. Wang, W. E. Stites, D. Zhong, and A. H. Zewail, *Protein surface hydration mapped by site-specific mutations*, *Proceedings of the National Academy of Sciences of the United States of America* **103** (Sept., 2006) 13979–13984.

[36] L. Zhang, Y. Yang, Y.-T. Kao, L. Wang, and D. Zhong, *Protein Hydration Dynamics and Molecular Mechanism of Coupled WaterProtein Fluctuations*, *Journal of the American Chemical Society* **131** (Aug., 2009) 10677–10691.

[37] J. T. King, E. J. Arthur, C. L. Brooks, and K. J. Kubarych, *Site-Specific Hydration Dynamics of Globular Proteins and the Role of Constrained Water in Solvent Exchange with Amphiphilic Cosolvents*, *The Journal of Physical Chemistry B* **116** (May, 2012) 5604–5611.

[38] C. Mattea, J. Qvist, and B. Halle, *Dynamics at the Protein-Water Interface from 17o Spin Relaxation in Deeply Supercooled Solutions*, *Biophysical Journal* **95** (Sept., 2008) 2951–2963.

[39] N. V. Nucci, M. S. Pometun, and A. J. Wand, *Site-resolved measurement of water-protein interactions by solution NMR*, *Nature Structural & Molecular Biology* **18** (Feb., 2011) 245–249.

[40] J. Yang, Y. Wang, L. Wang, and D. Zhong, *Mapping Hydration Dynamics around a -Barrel Protein*, *Journal of the American Chemical Society* **139** (Mar., 2017) 4399–4408.

[41] Y. Qin, L. Zhang, L. Wang, and D. Zhong, *Observation of the Global Dynamic Collectivity of a Hydration Shell around Apomyoglobin*, *The Journal of Physical Chemistry Letters* **8** (Mar., 2017) 1124–1131.

[42] K. H. Hausser and D. Stehlik, *Dynamic Nuclear Polarization in Liquids*, in *Advances in Magnetic and Optical Resonance* (J. S. Waugh, ed.), vol. 3 of *Advances in Magnetic Resonance*, pp. 79–139. Academic Press, Jan., 1968. DOI: 10.1016/B978-1-4832-3116-7.50010-2.

[43] I. Kaminker, R. Barnes, and S. Han, *Chapter Sixteen - Overhauser Dynamic Nuclear Polarization Studies on Local Water Dynamics*, in *Methods in Enzymology* (P. Z. Q. a. K. Warncke, ed.), vol. 564 of *Electron Paramagnetic Resonance Investigations of Biological Systems by Using Spin Labels, Spin Probes, and Intrinsic Metal Ions, Part B*, pp. 457–483. Academic Press, 2015.

[44] J. M. Franck, Y. Ding, K. Stone, P. Z. Qin, and S. Han, *Anomalously Rapid Hydration Water Diffusion Dynamics Near DNA Surfaces*, *Journal of the American Chemical Society* **137** (Sept., 2015) 12013–12023.

[45] L. Columbus and W. L. Hubbell, *A new spin on protein dynamics*, *Trends in Biochemical Sciences* **27** (June, 2002) 288–295.

[46] G. Mo, H. Zhou, T. Kawamura, and F. W. Dahlquist, *Solution Structure of a Complex of the Histidine Autokinase CheA with Its Substrate CheY*, *Biochemistry* **51** (May, 2012) 3786–3798.

[47] A. Pavlova, C.-Y. Cheng, M. Kinnebrew, J. Lew, F. W. Dahlquist, and S. Han, *Protein structural and surface water rearrangement constitute major events in the earliest aggregation stages of tau*, *Proceedings of the National Academy of Sciences* **113** (Jan., 2016) E127–E136.

[48] C.-Y. Cheng, J. Varkey, M. R. Ambroso, R. Langen, and S. Han, *Hydration dynamics as an intrinsic ruler for refining protein structure at lipid membrane interfaces*, *Proceedings of the National Academy of Sciences* **110** (Oct., 2013) 16838–16843.

[49] O. Fisette, C. Pslack, R. Barnes, J. M. Isas, R. Langen, M. Heyden, S. Han, and L. V. Schfer, *Hydration Dynamics of a Peripheral Membrane Protein*, *Journal of the American Chemical Society* **138** (Sept., 2016) 11526–11535.

[50] C.-Y. Cheng, J. Song, J. Pas, L. H. Meijer, and S. Han, *DMSO Induces Dehydration near Lipid Membrane Surfaces*, *Biophysical Journal* **109** (July, 2015) 330–339.

[51] J. M. Franck, M. Sokolovski, N. Kessler, E. Matalon, M. Gordon-Grossman, S.-i. Han, D. Goldfarb, and A. Horovitz, *Probing Water Density and Dynamics in the Chaperonin GroEL Cavity*, *Journal of the American Chemical Society* **136** (July, 2014) 9396–9403.

[52] B. D. Armstrong, M. D. Lingwood, E. R. McCarney, E. R. Brown, P. Blmler, and S. Han, *Portable X-band system for solution state dynamic nuclear polarization*, *Journal of Magnetic Resonance* **191** (Apr., 2008) 273–281.

[53] L. Hwang and J. H. Freed, *Dynamic effects of pair correlation functions on spin relaxation by translational diffusion in liquids*, *The Journal of Chemical Physics* **63** (Nov., 1975) 4017–4025.

[54] K. Volz and P. Matsumura, *Crystal structure of Escherichia coli CheY refined at 1.7-A resolution.*, *Journal of Biological Chemistry* **266** (1991), no. 23 15511–15519.

[55] B. Hess, C. Kutzner, D. van der Spoel, and E. Lindahl, *GROMACS 4: Algorithms for Highly Efficient, Load-Balanced, and Scalable Molecular Simulation*, *Journal of Chemical Theory and Computation* **4** (Mar., 2008) 435–447.

[56] W. D. Cornell, P. Cieplak, C. I. Bayly, I. R. Gould, K. M. Merz, D. M. Ferguson, D. C. Spellmeyer, T. Fox, J. W. Caldwell, and P. A. Kollman, *A Second Generation Force Field for the Simulation of Proteins, Nucleic Acids, and Organic Molecules*, *Journal of the American Chemical Society* **117** (May, 1995) 5179–5197.

[57] H. J. C. Berendsen, J. R. Grigera, and T. P. Straatsma, *The missing term in effective pair potentials*, *The Journal of Physical Chemistry* **91** (Nov., 1987) 6269–6271.

[58] T. Darden, D. York, and L. Pedersen, *Particle mesh Ewald: An Nlog(N) method for Ewald sums in large systems*, *The Journal of Chemical Physics* **98** (June, 1993) 10089–10092.

[59] B. Hess, H. Bekker, H. J. C. Berendsen, and J. G. E. M. Fraaije, *LINCS: A Linear Constraint Solver for Molecular Simulations*, *J. Comput. Chem* **18** (1997) 18–1463.

[60] S. Miyamoto and P. A. Kollman, *Settle: An analytical version of the SHAKE and RATTLE algorithm for rigid water models*, *Journal of Computational Chemistry* **13** (Oct., 1992) 952–962.

[61] S. Nos, *A molecular dynamics method for simulations in the canonical ensemble*, *Molecular Physics* **52** (June, 1984) 255–268.

[62] M. Parrinello and A. Rahman, *Polymorphic transitions in single crystals: A new molecular dynamics method*, *Journal of Applied Physics* **52** (Dec., 1981) 7182–7190.

[63] H. Acharya, S. Vembanur, S. N. Jamadagni, and S. Garde, *Mapping hydrophobicity at the nanoscale: Applications to heterogeneous surfaces and proteins*, *Faraday Discussions* **146** (July, 2010) 353–365.

[64] S.-H. Chong and S. Ham, *Interaction with the Surrounding Water Plays a Key Role in Determining the Aggregation Propensity of Proteins*, *Angewandte Chemie International Edition* **53** (Apr., 2014) 3961–3964.

[65] Y. Lou, M. Ge, and J. H. Freed, *A Multifrequency ESR Study of the Complex Dynamics of Membranes*, *The Journal of Physical Chemistry B* **105** (Nov., 2001) 11053–11056.

[66] D. E. Budil, S. V. Kolaczkowski, A. Perry, C. Varaprasad, F. Johnson, and P. R. Strauss, *Dynamics and ordering in a spin-labeled oligonucleotide observed by 220 GHz electron paramagnetic resonance.*, *Biophysical Journal* **78** (Jan., 2000) 430–438.

[67] Z. Liang and J. H. Freed, *An Assessment of the Applicability of Multifrequency ESR to Study the Complex Dynamics of Biomolecules*, *The Journal of Physical Chemistry B* **103** (July, 1999) 6384–6396.

[68] Y. Qin, M. Jia, J. Yang, D. Wang, L. Wang, J. Xu, and D. Zhong, *Molecular Origin of Ultrafast WaterProtein Coupled Interactions*, *The Journal of Physical Chemistry Letters* **7** (Oct., 2016) 4171–4177.

[69] E. J. Arthur, J. T. King, K. J. Kubarych, and C. L. Brooks, *Heterogeneous Preferential Solvation of Water and Trifluoroethanol in Homologous Lysozymes*, *The Journal of Physical Chemistry B* **118** (July, 2014) 8118–8127.

[70] R. G. Wei, M. Heyden, and J. Dzubiella, *Curvature Dependence of Hydrophobic Hydration Dynamics*, *Physical Review Letters* **114** (May, 2015) 187802.

[71] G. Niehues, M. Heyden, D. A. Schmidt, and M. Havenith, *Exploring hydrophobicity by THz absorption spectroscopy of solvated amino acids*, *Faraday Discussions* **150** (July, 2011) 193–207.

[72] C. Malardier-Jugroot, M. E.Johnson, R. K.Murarka, and T. Head-Gordon, *Aqueous peptides as experimental models for hydration water dynamics near protein surfaces*, *Physical Chemistry Chemical Physics* **10** (2008), no. 32 4903–4908.

[73] J. G. Davis, K. P. Gierszal, P. Wang, and D. Ben-Amotz, *Water structural transformation at molecular hydrophobic interfaces*, *Nature* **491** (Nov., 2012) 582–585.

[74] F. M. Agazzi, N. M. Correa, and J. Rodriguez, *Molecular Dynamics Simulation of Water/BHDC Cationic Reverse Micelles. Structural Characterization, Dynamical Properties, and Influence of Solvent on Intermicellar Interactions*, *Langmuir* **30** (Aug., 2014) 9643–9653.

[75] R. Costard, I. A. Heisler, and T. Elsaesser, *Structural Dynamics of Hydrated Phospholipid Surfaces Probed by Ultrafast 2d Spectroscopy of Phosphate Vibrations*, *The Journal of Physical Chemistry Letters* **5** (Feb., 2014) 506–511.

[76] G. Folpini, T. Siebert, M. Woerner, S. Abel, D. Laage, and T. Elsaesser, *Water Librations in the Hydration Shell of Phospholipids*, *The Journal of Physical Chemistry Letters* **8** (Sept., 2017) 4492–4497.

[77] C. Wang, C. Zhao, D. Li, Z. Tian, Y. Lai, J. Diao, and C. Liu, *Versatile Structures of -Synuclein*, *Frontiers in Molecular Neuroscience* **9** (June, 2016).

[78] L. J. Rothschild and R. L. Mancinelli, *Life in extreme environments*, *Nature* **409** (Feb., 2001) 35059215.

[79] R. P. Barnes, *Spatially heterogeneous surface water diffusivity around structured protein surfaces at equilibrium*, 2017.

[80] W. Doster, *The protein-solvent glass transition*, *Biochimica et Biophysica Acta (BBA) - Proteins and Proteomics* **1804** (Jan., 2010) 3–14.

[81] E. A. Golysheva, G. Y. Shevelev, and S. A. Dzuba, *Dynamical transition in molecular glasses and proteins observed by spin relaxation of nitroxide spin probes and labels*, *The Journal of Chemical Physics* **147** (Aug., 2017) 064501.

[82] N. P. Isaev and S. A. Dzuba, *Fast Stochastic Librations and Slow Rotations of Spin Labeled Stearic Acids in a Model Phospholipid Bilayer at Cryogenic Temperatures*, *The Journal of Physical Chemistry B* **112** (Oct., 2008) 13285–13291.

[83] K. Wood, A. Frlich, A. Paciaroni, M. Moulin, M. Hrtlein, G. Zaccai, D. J. Tobias, and M. Weik, *Coincidence of Dynamical Transitions in a Soluble Protein and Its Hydration Water: Direct Measurements by Neutron Scattering and MD Simulations*, *Journal of the American Chemical Society* **130** (Apr., 2008) 4586–4587.

[84] A. Volkov, C. Dockter, T. Bund, H. Paulsen, and G. Jeschke, *Pulsed EPR Determination of Water Accessibility to Spin-Labeled Amino Acid Residues in LHCIIb*, *Biophysical Journal* **96** (Feb., 2009) 1124–1141.

[85] A. Volkov, C. Dockter, Y. Polyhach, H. Paulsen, and G. Jeschke, *Site-Specific Information on Membrane Protein Folding by Electron Spin Echo Envelope Modulation Spectroscopy*, *The Journal of Physical Chemistry Letters* **1** (Feb., 2010) 663–667.

[86] G. Jeschke, *Principles of Pulse Electron Paramagnetic Resonance.* Oxford University Press, Oxford, New York, Aug., 2001.

[87] S. B. Kim, D. R. Gupta, and P. G. Debenedetti, *Computational investigation of dynamical transitions in Trp-cage miniprotein powders*, *Scientific Reports* **6** (May, 2016) 25612.

[88] B. D. Armstrong and S. Han, *A new model for Overhauser enhanced nuclear magnetic resonance using nitroxide radicals*, *The Journal of Chemical Physics* **127** (Sept., 2007) 104508.

[89] B. D. Armstrong and S. Han, *Overhauser Dynamic Nuclear Polarization To Study Local Water Dynamics*, *Journal of the American Chemical Society* **131** (Apr., 2009) 4641–4647.

[90] T. R. Carver and C. P. Slichter, *Experimental Verification of the Overhauser Nuclear Polarization Effect*, *Physical Review* **102** (May, 1956) 975–980.

[91] A. W. Overhauser, *Polarization of Nuclei in Metals*, *Physical Review* **92** (Oct., 1953) 411–415.

[92] J. B. Pedersen and J. H. Freed, *Some theoretical aspects of chemically induced dynamic nuclear polarization*, *The Journal of Chemical Physics* **61** (Aug., 1974) 1517–1525.

[93] J. B. Pedersen and J. H. Freed, *A hydrodynamic effect on chemically induced dynamic spin polarization*, *The Journal of Chemical Physics* **62** (Mar., 1975) 1790–1795.

[94] R. Gitti, C. Wild, C. Tsiao, K. Zimmer, T. E. Glass, and H. C. Dorn, *Solid/liquid intermolecular transfer of dynamic nuclear polarization. Enhanced flowing fluid proton NMR signals via immobilized spin labels*, *Journal of the American Chemical Society* **110** (Mar., 1988) 2294–2296.

[95] J. G. Krummenacker, V. P. Denysenkov, M. Terekhov, L. M. Schreiber, and T. F. Prisner, *DNP in MRI: An in-bore approach at 1.5t*, *Journal of Magnetic Resonance* **215** (Feb., 2012) 94–99.

[96] M. D. Lingwood, T. A. Siaw, N. Sailasuta, O. A. Abulseoud, H. R. Chan, B. D. Ross, P. Bhattacharya, and S. Han, *Hyperpolarized Water as an MR Imaging Contrast Agent: Feasibility of in Vivo Imaging in a Rat Model*, *Radiology* **265** (Nov., 2012) 418–425.

[97] E. R. McCarney, B. D. Armstrong, M. D. Lingwood, and S. Han, *Hyperpolarized water as an authentic magnetic resonance imaging contrast agent*, *Proceedings of the National Academy of Sciences* **104** (Feb., 2007) 1754–1759.

[98] O. Neudert, M. Reh, H. W. Spiess, and K. Mnnemann, *X-Band DNP Hyperpolarization of Viscous Liquids and Polymer Melts*, *Macromolecular Rapid Communications* **36** (May, 2015) 885–889.

[99] C.-Y. Cheng, O. J. Goor, and S. Han, *Quantitative Analysis of Molecular Transport across Liposomal Bilayer by J-Mediated 13c Overhauser Dynamic Nuclear Polarization*, *Analytical Chemistry* **84** (Nov., 2012) 8936–8940.

[100] C.-Y. Cheng, L. L. C. Olijve, R. Kausik, and S. Han, *Cholesterol enhances surface water diffusion of phospholipid bilayers*, *The Journal of Chemical Physics* **141** (Oct., 2014) 22D513.

[101] C.-Y. Cheng and S. Han, *Dynamic Nuclear Polarization Methods in Solids and Solutions to Explore Membrane Proteins and Membrane Systems*, *Annual Review of Physical Chemistry* **64** (Apr., 2013) 507–532.

[102] A. Doll, E. Bordignon, B. Joseph, R. Tschaggelar, and G. Jeschke, *Liquid state DNP for water accessibility measurements on spin-labeled membrane proteins at physiological temperatures*, *Journal of Magnetic Resonance* **222** (Sept., 2012) 34–43.

[103] J. M. Franck, J. A. Scott, and S. Han, *Nonlinear Scaling of Surface Water Diffusion with Bulk Water Viscosity of Crowded Solutions*, *Journal of the American Chemical Society* **135** (Mar., 2013) 4175–4178.

[104] R. Kausik and S. Han, *Ultrasensitive Detection of Interfacial Water Diffusion on Lipid Vesicle Surfaces at Molecular Length Scales*, *Journal of the American Chemical Society* **131** (Dec., 2009) 18254–18256.

[105] W. B. Mims, *Envelope Modulation in Spin-Echo Experiments*, *Physical Review B* **5** (Apr., 1972) 2409–2419.

[106] L. G. Rowan, E. L. Hahn, and W. B. Mims, *Electron-Spin-Echo Envelope Modulation*, *Physical Review* **137** (Jan., 1965) A61–A71.

[107] C. Altenbach, A. K. Kusnetzow, O. P. Ernst, K. P. Hofmann, and W. L. Hubbell, *High-resolution distance mapping in rhodopsin reveals the pattern of helix movement due to activation*, *Proceedings of the National Academy of Sciences* **105** (May, 2008) 7439–7444.

[108] S. Hussain, J. M. Franck, and S. Han, *Transmembrane Protein Activation Refined by Site-Specific Hydration Dynamics*, *Angewandte Chemie International Edition* **52** (Feb., 2013) 1953–1958.

[109] J.-M. Kim, C. Altenbach, M. Kono, D. D. Oprian, W. L. Hubbell, and H. G. Khorana, *Structural origins of constitutive activation in rhodopsin: Role of the K296/E113 salt bridge*, *Proceedings of the National Academy of Sciences of the United States of America* **101** (Aug., 2004) 12508–12513.

[110] A. Pavlova, E. R.McCarney, D. W.Peterson, F. W.Dahlquist, J. Lew, and S. Han, *Site-specific dynamic nuclear polarization of hydration water as a generally applicable approach to monitor protein aggregation*, *Physical Chemistry Chemical Physics* **11** (2009), no. 31 6833–6839.

[111] J. Song, T. H. Kang, M. W. Kim, and S. Han, *Ion specific effects: decoupling ionion and ionwater interactions*, *Physical Chemistry Chemical Physics* **17** (Mar., 2015) 8306–8322.

[112] J. Song, O. H. Han, and S. Han, *Nanometer-Scale Water- and Proton-Diffusion Heterogeneities across Water Channels in Polymer Electrolyte Membranes*, *Angewandte Chemie International Edition* **54** (Mar., 2015) 3615–3620.

[113] N. A. Eschmann, E. R. Georgieva, P. Ganguly, P. P. Borbat, M. D. Rappaport, Y. Akdogan, J. H. Freed, J.-E. Shea, and S. Han, *Signature of an aggregation-prone conformation of tau*, *Scientific Reports* **7** (Mar., 2017) srep44739.

[114] J. H. Ortony, D. S. Hwang, J. M. Franck, J. H. Waite, and S. Han, *Asymmetric Collapse in Biomimetic Complex Coacervates Revealed by Local Polymer and Water Dynamics*, *Biomacromolecules* **14** (May, 2013) 1395–1402.

[115] J. H. Ortony, S.-H. Choi, J. M. Spruell, J. N. Hunt, N. A. Lynd, D. V. Krogstad, V. S. Urban, C. J. Hawker, E. J. Kramer, and S. Han, *Fluidity and water in nanoscale domains define coacervate hydrogels*, *Chemical Science* **5** (Nov., 2013) 58–67.

[116] J. Song, B. Allison, and S. Han, *Local water diffusivity as a molecular probe of surface hydrophilicity*, *MRS Bulletin* **39** (Dec., 2014) 1082–1088.

[117] C. Griesinger, M. Bennati, H. M. Vieth, C. Luchinat, G. Parigi, P. Hfer, F. Engelke, S. J. Glaser, V. Denysenkov, and T. F. Prisner, *Dynamic nuclear polarization at high magnetic fields in liquids*, *Progress in Nuclear Magnetic Resonance Spectroscopy* **64** (July, 2012) 4–28.

[118] I. Solomon, *Relaxation Processes in a System of Two Spins*, *Physical Review* **99** (July, 1955) 559–565.

[119] D. Sezer, M. Gafurov, M. J. Prandolini, V. P. Denysenkov, and T. F. Prisner, *Dynamic nuclear polarization of water by a nitroxide radical: rigorous treatment of the electron spin saturation and comparison with experiments at 9.2 Tesla*, *Physical Chemistry Chemical Physics* **11** (July, 2009) 6638–6653.

[120] M. Bennati, C. Luchinat, G. Parigi, and M.-T. Trke, *Water 1h relaxation dispersion analysis on a nitroxide radical provides information on the maximal

signal enhancement in Overhauser dynamic nuclear polarization experiments, *Physical Chemistry Chemical Physics* **12** (May, 2010) 5902–5910.

[121] N. Enkin, G. Liu, M. d. C. Gimenez-Lopez, K. Porfyrakis, I. Tkach, and M. Bennati, *A high saturation factor in Overhauser DNP with nitroxide derivatives: the role of 14n nuclear spin relaxation*, *Physical Chemistry Chemical Physics* **17** (Apr., 2015) 11144–11149.

[122] N. Enkin, G. Liu, I. Tkach, and M. Bennati, *High DNP efficiency of TEMPONE radicals in liquid toluene at low concentrations*, *Physical Chemistry Chemical Physics* **16** (Apr., 2014) 8795–8800.

[123] P. Lottmann, T. Marquardsen, A. Krahn, A. Tavernier, P. Hfer, M. Bennati, F. Engelke, and C. Griesinger, *Evaluation of a Shuttle DNP Spectrometer by Calculating the Coupling and Global Enhancement Factors of l-Tryptophan*, *Applied Magnetic Resonance* **43** (July, 2012) 207–221.

[124] M.-T. Trke, I. Tkach, M. Reese, P. Hfer, and M. Bennati, *Optimization of dynamic nuclear polarization experiments in aqueous solution at 15 MHz/9.7 GHz: a comparative study with DNP at 140 MHz/94 GHz*, *Physical Chemistry Chemical Physics* **12** (May, 2010) 5893–5901.

[125] D. Sezer, *Computation of DNP coupling factors of a nitroxide radical in toluene: seamless combination of MD simulations and analytical calculations*, *Physical Chemistry Chemical Physics* **15** (Dec., 2012) 526–540.

[126] B. H. Robinson, D. A. Haas, and C. Mailer, *Molecular dynamics in liquids: spin-lattice relaxation of nitroxide spin labels*, *Science (New York, N.Y.)* **263** (Jan., 1994) 490–493.

[127] M.-T. Trke and M. Bennati, *Saturation factor of nitroxide radicals in liquid DNP by pulsed ELDOR experiments*, *Physical Chemistry Chemical Physics* **13** (Feb., 2011) 3630–3633.

[128] J. S. Hyde, W. Froncisz, and C. Mottley, *Pulsed eldor measurement of nitrogen T1 in spin labels*, *Chemical Physics Letters* **110** (Oct., 1984) 621–625.

[129] J. H. Freed, *Dynamic effects of pair correlation functions on spin relaxation by translational diffusion in liquids. II. Finite jumps and independent T1 processes*, *The Journal of Chemical Physics* **68** (May, 1978) 4034–4037.

[130] Y. Ayant, E. Belorizky, J. Aluzon, and J. Gallice, *Calcul des densits spectrales rsultant d'un mouvement alatoire de translation en relaxation par interaction dipolaire magntique dans les liquides*, *Journal de Physique* **36** (Oct., 1975) 991–1004.

[131] Y. Ayant, E. Belorizky, P. Fries, and J. Rosset, *Effet des interactions dipolaires magntiques intermolculaires sur la relaxation nuclaire de molcules polyatomiques dans les liquides*, *Journal de Physique* **38** (Mar., 1977) 325–337.

[132] D. Sezer, *Rationalizing Overhauser DNP of nitroxide radicals in water through MD simulations*, *Physical Chemistry Chemical Physics* **16** (Dec., 2013) 1022–1032.

[133] J. C. Hindman, A. Svirmickas, and M. Wood, *Relaxation processes in water. A study of the proton spinlattice relaxation time*, *The Journal of Chemical Physics* **59** (Aug., 1973) 1517–1522.

[134] D. Reichert and G. Hempel, *Receiver imperfections and CYCLOPS: An alternative description*, *Concepts in Magnetic Resonance* **14** (2002), no. 2 130–139.

[135] R. G. Bryant, *Dynamics of water in and around proteins characterized by 1h-spin-lattice relaxometry*, *Comptes Rendus Physique* **11** (Mar., 2010) 128–135.

[136] P. G. Fajer, *Electron Spin Resonance Spectroscopy Labeling in Peptide and Protein Analysis*, in *Encyclopedia of Analytical Chemistry*. John Wiley & Sons, Ltd, 2006. DOI: 10.1002/9780470027318.a1609.

[137] "Wiley: Electron Paramagnetic Resonance: Elementary Theory and Practical Applications, 2nd Edition - John A. Weil, James R. Bolton."

[138] J. S. Hodges, J. C. Yang, C. Ramanathan, and D. G. Cory, *Universal control of nuclear spins via anisotropic hyperfine interactions*, *Physical Review A* **78** (July, 2008) 010303.

[139] J. P. Hornak and J. H. Freed, *Spectral rotation in pulsed ESR spectroscopy*, *Journal of Magnetic Resonance (1969)* **67** (May, 1986) 501–518.

[140] Y. Zhang, C. A. Ryan, R. Laflamme, and J. Baugh, *Coherent Control of Two Nuclear Spins Using the Anisotropic Hyperfine Interaction*, *Physical Review Letters* **107** (Oct., 2011) 170503.

[141] T. E. Skinner, K. Kobzar, B. Luy, M. R. Bendall, W. Bermel, N. Khaneja, and S. J. Glaser, *Optimal control design of constant amplitude phase-modulated pulses: Application to calibration-free broadband excitation*, *Journal of Magnetic Resonance* **179** (Apr., 2006) 241–249.

[142] J. Pauly, P. Le Roux, D. Nishimura, and A. Macovski, *Parameter relations for the Shinnar-Le Roux selective excitation pulse design algorithm [NMR imaging]*, *IEEE transactions on medical imaging* **10** (1991), no. 1 53–65.

[143] N. Khaneja, T. Reiss, C. Kehlet, T. Schulte-Herbrggen, and S. J. Glaser, *Optimal control of coupled spin dynamics: design of NMR pulse sequences by gradient ascent algorithms*, *Journal of Magnetic Resonance* **172** (Feb., 2005) 296–305.

[144] A. Doll, S. Pribitzer, R. Tschaggelar, and G. Jeschke, *Adiabatic and fast passage ultra-wideband inversion in pulsed EPR*, *Journal of Magnetic Resonance* **230** (May, 2013) 27–39.

[145] P. E. Spindler, Y. Zhang, B. Endeward, N. Gershernzon, T. E. Skinner, S. J. Glaser, and T. F. Prisner, *Shaped optimal control pulses for increased excitation bandwidth in EPR*, *Journal of Magnetic Resonance* **218** (May, 2012) 49–58.

[146] P. E. Spindler, S. J. Glaser, T. E. Skinner, and T. F. Prisner, *Broadband Inversion PELDOR Spectroscopy with Partially Adiabatic Shaped Pulses*, *Angewandte Chemie International Edition* **52** (Mar., 2013) 3425–3429.

[147] G. Jeschke, *Distance Measurements in the Nanometer Range by Pulse EPR*, *ChemPhysChem* **3** (Nov., 2002) 927–932.

[148] J. S. Hyde, J. C. W. Chien, and J. H. Freed, *ElectronElectron Double Resonance of Free Radicals in Solution*, *The Journal of Chemical Physics* **48** (May, 1968) 4211–4226.

[149] Y.-W. Chiang, A. J. Costa-Filho, and J. H. Freed, *Dynamic Molecular Structure and Phase Diagram of DPPCCholesterol Binary Mixtures: A 2d-ELDOR Study*, *The Journal of Physical Chemistry B* **111** (Sept., 2007) 11260–11270.

[150] Y.-W. Chiang, A. J. Costa-Filho, B. Baird, and J. H. Freed, *2d-ELDOR Study of Heterogeneity and Domain Structure Changes in Plasma Membrane Vesicles upon Cross-Linking of Receptors*, *The Journal of Physical Chemistry B* **115** (Sept., 2011) 10462–10469.

[151] P. Hfer, A. Grupp, H. Nebenfhr, and M. Mehring, *Hyperfine sublevel correlation (hyscore) spectroscopy: a 2d ESR investigation of the squaric acid radical*, *Chemical Physics Letters* **132** (Dec., 1986) 279–282.

[152] R. SZOSENFOGEL and D. GOLDFARB, *Simulations of HYSCORE spectra obtained with ideal and non-ideal pulses*, *Molecular Physics* **95** (Dec., 1998) 1295–1308.

[153] P. P. Borbat and J. H. Freed, *Multiple-quantum ESR and distance measurements*, *Chemical Physics Letters* **313** (Nov., 1999) 145–154.

[154] G. A. Rinard, R. W. Quine, R. Song, G. R. Eaton, and S. S. Eaton, *Absolute EPR Spin Echo and Noise Intensities*, *Journal of Magnetic Resonance* **140** (Sept., 1999) 69–83.

[155] S. K. Misra and J. H. Freed, *Distance Measurements: Continuous-Wave (CW)- and Pulsed Dipolar EPR*, in *Multifrequency Electron Paramagnetic Resonance* (S. K. Misra, ed.), pp. 545–588. Wiley-VCH Verlag GmbH & Co. KGaA, 2011. DOI: 10.1002/9783527633531.ch12.

[156] C. J. Bardeen, V. V. Yakovlev, K. R. Wilson, S. D. Carpenter, P. M. Weber, and W. S. Warren, *Feedback quantum control of molecular electronic population transfer*, *Chemical Physics Letters* **280** (Nov., 1997) 151–158.

[157] R. H. Crepeau, A. Dul, J. Gorcester, T. R. Saarinen, and J. H. Freed, *Composite pulses in time-domain ESR*, *Journal of Magnetic Resonance (1969)* **84** (Aug., 1989) 184–190.

[158] R. H. Pursley, J. Kakareka, G. Salem, N. Devasahayam, S. Subramanian, R. G. Tschudin, M. C. Krishna, and T. J. Pohida, *Stochastic excitation and Hadamard correlation spectroscopy with bandwidth extension in RF FT-EPR*, *Journal of Magnetic Resonance* **162** (May, 2003) 35–45.

[159] N. Devasahayam, R. Murugesan, K. Matsumoto, J. B. Mitchell, J. A. Cook, S. Subramanian, and M. C. Krishna, *Tailored sinc pulses for uniform excitation and artifact-free radio frequency time-domain EPR imaging*, *Journal of Magnetic Resonance* **168** (May, 2004) 110–117.

[160] M. S. Silver, R. I. Joseph, and D. I. Hoult, *Selective spin inversion in nuclear magnetic resonance and coherent optics through an exact solution of the Bloch-Riccati equation*, *Physical Review A* **31** (Apr., 1985) 2753–2755.

[161] M. Garwood and L. DelaBarre, *The Return of the Frequency Sweep: Designing Adiabatic Pulses for Contemporary NMR*, *Journal of Magnetic Resonance* **153** (Dec., 2001) 155–177.

[162] B. Blmich, Q. Gong, E. Byrne, and M. Greferath, *NMR with excitation modulated by Frank sequences*, *Journal of Magnetic Resonance* **199** (July, 2009) 18–24.

[163] T. W. Borneman and D. G. Cory, *Bandwidth-limited control and ringdown suppression in high-Q resonators*, *Journal of Magnetic Resonance* **225** (Dec., 2012) 120–129.

[164] R. C. Bialczak, M. Ansmann, M. Hofheinz, E. Lucero, M. Neeley, A. D. OConnell, D. Sank, H. Wang, J. Wenner, M. Steffen, A. N. Cleland, and J. M. Martinis, *Quantum process tomography of a universal entangling gate implemented with Josephson phase qubits*, *Nature Physics* **6** (Apr., 2010) nphys1639.

[165] T. Maly, F. MacMillan, K. Zwicker, N. Kashani-Poor, U. Brandt, and T. F. Prisner, *Relaxation filtered hyperfine (REFINE) spectroscopy: a novel tool for studying overlapping biological electron paramagnetic resonance signals applied to mitochondrial complex I*, *Biochemistry* **43** (Apr., 2004) 3969–3978.

[166] G. R. Eaton, S. S. Eaton, R. W. Quine, D. Mitchell, V. Kathirvelu, and R. T. Weber, *A signal-to-noise standard for pulsed EPR*, *Journal of Magnetic Resonance* **205** (July, 2010) 109–113.

[167] S. Saxena and J. H. Freed, *Theory of double quantum two-dimensional electron spin resonance with application to distance measurements*, *The Journal of Chemical Physics* **107** (Aug., 1997) 1317–1340.

[168] E. O. Stejskal and J. Schaefer, *Comparisons of quadrature and single-phase fourier transform NMR*, *Journal of Magnetic Resonance (1969)* **14** (May, 1974) 160–169.

[169] G. Jeschke and A. Schweiger, *Matched twopulse electron spin echo envelope modulation spectroscopy*, *The Journal of Chemical Physics* **105** (Aug., 1996) 2199–2211.

[170] M. Tseitlin, R. W. Quine, G. A. Rinard, S. S. Eaton, and G. R. Eaton, *Digital EPR with an arbitrary waveform generator and direct detection at the carrier frequency*, *Journal of Magnetic Resonance* **213** (Dec., 2011) 119–125.

[171] K. Kobzar, B. Luy, N. Khaneja, and S. J. Glaser, *Pattern pulses: design of arbitrary excitation profiles as a function of pulse amplitude and offset*, *Journal of Magnetic Resonance* **173** (Apr., 2005) 229–235.

[172] P. P. Borbat, E. R. Georgieva, and J. H. Freed, *Improved Sensitivity for Long-Distance Measurements in Biomolecules: Five-Pulse Double ElectronElectron Resonance*, *The Journal of Physical Chemistry Letters* **4** (Jan., 2013) 170–175.

[173] M. Gordon-Grossman, I. Kaminker, Y. Gofman, Y. Shai, and D. Goldfarb, *W-Band pulse EPR distance measurements in peptides using Gd3+dipicolinic acid derivatives as spin labels*, *Physical Chemistry Chemical Physics* **13** (May, 2011) 10771–10780.

[174] R. Rizzato and M. Bennati, *Enhanced sensitivity of electron-nuclear double resonance (ENDOR) by cross polarisation and relaxation*, *Physical Chemistry Chemical Physics* **16** (Apr., 2014) 7681–7685.

[175] W. Froncisz, T. G. Camenisch, J. J. Ratke, J. R. Anderson, W. K. Subczynski, R. A. Strangeway, J. W. Sidabras, and J. S. Hyde, *Saturation recovery EPR and ELDOR at W-band for spin labels*, *Journal of Magnetic Resonance* **193** (Aug., 2008) 297–304.

[176] D. E. Budil, S. Lee, S. Saxena, and J. H. Freed, *Nonlinear-Least-Squares Analysis of Slow-Motion EPR Spectra in One and Two Dimensions Using a Modified LevenbergMarquardt Algorithm*, *Journal of Magnetic Resonance, Series A* **120** (June, 1996) 155–189.

[177] S. Stoll and A. Schweiger, *EasySpin, a comprehensive software package for spectral simulation and analysis in EPR*, *Journal of Magnetic Resonance* **178** (Jan., 2006) 42–55.

[178] L. J. Schwartz, A. E. Stillman, and J. H. Freed, *Analysis of electron spin echoes by spectral representation of the stochastic Liouville equation*, *The Journal of Chemical Physics* **77** (Dec., 1982) 5410–5425.

[179] M. Bonora, S. Pornsuwan, and S. Saxena, *Nitroxide SpinRelaxation over the Entire Motional Range*, *The Journal of Physical Chemistry B* **108** (Apr., 2004) 4196–4198.

[180] D. I. Hoult, *Fast recovery, high sensitivity NMR probe and preamplifier for low frequencies*, *Review of Scientific Instruments* **50** (Feb., 1979) 193–200.

[181] N. S. Sullivan, P. Deschamps, P. Nel, and J. M. Vaissire, *Efficient fast-recovery scheme for NMR pulse spectrometers*, *Revue de Physique Applique* **18** (Apr., 1983) 253–261.

[182] I. J. Lowe and D. E. Barnaal, *RadioFrequency Bridge for Pulsed Nuclear Magnetic Resonance*, *Review of Scientific Instruments* **34** (Feb., 1963) 143–146.

[183] M. Alecci, J. A. Brivati, G. Placidi, L. Testa, D. J. Lurie, and A. Sotgiu, *A Submicrosecond Resonator and Receiver System for Pulsed Magnetic Resonance with Large Samples*, *Journal of Magnetic Resonance* **132** (May, 1998) 162–166.

[184] G. A. Rinard, R. W. Quine, B. T. Ghim, S. S. Eaton, and G. R. Eaton, *Easily Tunable Crossed-Loop (Bimodal) EPR Resonator*, *Journal of Magnetic Resonance, Series A* **122** (Sept., 1996) 50–57.

[185] A. I. Tsapin, J. S. Hyde, and W. Froncisz, *Bimodal loop-gap resonator*, *Journal of Magnetic Resonance (1969)* **100** (Dec., 1992) 484–490.

[186] G. A. Rinard, R. W. Quine, and G. R. Eaton, *An L-Band Crossed-Loop (Bimodal) EPR Resonator*, *Journal of Magnetic Resonance* **144** (May, 2000) 85–88.

[187] P. A. S. Cruickshank, D. R. Bolton, D. A. Robertson, R. I. Hunter, R. J. Wylde, and G. M. Smith, *A kilowatt pulsed 94 GHz electron paramagnetic resonance spectrometer with high concentration sensitivity, high instantaneous bandwidth, and low dead time*, *Review of Scientific Instruments* **80** (Oct., 2009) 103102.

[188] T. N. Rudakov, V. V. Fedotov, A. V. Belyakov, and V. T. Mikhaltsevich, *Suppression of transient processes in the oscillatory circuit of the NQR spectrometer*, *Instruments and Experimental Techniques* **43** (Jan., 2000) 78–81.

[189] P. P. Borbat, R. H. Crepeau, and J. H. Freed, *Multifrequency Two-Dimensional Fourier Transform ESR: An X/KuBand Spectrometer*, *Journal of Magnetic Resonance* **127** (Aug., 1997) 155–167.

[190] G. A. Rinard, R. W. Quine, S. S. Eaton, G. R. Eaton, and W. Froncisz, *Relative Benefits of Overcoupled Resonators vs Inherently Low-Q Resonators for Pulsed Magnetic Resonance*, *Journal of Magnetic Resonance, Series A* **108** (May, 1994) 71–81.

[191] J. L. Davis and W. B. Mims, *Use of a microwave delay line to reduce the dead time in electron spin echo envelope spectroscopy*, *Review of Scientific Instruments* **52** (Jan., 1981) 131–132.

[192] P. A. Narayana, R. J. Massoth, and L. Kevan, *Active microwave delay line for reducing the dead time in electronspin echo spectrometry*, *Review of Scientific Instruments* **53** (May, 1982) 624–626.

[193] T. Kaufmann, T. J. Keller, J. M. Franck, R. P. Barnes, S. J. Glaser, J. M. Martinis, and S. Han, *DAC-board based X-band EPR spectrometer with arbitrary waveform control*, *Journal of Magnetic Resonance* **235** (Oct., 2013) 95–108.

[194] A. Doll and G. Jeschke, *Fourier-transform electron spin resonance with bandwidth-compensated chirp pulses*, *Journal of Magnetic Resonance* **246** (Sept., 2014) 18–26.

[195] L. Sun, J. J. Savory, and K. Warncke, *Design and implementation of an FPGA-based timing pulse programmer for pulsed-electron paramagnetic resonance applications*, *Concepts in Magnetic Resonance Part B: Magnetic Resonance Engineering* **43** (Aug., 2013) 100–109.

[196] Y. Twig, E. Dikarov, W. D. Hutchison, and A. Blank, *Note: High sensitivity pulsed electron spin resonance spectroscopy with induction detection*, *Review of Scientific Instruments* **82** (July, 2011) 076105.

[197] A. Blank, E. Stavitski, H. Levanon, and F. Gubaydullin, *Transparent miniature dielectric resonator for electron paramagnetic resonance experiments*, *Review of Scientific Instruments* **74** (Apr., 2003) 2853–2859.

[198] R. Narkowicz, D. Suter, and R. Stonies, *Planar microresonators for EPR experiments*, *Journal of Magnetic Resonance* **175** (Aug., 2005) 275–284.

[199] R. Narkowicz, D. Suter, and I. Niemeyer, *Scaling of sensitivity and efficiency in planar microresonators for electron spin resonance*, *Review of Scientific Instruments* **79** (Aug., 2008) 084702.

[200] T. A. Siaw, A. Leavesley, A. Lund, I. Kaminker, and S. Han, *A versatile and modular quasi optics-based 200ghz dual dynamic nuclear polarization and electron paramagnetic resonance instrument*, *Journal of Magnetic Resonance* **264** (Mar., 2016) 131–153.

[201] J. Kyte and R. F. Doolittle, *A simple method for displaying the hydropathic character of a protein*, *Journal of Molecular Biology* **157** (May, 1982) 105–132.

[202] J. M. Martinis, *Superconducting phase qubits*, *Quantum Information Processing* **8** (June, 2009) 81–103.